Politecnico di Bari

Department of Mechanics, Mathematics and Management
MECHANICAL AND MANAGEMENT ENGINEERING
Ph.D. Program
SSD: ING-IND/08–FLUID MACHINERY

Final Dissertation

Theoretical and Experimental Analysis of Pumps as Turbines

---

by
Michele Stefanizzi

Supervisors:

Prof. Sergio Mario Camporeale

Prof. Marco Torresi

Ing. Rosario Monteriso

Coordinator of Ph.D. Program:
Prof. Giuseppe Pompeo Demelio

Course n°31, 01/11/2015-31/10/2018

Politecnico di Bari

Department of Mechanics, Mathematics and Management
MECHANICAL AND MANAGEMENT ENGINEERING
Ph.D. Program
SSD: ING-IND/08–FLUID MACHINERY

Final Dissertation

Theoretical and Experimental Analysis of Pumps as Turbines

---

by
Michele Stefanizzi

Referees:

Prof. Mario Amelio

Prof. Massimiliano Renzi

Supervisors:

Prof. Sergio Mario Camporeale

Prof. Marco Torresi

Ing. Rosario Monteriso

Coordinator of Ph.D Program:
Prof. Giuseppe Pompeo Demelio

Course n°31, 01/11/2015-31/10/2018

POLYTECHNIC OF BARI UNIVERSITY

Abstract

Engineering Faculty
Department of Mechanics, Mathematics and Management

Doctor of Philosophy

Theoretical and Experimental Analysis of Pumps as Turbines

by Michele STEFANIZZI

This PhD thesis is focused on theoretical and experimental analysis of Pumps as Turbines (PaTs). The PhD research project has been carried out in partnership with Nuovo Pignone Bari, a leader company in pump manufacturing, which founded this PhD scholarship.

A PaT is a conventional pump used in reverse mode in order to recover energy, wasted otherwise, from flows subjected to considerable pressure drops. Due to the complexity of developing customized turbines, using pumps in reverse mode may represent a practical solution, in consideration of the wide range of specific speed numbers and available standard sizes of pumps. However, this technology is considered a cost-effective alternative to traditional turbines as long as their turbine mode performance can be predicted.

Unfortunately, pump manufacturers do not usually offer performance curves of their pumps in reverse mode, since this requires testing of the machines also in turbine mode operation, hence increasing significantly their costs. Because of this lack of experimental data, a big number of studies can be found about the prediction of PaT performance but mainly focused on the turbine BEP (Best Efficiency Point). These prediction models are extremely simple but seldom consider off-design points. Furthermore, these models show a low applicability, showing prediction errors within $\pm 20\%$, being usually based on experimental correlations from a limited number of samples. On the other side, pump manufacturers need a tool that could support them to predict the turbine mode performance of their pumps.

In this landscape, the present work aims at developing two different prediction models: (i) an experimental model for the prediction of the BEP of PaTs, as a selection tool for users, which has showed a better accuracy (BEP prediction errors within $\pm 10\%$) than the models found in literature; (ii) and a new 1-D model for the prediction of the entire characteristic, as a design tool for manufactures. The model has been validated on three machines by Nuovo Pignone, showing a better accuracy in the prediction of their characteristics within $\pm 4\%$ than other models in literature and the pre-existing model developed by Nuovo Pignone.

Moreover, a closed-loop test rig for experimental studies on hydraulic pumps and turbines has been set up. A KSB single-stage centrifugal pump has been tested in both direct and reverse modes. Experimental characteristic curves have been used to develop the experimental model for turbine BEP prediction, and to carry out a preliminary assessment of the installation of the same PaT in a real water distribution network in order to supply an electrical charging station.

Finally, a theoretical approach has been proposed in order to predict the PaT performance with a two-phase flow, whose expansion characteristics are known.

Acknowledgements

I would like to express my gratitude to my supervisors Marco Torresi, Sergio Mario Camporeale and Rosario Monteriso for the help and the support during the development of this research project.

I sincerely thank Marco Torresi for the willingness and the patience with which he has followed this research work.

I thank Sergio Mario Camporeale who has professionally supervised the entire research project. I thank Rosario Monteriso as well for all the support given to me by the Nuovo Pignone company branch.

I gratefully acknowledge Nuovo Pignone, which have funded this PhD research project. Special thanks to my colleague, Tommaso Capurso, with whom I shared this valuable experience.

Thanks to the technician of the test rig, Vito Mele, for his help during the set-up of the test rig.

I would like also to thank Helmut Jaberg and his staff, who gave me the opportunity to study in the Institute of Hydraulic Fluid Machinery, at the Graz University of Technology (Austria).

Finally, thanks to my family, solid support in all my life choices.

Contents

List of Figures

List of Tables

List of Abbreviations

AC	-	**A**lternate **C**urrent
BEP	-	**B**est **E**fficiency **P**oint
CFD	-	**C**omputer **F**luid **D**ynamics
DAQ	-	**D**ata **A**c**Q**uisition
DC	-	**D**irect **C**urrent
DMA	-	**D**istrict **M**etering **A**rea
DMMM	-	**D**epartment of **M**echanics **M**athematics and **M**anagement
DOF	-	**D**egree **O**f **F**reedom
FPGA	-	**F**ield **P**rogrammable **G**ate **A**rray
PaT	-	**P**ump **a**s **T**urbine
PRV	-	**P**ressure **R**educing **V**alve
SHP	-	**S**mall **H**ydro **P**ower
TDMS	-	**T**echnical **D**ata **M**anagement **S**treaming
UNIDO	-	**U**nited **N**ations **I**ndustrial **D**evelopment **O**rganization
VI	-	**V**irtual **I**nstrument
WDN	-	**W**ater **D**istribution **N**etwork

List of Symbols

A	Cross section area	$[m^2]$
a_3	Throat volute height	$[m]$
b	Width of runner channel	$[m]$
C	Torque	$[Nm]$
c	Absolute velocity	$[m/s]$
c_f	Friction coefficient of a flat plate	$[-]$
c_m	Meridional component of the absolute velocity	$[m/s]$
c_P	Hydraulic Source Harvesting Coefficient	$[-]$
c_u	Tangential component of the absolute velocity	$[m/s]$
D	Diameter	$[m]$
D_h	Hydraulic diameter	$[m]$
D_{hub}	Hub diameter	$[m]$
D_m	Mean diameter	$[m]$
D_{tip}	Tip diameter	$[m]$
e_3	Volute tongue thickness	$[m]$
e_H	Relative error in turbine head prediction	[%]
e_Q	Relative error in turbine flow rate prediction	[%]
f	Colebrook's friction loss coefficient	$[-]$
H^0	Total head	$[m]$
$\overline{H}$	Average head	$[m]$
$H_{BEP,P}$	PaT head at BEP under pump mode operation	$[m]$
$H_{BEP,T}$	PaT head at BEP under turbine mode operation	$[m]$
H_G	Guaranteed head	$[m]$
H_{site}	Head of the installation site	$[m]$
H_{th}	Theoretical head	$[m]$
L	Length	$[m]$
N	Rotational speed	$[rpm]$
N_s	Specific speed number	$[m^3/s, m, rpm]$
$N_{s,P}$	Specific speed number of the PaT under pump mode operation	$[m^3/s, m, rpm]$
$N_{s,T}$	Specific speed number of the PaT under turbine mode operation	$[m^3/s, m, rpm]$
N_{stages}	Number of stages	$[-]$
P	Power	$[W]$
P_{hydr}	Hydraulic power	$[W]$
$P_{hydr,available}$	Available hydraulic power from the installation site	$[W]$
$P_{hydr,obt.}$	PaT obtained power	$[W]$
p	Pressure	$[Pa]$
p_{in}	Inlet pressure of the machine	$[Pa]$
p_{out}	Outlet pressure of the machine	$[Pa]$
Q	Flow rate	$[m^3/s]$
$\overline{Q}$	Average flow rate	$[m^3/s]$
$Q_{BEP,P}$	PaT flow rate at BEP under pump mode operation	$[m^3/s]$
$Q_{BEP,T}$	PaT flow rate at BEP under turbine mode operation	$[m^3/s]$

Q_G	Guaranteed flow rate	$[m^3/s]$
Q_{site}	Flow rate of the installation site	$[m^3/s]$
r	Radius	$[m]$
Re	Reynolds Number	$[m]$
t	t-student distribution corrective factor	$[-]$
t_3	Volute pitch	$[m]$
u	Tangential velocity	$[m/s]$
U_y	Expanded uncertainty	[%]
$U_c\ (y)$	Combined standard uncertainty	[%]
u_R	Random type uncertainty	[%]
u_S	Systematic type uncertainty	[%]
u_y	Overall uncertainty	[%]
w	Relative velocity	$[m/s]$
W_{th}	Theoretical work	$[J]$
x	Mass vapour fraction	[%]
Y	Specific work	$[J/kg]$
Z_{blades}	Number of impeller blades	$[-]$
Z_f	Friction loss	$[m]$
Z_h	Hydraulic loss	$[m]$
Z_L	Local loss	$[m]$

Greek Symbols

α	absolute flow angle	$[^\circ]$
α	volume vapour fraction	[%]
β	Relative flow angle	$[^\circ]$
β_B	Relative impeller blade angle	$[^\circ]$
ϵ	Roughness	$[m]$
ζ	Local loss coefficient	$[-]$
η	Efficiency	$[-]$
$\eta_{BEP,P}$	Best Efficiency of the PaT under pump mode operation	$[-]$
$\eta_{BEP,T}$	Best Efficiency of the PaT under turbine mode operation	$[-]$
η_v	Volumetric Efficiency	$[-]$
λ	Power Coefficient	$[-]$
ν	Kinematic Viscosity	$[m^2/s]$
ξ	Blade blockage factor	$[-]$
ρ	Density	$[kg/m^3]$
ρ_L	Liquid density	$[kg/m^3]$
ρ_V	Vapour density	$[kg/m^3]$
σ	Slip factor	$[-]$
φ	Flow coefficient	$[-]$
ψ	Pressure coefficient	$[-]$

Dedicated to my Family

Chapter 1

Introduction

1.1 Motivations

A Pump as Turbine (PaT) is a conventional pump used in reverse mode, as represented in Fig. 1.1. It is used to recover energy, wasted otherwise, from fluids subjected to a considerable pressure drop, as an alternative to throttling devices. This technology is becoming more and more tempting in a scenario where the increasing energy demand represents a priority issue to be faced with social, economic, political and technical points of view. In both developing and developed countries, the need for clean and sustainable energy sources is growing more and more stringently to contrast the anthropic climate changes. For this reason, renewable energy sources should be preferred to the conventional ones in order to follow the track of a sustainable development. In many industrial plants, PaTs could be an important renewable energy technology, contributing to create smart grids, rural electrification, sustainable industrial development as well as the reduction of greenhouse gas emissions and deforestation.

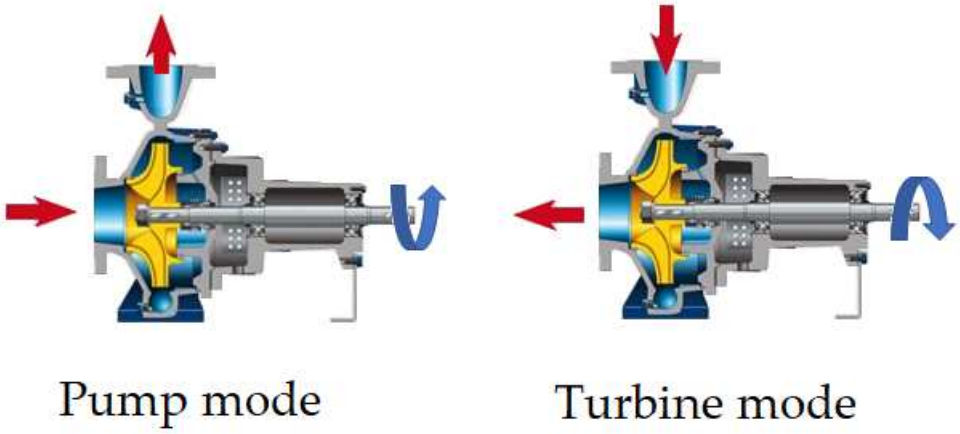

FIGURE 1.1: Single stage centrifugal pump operating in direct mode (left) and reverse mode (right) [1].

Among renewable energy sources, Small Hydropower Plants (SHPs) represent a promising solution in electricity production, having no significant environmental impact. According to the latest World Small Hydropower Development Report by the United Nations Industrial Development Organization (UNIDO) [2], approximately 36 % of the current global SHP potential has been developed in 2016. SHPs

represent 7 % of the total renewable energy capacity and 6.5 % of the total hydropower capacity (including pumped storage). Europe has the highest SHP development rate, with nearly 48 % of the overall potential already installed (Fig. 1.2 and Fig. 1.3).

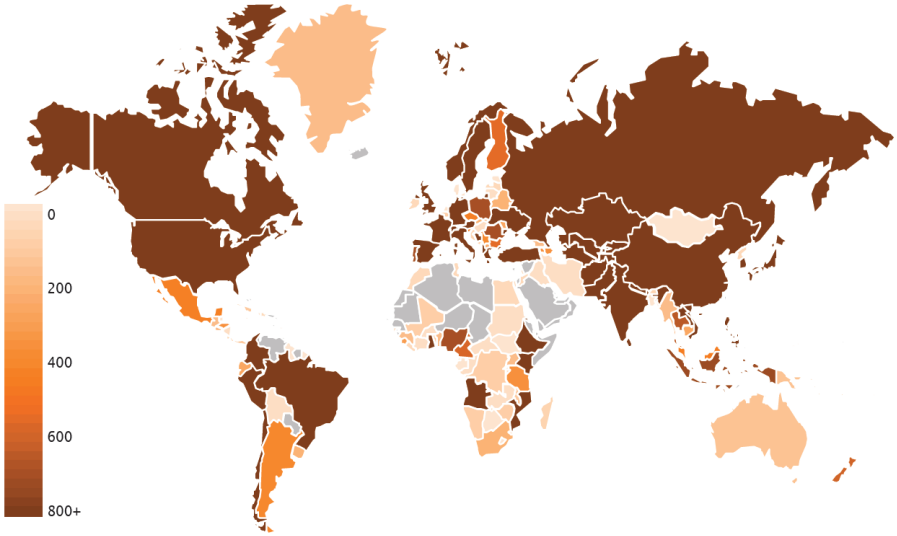

FIGURE 1.2: Identified SHP potential by country [MW] [2].

In the hydraulic area, there are power plants of the order of megawatts, which are located in some well-defined places on the planet thanks to the availability of suitable pressure drops and adequate flow rates. In addition to this field, the interest in water distribution networks (WDNs) is beginning to be strong. Indeed, it is often necessary to insert pressure dissipation points inside the WDNs in order to reduce leakages, sometimes very high especially during the night, since the water drinking demand is insignificant and consequently the pressure in the network reaches maximum levels. To this end, the water management authorities are partitioning water distribution networks into District Metering Areas (DMAs) and installing an ever-increasing number of pressure reduction valves (PRVs) in well-specific points useful to control daily pressure pattern.

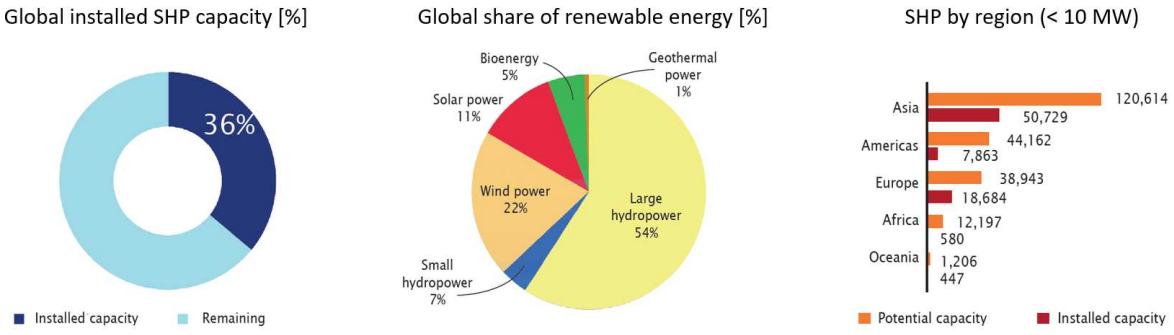

FIGURE 1.3: Global overviews on SHP potential [2].

In this framework, PaTs represent a technical solution to save and produce energy by replacing PRVs. Due to the complexity of developing customized turbines, the use of pumps operating in reverse mode may represent a practical solution, in

consideration of the wide range of specific speed numbers and available standard sizes of pumps.

Moreover, PaTs can be used not only in hydraulic power generation but also in processes engineering, where fluids containing dissolved or undissolved gases or volatiles can be expanded from a higher to a lower pressure level for energy recovery. As the gas contained in the fluid is released from the solution during expansion, the flow rate increases, and additional energy is delivered with respect to the case of incompressible flow. Usually, manufacturing companies test their machines in single phase (generally water). For this reason, they need a global performance correction tool, that could evaluate the power output surplus under two-phase conditions.

However, PaTs are considered a cost-effective alternative to traditional turbines as long as their turbine mode performance can be predicted. Unfortunately, pump manufacturers do not usually offer performance curves of their pumps in reverse mode, since this requires testing of the machines also in turbine mode operation, hence increasing significantly their costs. Because of this lack of experimental data, a consistent effort was made by several authors in the prediction of PaT performance not only with theoretical approaches, but also with experimental campaigns of pumps tested in reverse mode. The common target was to develop models, able to predict PaT performance by knowing the pump main characteristics. At the beginning, these models were mainly focused on the turbine BEP (Best Efficiency Point). Most of them have been developed for users who can only retrieve information from the pump datasheet (flow rate, head and efficiency at the BEP). For this reason, these prediction models are extremely simple but seldom consider off-design points. Furthermore, these models show a low applicability, being usually based on experimental correlations from a limited number of samples.

On the other side, pump manufacturers need a tool that could support them to predict the turbine mode performance by knowing pump characteristics, in order to be competitive on the market. Indeed, manufacturers have detailed geometric information of their machines that could be useful in the development of more accurate models.

In this framework, Nuovo Pignone Bari, a leader company in pump manufacturing, has showed a strong interest in studying the behaviour of its machines operating as turbines, by funding the present PhD research project, supported also by an abroad research period at the Graz University of Technology.

1.2 Objectives

In order to investigate the behavior of centrifugal pumps operating in reverse mode, the present research project aims to:

- Set-up a closed-loop test rig for experimental studies on hydraulic pumps and turbines at the Department of Mechanics, Mathematics and Management (DMMM) of the Polytechnic University of Bari, in order to experimentally support the theoretical studies on PaTs;
- Develop an experimental model with a general applicability for the prediction of the BEP of PaTs, as a selection tool for users;
- Develop a 1-D model for the prediction of the entire characteristic, as a design tool for manufactures, in order to improve the pre-existing prediction model by Nuovo Pignone;

- Perform a preliminary technical assessment of a real case study for the installation of a PaT: the water distribution network of the town of Casamassima (BA), located in Puglia (Southern Italy);
- Develop a theoretical approach to predict PaT performance with a two-phase flow, whose expansion characteristics are known.

1.3 Thesis Structure

The thesis is organized in eight chapters, as follows:

- **Chapter 1** introduces the research theme project with its motivations and objectives;
- **Chapter 2** describes the background on different topics of PaTs, as the first theoretical studies, technical and economic aspects in installation and performance prediction models;
- **Chapter 3** shows the closed-loop test rig for hydraulic turbomachinery and describes the methodology used to set-up the hardware and software architecture, useful to remotely perform experimental tests;
- **Chapter 4** outlines the experimental results of a KSB PaT, tested in direct and reverse mode at the test rig;
- **Chapter 5** illustrates the two proposed prediction models: (i) an experimental model for the prediction of the BEP of PaTs, as a selection tool for users; (ii) and another 1-D model for the prediction of the entire characteristic, as a design tool for manufactures;
- **Chapter 6** reports a preliminary assessment of the installation of a pump as turbine in a real water distribution network;
- **Chapter 7** presents a theoretical approach to predict the PaT performance with a two-phase flow, whose expansion characteristics are known;
- **Chapter 8** summarizes the conclusions of the thesis and recommendations for future works.

Chapter 2

Background

2.1 The Dawn of Pumps as Turbines

The oldest PaT seems to be the one installed in Orchard Mesa, USA, in 1926 [3]. It is remarkable how this study is still of considerable interest to the scientific community, even after almost a century. The natural development of engineering technologies has been characterised by constant improvement of the know-how on PaTs, that has not reached a revolutional stage yet. In 1931, Thoma and Kittredge [4] accidentally realized that pumps could operate very efficiently in the turbine mode while they were trying to assess the complete characteristics of pumps [5]. Later in 1941, Knapp [6] published the complete pump characteristics for pump design based on experimental investigations.

In 1957, Stepanoff [7] proposed one of the first correlations to predict the BEP in turbine mode. In 1967, Ruggiero [8] focused on a theoretical dissertation about the flow patterns inside axial pumps during direct and reverse mode, in order to provide design guidelines.

Some technical reports by international pump manufacturers, like Sulzer and KSB, started to be published in the the early 80's with Laux [9] [10], who studied reverse-running multistage pumps as energy recovery turbines in oil supply systems; Apfelbacher et al. [11] studied the application of a PaT in a reduction pressure station in Aachen (Germany).

2.2 Advantages and Drawbacks of PaTs

The study of the background on PaTs points out advantages and drawbacks of this technology. On one side, PaTs can be a cost-effective alternative to conventional turbines because of:

- Low cost compared to conventional and customized hydraulic turbines;
- Low mechanical complexity;
- Availability on the market for a wide range of heads and flow rates, hence specific speeds;
- Availability on the market in a large number of standard sizes;
- Easy installation;
- Short pay-back period in the range $1 \div 500$ kW [12].

On the other side, PaTs show a series of drawbacks in different aspects:

- Pump manufacturers do not usually offer performance curves of their pumps in reverse mode, since this requires testing of the machines also in turbine mode operation, hence increasing significantly their costs;
- Uncertainty of prediction methods for the turbine mode operation;
- Their efficiencies are lower than conventional turbines;
- Insufficient knowledge about their off-design operating conditions;
- Normally not equipped with the flow regulating guide vanes, which could improve performance at off-design operating conditions.

2.3 Application Areas

In the hydraulic area, the hydroelectric sector concerns power plants of the order of hundreds of megawatts, which are located in some well-defined places on the planet thanks to the availability of suitable pressure drops and adequate flow rates. In addition to this field, the interest in water distribution networks (WDNs) is beginning to be strong. Indeed, it is often necessary to insert pressure dissipation points inside the WDNs in order to reduce leakages, sometimes very high especially during the night, since the water drinking demand is insignificant and consequently the pressure in the network reaches maximum levels. To this end, the water management authorities are partitioning water distribution networks into District Metering Areas (DMAs) and installing an ever-increasing number of pressure reduction valves (PRVs) in well-specific points useful to control daily pressure pattern. The replacement of pressure reducing valves with pico- or micro-hydropower plants could be a feasible practice to achieve an effective pressure control with energy recovery [13]. The preliminary selection of the PaT is fundamental to find the best suitable machine for a specific site. Several works, based on empirical correlations, have been proposed: Barbarelli et al. [14] proposed a procedure starting by the specific speed requested by the site, Pugliese et al. [15] presented a procedure for the preliminary selection of a PaT, based on the design of the main parameters (the head drop and the produced power at the BEP, the impeller diameter and the rotational speed) to maximize the power output and regulate the exceeding pressure. However, the insertion of a PaT must consider the variability of water demand that is fundamentally a stochastic process [16]. A similar hydraulic variability in a water distribution network does not permit to define a unique operational point for a PaT and this aspect is a further obstacle for the functional planning of a similar system. Generally, the backpressure remains almost constant, as it must guarantee the satisfaction of the users during the day, whereas the upstream pressure depends on the flow rate pattern. For the sake of clarity, while the backpressure is defined by the pressure reduction valve on adequate values to guarantee the downstream water demand, upstream it can be observed extremely different conditions, which are based on the user demand random variability. In order to guarantee off-design conditions, Carravetta [17] proposed to adopt different regulation methods: Hydraulic Regulation (HR), Electrical regulation (ER) or both modes. The first (HR) can be performed by installing a by-pass line and a series PRV downstream the PaT. The former is used when the flow rate exceeds the design operating point, the latter is used for flow rates lower than the design operating point to regulate the excess of head. The

second mode (ER) modifies the rotational speed in order to change the PaT characteristic curve. Finally, the last permits the best compromise between hydraulic conditions and PaT mechanical efficiency by combining both previous modes.

For these reasons, the hydraulic field is the main application area where PaTs are installed. Many works asses the installation of PaT into Water Distribution Networks (WDN) in order to save energy dissipated by pressure reducing valves (PRVs). The common technical solution, depicted in Fig. 2.1, is to install the PaT in parallel with the pre-existing PRV.

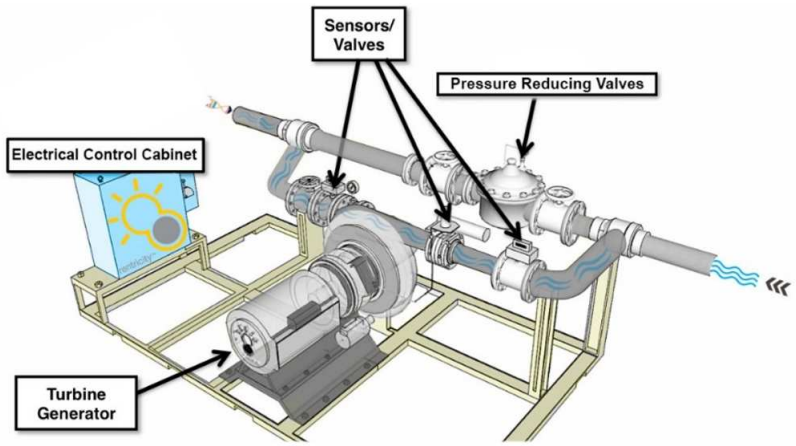

FIGURE 2.1: Example of a PaT installation in a Water Distribution Network [18].

Muhammetoglu et al. [19] implemented a full-scale PaT application into a real WDN in Turkey for energy production and pressure reduction; Rossi et al. [20] evaluated the potential of the PaT installation for the WDN of Merano (Italy). Balacco et al. [21] considered to replace existing PRVs with a PaT in the WDN of Casamassima (Italy) in order to supply a recharging point for electric vehicles on site. Alberizzi et al. [22] focused on the PaT speed regulation control in order to guarantee the BEP working condition of a PaT, which has to be installed in a branch of the WDN located in Laives (South-Tyrol - Italy). Du et al. [23] analyzed micro-hydro power generation from water supply system in high rise buildings in Hong Kong, by using a PaT.

PaTs fulfill an important role in hydraulic pumped-storage plants. As explained by Ciocan et al. [24] , when power demand is at its peak, water is released through the turbines to generate electric power. As the demand decreases, a large amount of electric power is available on the grid. With its ability to pump back water from the lower into the higher reservoir the plant acts like a giant rechargeable battery, using readily available power to provide reliable and flexible power to cover peak demand. The same power lines, connected to the power transmission grid, will provide the electric power required to pump back water, and transport the power generated by the plant when it is operating in turbine mode (Fig. 2.2). The environmental impact of this operation mode is neutral for a "green-energy" production point of view.

Furthermore, PaTs can represent stand-alone small hydro systems in all that remote communities, where the grid connection is not economical and/or practically possible. In this case, PaTs can satisfy the energy demand by exploiting natural

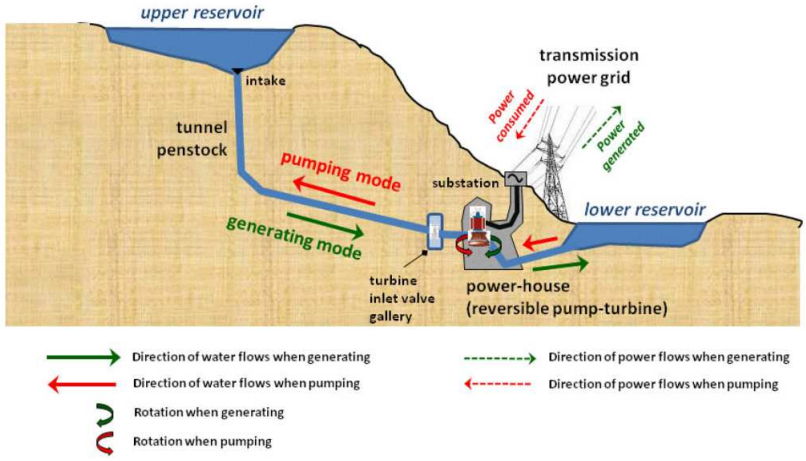

FIGURE 2.2: Example of a Pumped-Storage Power Plant [25].

water sources, as depicted in Fig. 2.3. For example, Arriaga [26] proposed the installation of a PaT in a village of Lao Democratic Republic and highlighted the cost-effective solution for rural electrification which can be installed, commissioned, and maintained by local technicians.

FIGURE 2.3: Example of an axial PAT for rural eletrification [27].

PaTs found applications not only in hydraulic areas, but also in other fields of the process engineering. These studies were carried on during the last two decades of the 20^{th} century, when engineering was mainly driven by the petroleum economy. For example, Laux [9] [10] studied reverse-running multistage pumps as energy recovery turbines in oil supply systems; Apfelbacher et al. [11] studied the application of a PaT in a reduction pressure station in Aachen (Germany). Semple et al. [28] investigated various arrangements of PaT installation with their design problems in a hydrocracker unit. Gopalakrishnan [29] analyzed PaTs in process industry applications. Furthermore, Raja [30] and Bolliger [31] examined pumps as turbine in reverse osmosis plants in the early '80s. Moreover Bolliger focused on PaTs in a gas washing plant [32] in 1997. Finally, Van Antwerpen [33] proposed a system that uses a reverse-running multistage pump acting as a turbine to do simultaneous pressure regulation and pressure recovery in secondary cooling water systems in deep mines.

2.4 Performance Prediction Models

PaTs are considered a cost-effective alternative to traditional turbines as long as their turbine mode performance can be predicted. Because of the lack of experimental data, a consistent effort was made by several authors in the prediction of PaT performance not only with theoretical approaches, but also with experimental campaigns of pumps tested in reverse mode. For example, Amelio et al. [34] in 1997 built a test rig to test pumps in reverse mode and to compare prediction models in literature. Other experimental activities were also performed by Barbarelli et al. [14], Derakhshan and Nourbakhsh [35], Nautiyal et al. [36], Pugliese et al. [37], Rossi et al. [20], Singh and Nestmann [38], Shi at al. [39], Yang et al. [12], Tan and Engeda [40], Carravetta et al. [41].

As showed in Fig. 2.4, there are two groups of prediction models in the technical background: on one side, users would select the best PaT for their specific application. Indeed, users could retrieve only information from the pump data sheet (flow rate, head and efficiency). On the other side, pump manufacturers need of a tool that could support them to predict the turbine mode performance by knowing pump characteristics, in order to be competitive on the market. Indeed, manufacturers have detailed geometric information of their machines that could be useful in the development of more accurate models.

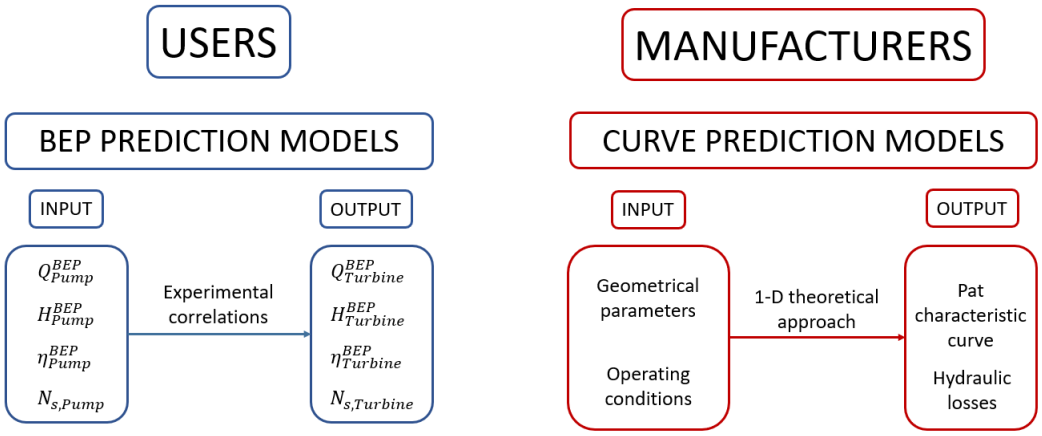

FIGURE 2.4: Prediction models for PaT performance.

The common target was to develop models, able to predict PaT performance by knowing the pump main characteristics. The relation between turbine and pump BEP performance are usually given in terms of head and discharge correction factors: $h = H_{BEP,T}/H_{BEP,P}$ and $q = Q_{BEP,T}/Q_{BEP,P}$. At the beginning, these models were mainly focused on the turbine BEP. In particular, focusing on PaT BEP, there are mainly two groups of prediction models: authors as Williams [42], Sharma [43], Alatorre [3] and Yang et al. [12] used methods based on the pump efficiency at BEP, $\eta_{BEP,P}$, whereas others as Derakhshan and Nourbakhsh [35], Singh and Nestmann [38], Nautiyal et al. [36], Tan and Engeda [40] and Barbarelli et al. [14], used methods based on the pump specific speed number, $N_{s,P}$. Tab. 2.1 summarizes some of these models in chronological order and proves that this topic is still nowadays object of research.

These investigations, carried out in periods with a lack of experimental data in literature, have been useful to create a basis for the developing of future models. Indeed, these prediction models are extremely simple but seldom consider off-design

TABLE 2.1: Some BEP prediction models in literature.

Year	Researcher	Method	$h = H_{BEP,T}/H_{BEP,P}$	$q = Q_{BEP,T}/Q_{BEP,P}$
1957	Stepanoff	$\eta_{BEP,P}$	$\frac{1}{\eta_{BEP,P}}$	$\frac{1}{\eta^{0.5}_{BEP,P}}$
1985	Sharma	$\eta_{BEP,P}$	$\frac{1}{\eta^{1.2}_{BEP,P}}$	$\frac{1}{\eta^{0.8}_{BEP,P}}$
1994	Alatorre	$\eta_{BEP,P}$	$\frac{1}{0.85\ \eta^{5}_{BEP,P}+0.385}$	$\frac{0.85\ \eta^{5}_{BEP,P}+0.385}{2\ \eta^{9.5}_{BEP,P}+0.205}$
2012	Yang	$\eta_{BEP,P}$	$\frac{1.2}{\eta^{1.1}_{BEP,P}}$	$\frac{1.2}{\eta^{0.55}_{BEP,P}}$
2008	Derakshan	$N_{s,P}$	$0.0233\ N_{s,P} + 0.6464$	$0.9413\ N_{s,P} + 0.6045$
2009	Singh	$N_{s,P}$	$f(N_{s,P})$	$f(N_{s,P})$
2011	Nautiyal	$N_{s,P}$	$41.667\left[\frac{\eta_{BEP,P}-0.212}{\ln N_{s,P}}\right] - 5.042$	$30.303\left[\frac{\eta_{BEP,P}-0.212}{\ln N_{s,P}}\right] - 3.424$
2016	Tan	$N_{s,P}$	$f(N_{s,P})$	$f(N_{s,P})$

points. Furthermore, these models show a low applicability, showing a deviation around $\pm 20\%$ from experimental results and being usually based on experimental correlations from a limited number of samples.

Theoretical models are based on the geometry of the machine and some complex phenomena like hydraulic losses. These methods are quite comprehensive but they are difficult to be applied in practice because they necessitate very detailed geometric information, which is sometimes available only to the manufacturers. Some researchers, such as Gülich [44] and Barbarelli et al. [45], developed theoretical approaches in order to predict PaT performance by taking into account velocity triangles, hydraulic losses on simplified geometries rather than using statistical and experimental correlations. However, the simplification of the geometry of impeller channel or volute could determine errors in terms of performance prediction.

Flow field through the PaT runner was investigated by taking into account the slip phenomenon. Ventrone [46] was one of the first to focus on this topic. As shown by Ventrone, the relative velocity vectors at the outlet of a centripetal turbine, e.g., Francis turbine and PaT, are subject to a deflection with respect to the blade congruent angle. Ventrone and Shi et al. [47] justified this by demonstrating the presence of fluid flow vorticity between the blades in planes orthogonal to the rotational axis. Thus, a counter rotating vortex compared to the angular velocity is present inside the impeller channels. Although this first works, this phenomenon has been often neglected in the development of the prediction models.

2.5 CFD Investigations

As evidenced by Binama at al. [48], many researchers have shown that CFD analysis is a reliable tool to predict the behavior of a pump operating as a turbine and to

estimate the performance curves of the turbomachinery. With CFD, complex fluid flow behaviors inside the PAT can be virtually previewed, which can substantially reduce both the design time and cost. A big number of studies have been carried out aiming at PAT flow characteristics understanding and performance prediction.

Capurso et al. [49] performed numerical simulations in order to investigate slip phenomenon at the outlet section of the runner. He introduced a fluid dynamic parameter ($\sigma_{turbine}$ – slip factor), whose definition is comparable to the slip factor occurring in the centrifugal pumps. This parameter accounts for the difference between the actual work and the theoretical one, due to the reduced number of the blades in PaTs compared to conventional turbines (e.g., Francis turbines). This fluid dynamic parameter provides a great support in developing and tuning 1-D models for the prediction of the turbine performance.

Singh and Nestmann [50] [51] proposed various possibilities of modifying the pump geometry to improve the performance in turbine mode: rounding the impeller, modifying the inlet casing rings, enlarging the suction eye, removing the casing eye rib. It was revealed that, among the different modifications proposed, the impeller blade rounding was the most beneficial [5].

Wang et al. [52] carried out theoretical, experimental, and numerical study of special impeller in order to improve the performance in turbine mode of a centrifugal pump.

Su et al. [53] investigated numerically a potential multistage PaT system with load pump in order to predict performance under both constant and variable speed conditions.

Li [54], Rossi et al. [55] investigated by means of numerical simulations the effect of viscosity on the performance of PaTs.

Nielsen and Olimstad [56] [57] [58] focused on the stability problems of PaT in pumped storage hydropower plants during their turbine mode operation. These instabilities, not present in a conventional Francis turbines, depend on the turbine design and more specifically on the geometry of the runner inlet. They investigated the effect of the variation of the leading edge on the characteristic curve in turbine mode by means of CFD simulations. Moreover, a theoretical approach was proposed in order to use turbine characteristic curves in system dynamic simulation.

2.6 PaT with Two-Phase Flow

The interest in pumps as turbine with two-phase flow starts during the 80's with some technical reports on first theoretical and experimental studies. All these models were based on the main assumption of the homogeneous flow in which two phases could be sufficiently well mixed and therefore the disperse particle size sufficiently small to eliminate any significant relative motion.

Gülich [44] was one of the first to study this issue. He tested a three-stage pump in reverse mode with an air/water mixture and he proposed a model to predict the performance in turbine mode during two-phase flow conditions. The model considers an isothermal flow and correlates the two-phase performance to the single-phase operating conditions by means of two empirical factors, $f_\psi = \psi_{2P}/\psi_{1P}$ and $f_\eta = \eta_{2P}/\eta_{1P}$, which depend on the void fraction α:

$$f_\psi = \frac{\psi_{2P}}{\psi_{1P}} = 1 + 0.45\alpha \tag{2.1}$$

$$f_\eta = \frac{\eta_{2P}}{\eta_{1P}} = 1 - 0.55\alpha - \alpha^3 \tag{2.2}$$

Gülich assumed that up to a void fraction α of about 80 %, the gas mass fraction is negligible compared to that of the liquid, and the temperature remains roughly constant. In addition to this, effects of liquid evaporation or gas desorbing are neglected and both the phases are considered separately. As a consequence of these assumptions, the isothermal specific work from the inlet pressure, p_2, to the outlet pressure, p_1, of each stage is computed by summing the contribution of both phases, as stated in equation 2.3. The liquid and the gas contributions are weighted by the corresponding mass fractions, x.

$$Y_{isoth.} = (1-x)\frac{p_2 - p_1}{\rho_L} + xRT \ln \frac{p_2}{p_1} + \frac{c_2^2 - c_1^2}{2} \tag{2.3}$$

Once the specific isothermal work is computed, Gülich proposed to calculate the equivalent head per stage with single-phase liquid flow by means of the empirical factor f_ψ:

$$\psi_{1P} = \frac{\psi_{2P}}{f_\psi} = \frac{2Y_{isoth.}}{N_{stages}\, u_2^2\, f_\psi} = \frac{2Y_{isoth.}}{N_{stages}\, u_2^2\, (1 + 0.45\alpha)} \tag{2.4}$$

By means of ψ_{1P}, the flow coefficient, φ, and the efficiency, η_{1P}, can be read from the single-phase characteristics. Using these values, the volumetric flow rate, Q, the efficiency η_{2P} and the power P_{2P} can be calculated:

$$Q = A_2\, u_2\, \varphi \tag{2.5}$$

$$\eta_{2P} = \eta_{1P} f_\eta = \eta_{1P}(1 - 0.55\alpha - \alpha^3) \tag{2.6}$$

$$P_{2P} = G\, Y_{isoth.}\, \eta_{2P} \tag{2.7}$$

Hamkins et. al [59] carried out an experimental characterization of an eight-stages pump running as turbine in a petrochemical plant under real production conditions. The flow within the turbine was in a two-phase condition from the inlet to the outlet. The exit void fraction ranged from 0.35 to 0.40 for these tests. They predicted the characteristic curve by treating the mixture as a homogeneous compressible fluid.

One of the most recent work in this field has been carried out by Visser [60], who computed the average density of the 2-phase mixture stage by stage and treats it as an incompressible mixture during each single-stage work calculation. First of all, the void fraction is experimentally known as function of the pressure. The total pressure drop is divided stage by stage in order to know the void fraction as function of the inlet and the outlet pressure of each stage. Once the mean void fraction of the stage is known, it is possible to calculate the density of the homogeneous mixture, ρ_{mix}. Then, the total work is obtained by summing the single specific works of each stage. Finally, it is possible to calculate the output power of the turbine by multiplying the specific work by the total mass flow rate and the turbine efficiency in two-phase flow conditions. The efficiency is obtained by means of the empirical correlation proposed by Gülich, as a function of the average void fraction. All of these models assume that the equilibrium gas volume fraction is established instantaneously.

The formation of gas bubbles requires time because the gas molecules must diffuse through the liquid and form a bubble. The equilibrium conditions in which two-phase density is a unique function of pressure, $\rho_{mix}(p)$, can only be established after a finite time. Gopalakrishnan [29] applied the analysis of Payvar [61] and determined that the bubble development time is of the same order of magnitude as the residence time in the turbine. The model calculates the bubble growth history in hydraulic turbines. The main assumptions are that the two-phase flow is homogeneous and one-dimensional, the pressure distribution is known *a priori* and the gas volume rate increases because of the growth of bubble and because of the generation of new bubbles at all solid surfaces in contact with the fluid stream.

2.7 Economical Analysis of PaT installation

An economic analysis permits to evaluate that a PaT installation is characterized by a payback period of few years [41]. Although the efficiency of PaTs is lower than the efficiency of conventional hydraulic turbines, PaT installations are recommended in view of their lower initial and maintenance cost. Some researcher applied different methods in order to justify the use of PaT by means of comparison of various project investments opportunities based on several financial parameters, the evaluation of various renewable energy options, cost analysis of hydro power plant by considering conventional turbines as well as an equivalent PaT.

Maher et al. [62] carried out a cost comparison of different off-grid electricity generation option (i.e. PaT based pico-hydro plant, the solar home system and the battery system in a rural area in Kenya). The annual life cycle cost and cost per kWh were worked out for different options by considering the installation cost, life of the system ad annual maintenance and operation costs. From the analysis, the PaT solution was found more cost effective than an equivalent solar power system.

Motwani et al. [63] carried out an annual life cycle cost analysis for 3 kW micro-hydropower plant, by comparing PaT with an equivalent Francis turbine. Based on the analysis, the annual life cycle cost was found 85 % less for PaT compared to Francis turbine.

Kramer et al. [64] proposed a new cost classification scheme cost in order to enable a systematic and generally valid estimation of investment costs of energy recovery plants. By using the net present value method, economic profitability of the installed energy recovery plant was investigated. The calculated net present value curves showed that the payback period for a complete feed-in is reached within a time period, where reinvestment is likely to be necessary. However, if the generated electricity contributes to the fulfillment of the own demand, the payback periods drop significantly and a positive indication for the investment decision is given.

Finally, Balacco et al. [21] considered to replace existing PRVs with a PaT in the WDN of Casamassima (Italy). A horizontal single-stage centrifugal pump was selected and an installation scheme was defined with a hydraulic regulation, constituted by a bypass valve and a control system, which permits the electric regulation varying the PAT rotational speed. An empirical correlation from the literature, based on the Best Efficiency Point (BEP) in direct mode, was adopted for the definition of the PAT characteristic curve and assuring necessary backpressure to satisfy water demand. It was verified how a PAT system can generate about 157 kWh/day and an average power of 6.57 kW considering a conservative PAT efficiency equal to 0.7. If compared with a conventional turbine, PaT solution can involve an annual income ranging from about 25,000 $euro/year$ to about 50,000 $euro/year$ or more depending

on the environmental benefits obtained like water saving due to pressure reduction by the PaT system.

2.8 Market status of Pat

Nowadays, water suppliers, operators of small hydropower plants and pump manufactures are accepting the idea of PaTs as an efficient way of generating energy from sources that would be wasted. Worldwide, many pump manufacturers have carried out research on PaT and supplied different types for power generation, water supply systems and other areas.

KSB is active in investing resources in PaTs by reaching incredible results. Indeed, KSB has already supplied PaTs for various applications like small hydropower plants ($\leq$ 10 MW), major water transport systems, reverse osmosis and industrial plants where the technology can be implemented as an alternative to throttling devices. KSB is active in supplying volute casing centrifugal pumps and ring-section pumps as turbine and ring, mostly in the small hydropower market. [65]

Andritz Hydro supplies its single-stage and multi-stage centrifugal pumps as turbine for different applications (i.e. recovery turbines in pulp and paper mills, in small hydropower plants) [66].

Finally, Baker Hughes, a GE company, mainly focuses on PaT for pumped-storage plants. Their pump turbine offerings are suited for heads from 5 m to 1.200 m and have production potential up to 15 MW [67].

Chapter 3

The Test Rig

A closed loop test rig for experimental tests and studies on hydraulic pumps, turbines and PaT was built by the Department of Mechanics, Mathematics and Management (DMMM) of the Polytechnic University of Bari during the PrInCE project (*Processi Innovativi per la Conversione dell'Energia*). The test rig, shown in Fig. 3.1, is located at the *Laboratorio di Ingegneria Costiera* (LIC), in Valenzano (Bari), of the Polytechnic University of Bari. At the same time, this test rig was built with the aim to provide an important facility for those pump manufacturers that would like to investigate more deeply their machine operations.

At the beginning of this work, the test rig was only built with its mechanical components, but it needed to be set up in terms of both hardware and software aspects. Indeed, the first target was to remotely control the test rig from a control room, separated from the Test Rig, because it was possible only to locally control it by means of a pre-existing PLC (Programmable Logic Controller) with its control panel. At this end, a hardware and software control system has been set up in order to physically interface all the measurement devices with the lab control system. Then, a real time LabVIEW software has been developed in order to remotely control the test rig. The creation of the Test Rig control system is described in the next sections.

FIGURE 3.1: View of the Test Rig.

3.1 Description of the Test Rig

The closed loop test rig allows one to test machines with a head up to 280 mH_2O, a flow rate up to 650 m^3/h, a rotational speed up to 2400 rpm and a power up to 480 kW. Due to the possibility to test pumps either in direct or in reverse mode, two hydraulic loops can be set by simply acting on manual On/Off valves, as shown in Fig. 3.2.

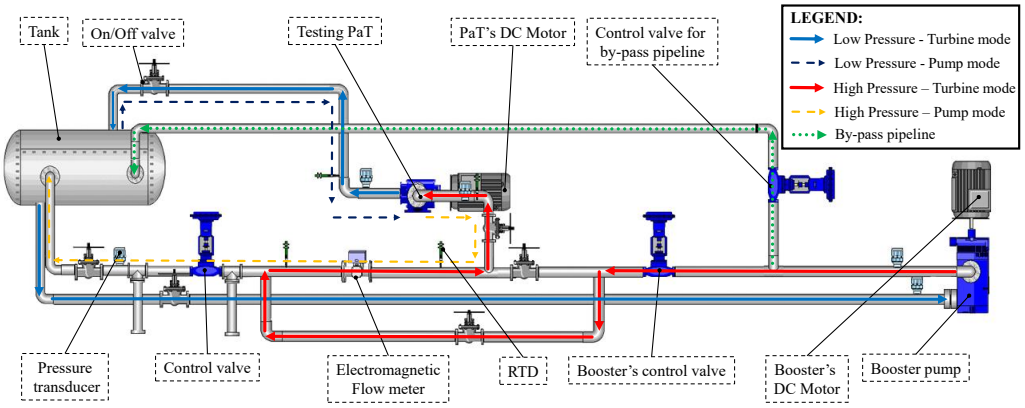

FIGURE 3.2: Layouts of the Test Rig.

In this layout, all the installed measurement devices can be evidenced. The PaT is installed in the test section, provided by a special platform with a rail system in order to be able to install hydraulic machines of different sizes. The machine is directly coupled with a DC motor of 480 kW that can work as motor during "pump tests" and generator during "turbine tests" . This is possible because a four quadrant AC/DC converter controls the electric DC motor at constant rotational speed, during pump mode, and at constant torque, during reverse mode.

During "turbine tests" , a booster pump (KSB Multitec D with max head 280 m, max flow rate 550 m^3/h, max power 516 kW, max rotational speed 2267 rpm and max efficiency 81.2%), driven by a second electric DC motor (identical to the previous one) and controlled only at constant rotational speed, supplies the hydraulic power for the testing of the PaT. In this case, the motor that drives the booster pump is partially supplied by the power produced by the PaT. The experimental setup for the characterization is constituted of a series of electronic measurement devices: an electromagnetic flow meter (Siemens Sitrans FM Magflow 3100 – accuracy 0.25%), four-wire RTD PT 100 for water temperature measurements, static (EH Cerabar S – accuracy 0.15%) and dynamic (PCB 113B21 – accuracy class 0.05%) pressure transducers down and upstream of both the PaT and the booster pump, a HBM T40B torque meter with integrated angular speed encoder characterized by an accuracy class of 0.05%.

Three electric regulation valves are installed in the piping. Two of them (C_v = 650 m^3/h), installed downstream of both hydraulic turbomachines, are used to regulate the discharge and the latter, installed on a parallel bypass pipeline, allows one to have a further degree of freedom in the regulation of the head and the discharge. Furthermore, the test rig is equipped with a surge tank with a capacity of 8 m^3 and an

air pressure control system that can increase the absolute pressure up to 11 $bar(abs)$. In the case of cavitation tests, a vacuum pump can reduce the tank absolute pressure down to 0.2 $bar(abs)$; a closed loop cooling system controls the water temperature. During tests, a real time LabVIEW software, implemented in this work and installed on a PC (inside the control room), allows the user to remotely control the DC motors, the control valves, and perform the data acquisitions. The PC is connected with a National Instruments master/slave hardware configuration: a master NI PXIe-8135 and two slaves NI 9144 chassis with C series I/O modules.

3.2 Components of the Test Rig

A series of mechanical components (tank, valves, turbomachines, electric machines) and electronic measurements devices constitute the test rig. All the components of the test rig are described in detail in the following paragraphs.

3.2.1 The Surge Tank

The test rig is equipped with a surge tank with a capacity of 8 m^3 (Fig. 3.3). It was designed according to the ASME Boiler and Pressure Vessel Code - Section VIII. It was filled with demineralized water.

FIGURE 3.3: View of the Tank.

The tank is equipped with a magnetic level indicator which consists of a series of two-color magnetic rollers, which are magnetically actuated by the movement of a float inside the instrument. When the tank is empty, the rollers show to the observer their white surface. As the level increases, the rollers rotate 180°, showing the red side. It also has a $4-20\ mA$ current output for monitoring the level of liquid in the tank remotely. Two magnetic switches are installed at the lowest and highest limit of the indicator for the "full" limit or "empty" limit (Fig. 3.4).

The tank is provided with an air pressure control system that can increase the absolute pressure up to 11 $bar(abs)$. In the case of cavitation tests, a vacuum pump can reduce the tank absolute pressure down to 0.2 $bar(abs)$; a closed loop cooling system controls the water temperature by means of a chiller (model AWA PROZONE 2260 by Thermocold [68]). The process water is taken from the tank and sent to the

outside via a circulation pump to the chiller unit, and then returned to the tank at the desired temperature (Fig. 3.5).

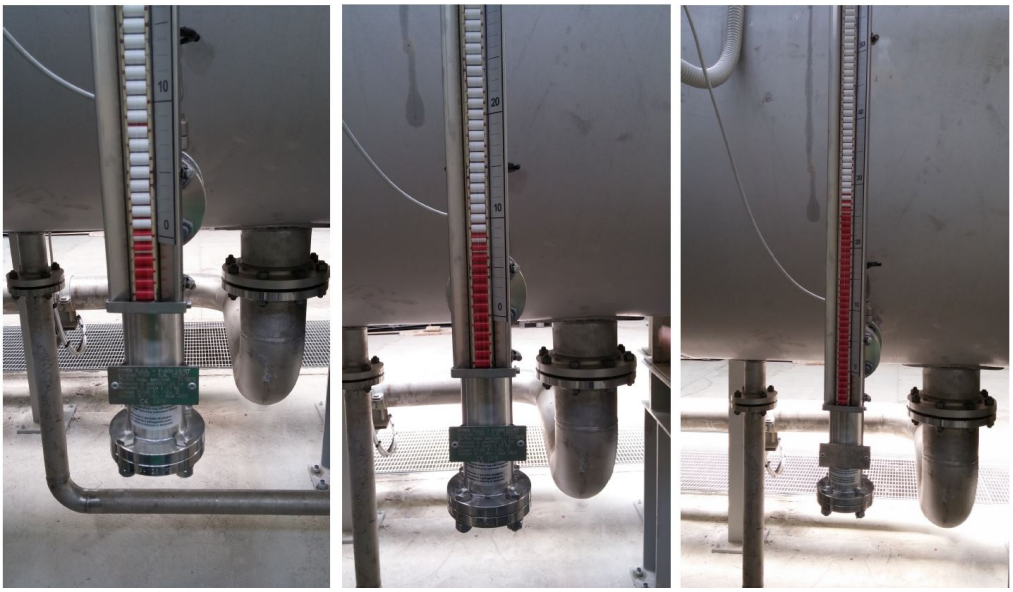

FIGURE 3.4: Magnetic water level indicator during tank filling procedure.

FIGURE 3.5: The Chiller unit (left) and the circulation pump of the cooling system (right).

3.2.2 Regulation Valves

Three electric regulation valves are installed in the piping (Fig. 3.6). These valves are manufactured by Bellino and they are equipped with electrical linear actuators Rotork IQML10. Two of them ($C_v = 650\ m^3/h$ and nominal diameter 8 ″), installed downstream of both hydraulic turbomachines, are used to regulate the flow rate and the latter ($C_v = 170\ m^3/h$ and nominal diameter 6 ″), installed on a parallel bypass pipeline, allows one to have a further degree of freedom in the regulation of the head and the discharge.

FIGURE 3.6: One of the three regulation valves of the Test Rig.

The type of trimming is different in the three control valves: a GVPC or a "parabolic contoured" globe valve, a GVVP or a "cage Vport" globe valve and a GVCH or "cage multihole" . The latter is located on the bypass pipeline.

The electric actuators needed to be powered at 230 *VAC* 3-phase, whereas the test rig was powered at 380 *VAC*. This means that a transformer with a primary of 380 *VAC* and a secondary of 230 *VAC* was required. For this reason, a transformer (Fig. 3.7), whose electric characteristic are summarized in Tab. 3.1, was selected and installed.

TABLE 3.1: Transformer characteristic.

Power	$2000VA$
Primary	$380\ V(\Delta)$
Secondary	$230\ V(Yn)$
Standard	IEC 61558-2-1
Dimensions	$237x120x215\ mm$

FIGURE 3.7: 380/230 VAC - 3 phase transformer.

3.2.3 Electric Motors and their equipment

Two identical DC motors drive respectively the testing machine and the booster pump. Each of them is characterized by an armature voltage equal to 550 V, with a power of 480 kW and 460 kW at respectively 1760 rpm and 2400 rpm, with an armature current of 919 A and 881 A. Both of them are cooled by two electric fans (Fig. 3.8). The DC motor coupled with the booster pump is equipped with a magnetic encoder bearingless Lika SMRI5 [69] (Fig. 3.9).

FIGURE 3.8: DC motor coupled with the KSB booster pump.

The DC motor coupled with the PaT is instead equipped with a flange torque meter with integrated angular speed encoder HBM T40B [70] ($C_{\max} = 3000\ Nm$, $N_{\max} = 2400\ rpm$ - accuracy class 0.05%), consisting of two separate parts: a rotor and a stator (Fig. 3.10). The rotor includes the measuring body and the signal transmission elements. Torque measurement is performed using strain gauges applied to the measuring body. Signals are sent and received by an annular antenna that can

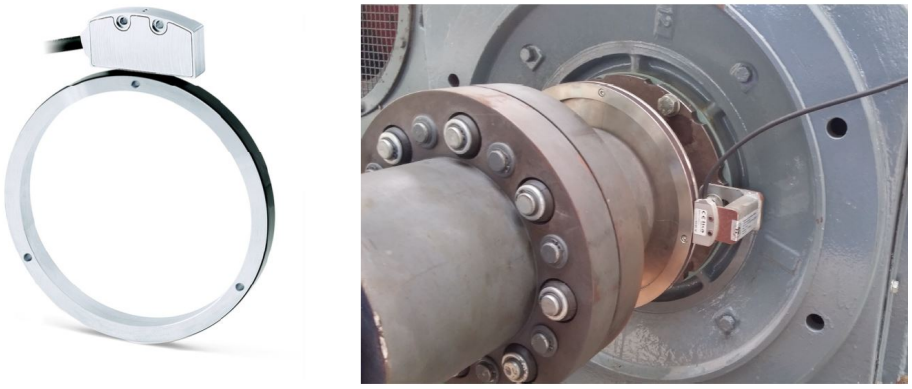

FIGURE 3.9: Components of the encoder (left) and the encoder installed on the DC motor shaft.

be divided into segments. The ring antenna is enclosed in a housing together with the electronics to adapt the voltage and condition the signal. The connecting pins of the torque signal, the supply voltage and the digital output are located on the stator. The torque measurement signal is a frequency modulated output at 5 V, while the speed measurement output signal consists of a sequence of pulses of 5 V.

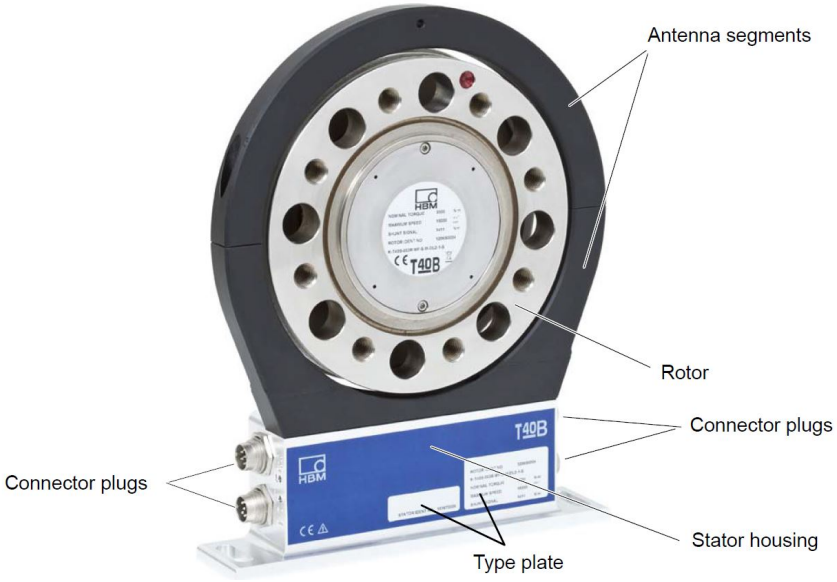

FIGURE 3.10: Torque meter with integrated angular speed encoder HBM T40B [70].

The torque meter is connected to two HBM MP60 signal conditioners, which transform the frequency input from the torque and speed measurement into an analog $4-20\ mA$ or $0-10\ V$ signal easier to manipulate (Fig. 3.11).

Both of DC motors are controlled by a four quadrant AC/DC converter Ansaldo Silcopac D with Graetz bridge rectifie (Fig. 3.11). The four quadrants operation mode offers the possibility of controlling the motor in direct and reverse mode. Indeed, the electric machine directly coupled with the PaT can work as motor during "pump tests" and generator during "turbine tests" .

FIGURE 3.11: HBM MP60 signal conditioners for torque and rotational speed signals (left) and AC/DC converter Ansaldo Silcopac D (right).

3.2.4 The Booster Pump

The booster pump, which supplies the hydraulic power for the testing of the PaT, is a 3-stages centrifugal pump KSB Multitec D with max head 280 m, max discharge 550 m^3/h, max power 516 kW, max rotational speed 2267 rpm and max efficiency 81.2% (Fig. 3.12).

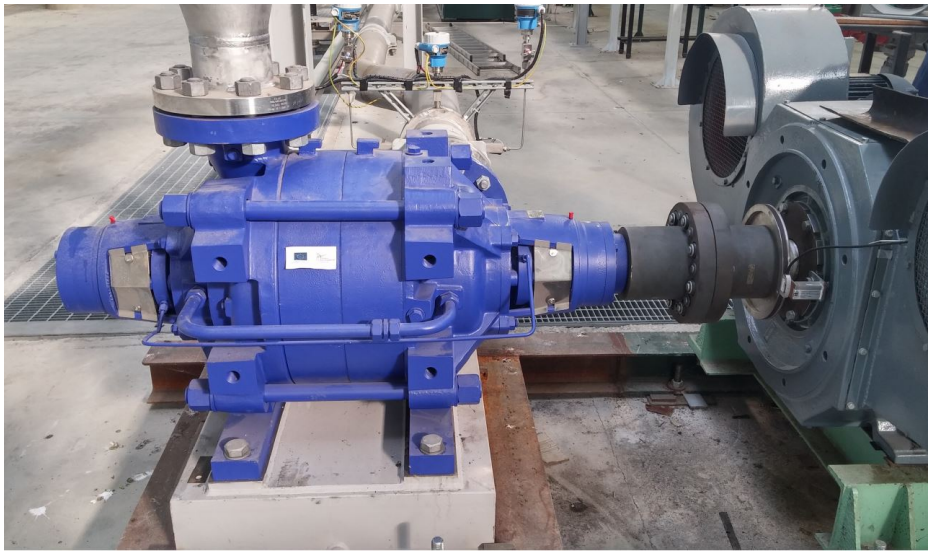

FIGURE 3.12: The booster pump of the Test Rig.

3.2.5 Electromagnetic Flow Meter

An electromagnetic flow meter (Siemens Sitrans FM Magflow 3100 – $Q_{\max}$ 1100 m^3/h – analog output $4-20$ mA – accuracy 0.25%) is installed for flow rate measurements. It is possible to measure the velocity of fluids having conductivity of at least 5 $\mu S/cm$.

3.2.6 RTD (Resistance Temperature Detector)

Four PT100 RTD (Resistance Temperature Detector) are installed in the field (Fig. 3.13). They are constituted by a thin layer of platinum and show a typical resistance of 100 Ω at 0 $^{\circ}C$.

FIGURE 3.13: PT100 RTD.

3.2.7 Pressure transducers

Two types of pressure transducers for monitoring and acquiring pressure are installed upstream and downstream of turbomachines:

- Piezoresistive transducers for the static pressure measurement;
- Piezoelectric transducers for the dynamic measurement of the static pressure.

The former are used to evaluate the static pressure values for low acquisition frequencies and guarantee an accurate measurement of the process value, while the latter are dynamic transducers for high frequency acquisitions.

The piezoresistive transducers installed in the field are EH CERABAR (accuracy 0.15%). Two models are installed because of their pressure operating ranges: M PMP 51 ($0-100$ *bar*) for high pressure sections (discharge section of the booster pump and testing machins), whereas model S PMP 71 ($0-40$ *bar*) for low pressure (suction section of both the turbomachines).

Each measurement section is constituted by three transducers, which are installed at 90° from each other in order to guarantee samples, even in the event of a failure of one of the sensors, without repeating the test (Fig. 3.14).

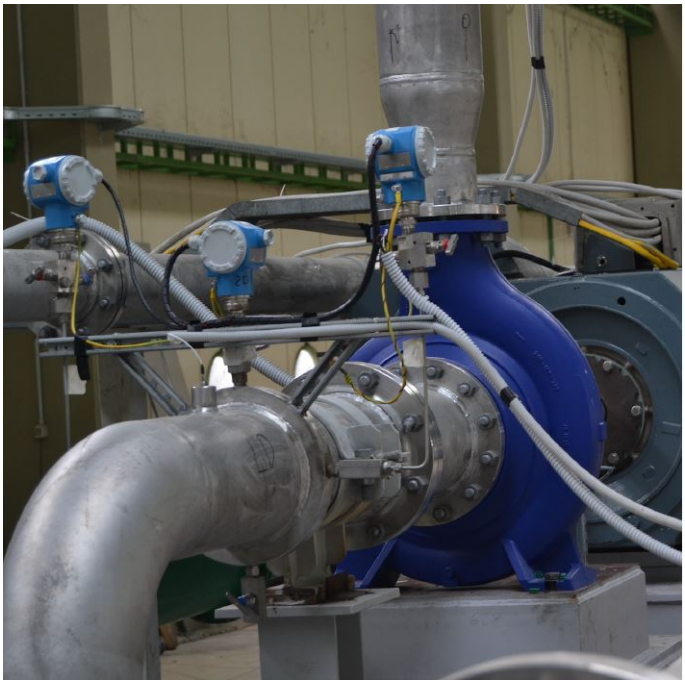

FIGURE 3.14: EH Cerabar pressure transducers installed downstream the testing PaT.

The piezoelectric dynamic transducers used are PCB-113B21 [71] with an operating pressure range $0 - 200$ *psi*, which corresponds to an output of ± 5 V, but can detect up to a pressure of 400 *psi* in over range producing an output of ± 10 V. Five PCB transducers are installed, one for each pressure measurement section. In order to install these devices, five tapping point were realized, as shown in Fig. 3.15

FIGURE 3.15: Dynamic pressure transducer installed and cabled.

3.3 Hardware Architecture

At the beginning of this work, the test rig was only built with its mechanical components, but it needed to be set up in terms of both hardware and software aspects. Indeed, the first aim was to remotely control the test rig from a control room, separated from the Test Rig, because it was possible only to locally control it by means of a pre-existing control panel . At this end, a hardware and software control system was set up in order to physically interface all the measurement devices with the lab control system. Then, a real time LabVIEW software was developed in order to remotely control the test rig. The creation of the Test Rig control system is described in the next sections.

3.3.1 Acquisition & Control Hardware system

A LabVIEW Realtime software runs on a PC, located in a control room. This software allows to start-up and remote control the test rig. Moreover, the control room allows, through a plexiglass glass, a visual control of the system and at the same time protects the operator from noise and moving parts (Fig. 3.16).

FIGURE 3.16: View of the Control room of the Test Rig.

The PC is connected with a National Instruments master/slave hardware configuration: a master NI PXIe-8135 and two slaves NI CompactRIO 9144 chasses with C series I/O modules. These components have been connected to each other by EtherCAT, a network communication protocol for typical real-time applications in automation field.

Two cabinets have been set up in order to contain all this hardware instrumentation: in the first cabinet the master NI PXIe-8135 has been allocated with its first slave NI 9144 chassis. The second NI 9144 chassis slave has been allocated inside another cabinet because of the need to place acquisition modules closer to the farthest sensors, to limit signal noise (Fig. 3.17).

FIGURE 3.17: Cabinets with hardware instrumentation: PXIe-8135 with one slave CompactRIO 9144 (left) and the second slave CompactRIO 9144 (right).

3.3.2 Master: NI PXIe-8135

The hardware architecture core is the NI PXIe-8135 controller [72]. It is an integrated controller based on Intel Core i7 CPU for PXI Express systems. This device is ideal for applications of modular instrumentation and data acquisition. The NI PXIe-8135 controller is housed within the NI PXIe-1078 chassis, which also is useful as an expansion module for other PXIe standard acquisition modules. Indeed, it includes a PCI Express connection for each of the 9 slots (Fig. 3.18). Five NI PXIe-4499 acquisition modules and two NI PXIe-8431/8 modules are plugged-in to the expansion chassis.

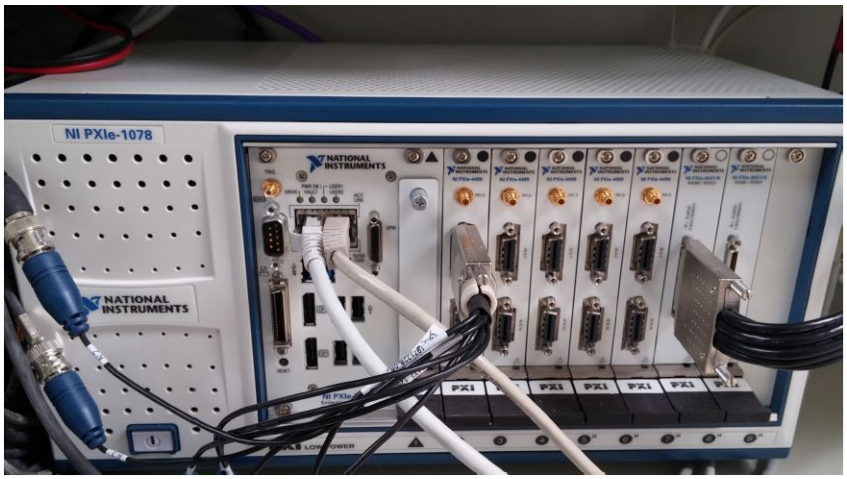

FIGURE 3.18: Cabinet with hardware instrumentation: NI PXIe-1078 chassis with NI PXIe-8135 controller.

NI PXIe-4499

NI PXIe-4499 are sound and vibration modules with a high number of channels with a resolution of 24 bits that allow to acquire up to 16 inputs simultaneously [73]. The 5 dynamic pressure transducers have been connected to the NI PXIe-4499 via the InfiniBand connector (module side) and BNC connector (sensor side).

NI PXIe-8431/8

Two NI PXIe-8431/8 modules occupy slots 6-7 and are high-performance interfaces for high-speed serial communication [74]. This module have been selected in order to control the three control valves, whose electric actuators communicate via the serial communication protocol "*Modbus*" by means of a "*Modbus module*", installed inside each actuator.

A "*half duplex*" connection was required by the "*Modbus module*". For this reason, it has been necessary to set the module with "*half duplex*" communication type. If this condition had not been implemented, it would not have been possible to communicate with the electric actuators.

The NI PXI 8431/8 module shows 8 serial channel RS-485, as indicated in Fig. 3.19.

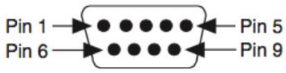

Pin	232 DTE	232 DCE	422/485
1	DCD[2]	DCD	GND
2	RXD	TXD	CTS+ (HSI+)
3	TXD	RXD	RTS+ (HSO+)
4	DTR[2]	DSR	RXD+
5	GND	GND	RXD–
6	DSR[2]	DTR	CTS– (HSI–)
7	RTS	CTS	RTS– (HSO–)
8	CTS	RTS	TXD+
9	RI[2]	RI	TXD–

FIGURE 3.19: RS-485 Pinout.

The highlighted pins are those involved in communication. These pins are indicated by the "*Modbus module*" of the actuators. Moreover, the "*loopback configuration*" has been carried out, according to the pinout of Fig. 3.20 in order to create a single reception and transmission channel.

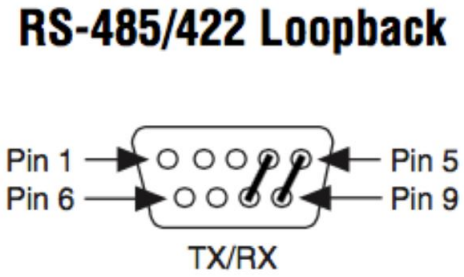

FIGURE 3.20: RS-485 Pinout in Loopback configuration.

Finally, pins 4 and 8 of the RS 485 port (PXI-e side) have been connected to the channel 1A (Rx/Tx +) of the actuators "*Modbus module*" , whereas pins 5 and 9 of the RS 485 port (PXI-e side) have been connected to the channel 1B (Rx/Tx -). Pin 1 with the "common" (COM).

3.3.3 Slave 1: CompactRIO NI 9144

Two CompactRIO NI 9144 chassis [75] are connected to the master NI PXIe-8135 via EtherCAT, as slaves. They offer the possibility of installing various I/O expansion

modules, as described in the following paragraphs.

The first CompactRIO Chassis is housed in the main cabinet (Fig. 3.21), above the PXIe instrumentation and has 8 slots:

- Slot 1: cRIO NI 9481 module;
- Slot 2: cRIO NI 9263 module;
- Slot 3: cRIO NI 9201 module;
- Slot 4: cRIO NI 9203 module;
- Slot 5: cRIO NI 9203 module;
- Slot 6/7/8: Empty.

FIGURE 3.21: The first CompactRIO Chassis with its I/O modules.

NI 9481 module

The NI 9481 module is a Relay Output Module [76]. This module is constituted by four relay. Two of them are used to send the "run" and "stop" commands to the DC motor coupled with the PaT, whereas other two relay are used to send the same commands to the DC motor coupled with the booster pump. The relay for the "run" command is normally open, whereas the relay for the "stop" command is normally close.

NI 9263 module

The NI 9263 module is a Voltage Analog Output Module with 4 channels, 16 bit resolution and an output range of $\pm 10\ V$ [77]. The 4 outputs provide a set point of rotational speed and armature current to the two DC motors, as voltage modulated signals.

NI 9201 module

The NI 9201 module is a Voltage Analog Input Module with 8 channels, 12 bit resolution and an output range of $\pm 10\ V$ [78].

Channels $1-6$ are used for rotational speed, armature current and armature voltage readings from both the DC motors. These real time readings are used for close-loop controls. Indeed, real time values of speed, current and voltage are compared with respect to their set points in order to reach the desired operating points.

Channels $7-8$ are connected to magnetic switches of the magnetic water level indicator, according to the wiring scheme of Fig. 3.22.

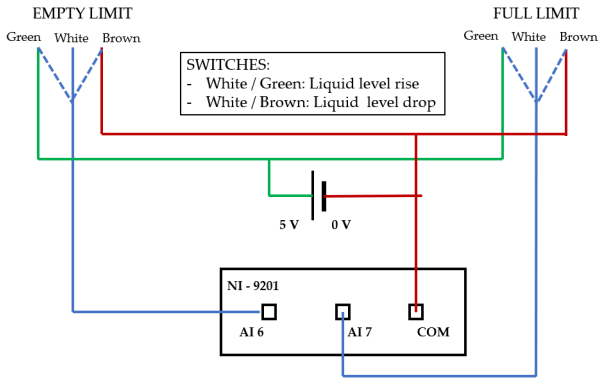

FIGURE 3.22: Wiring scheme for electromagnetic switches of the water level indicator.

NI 9203 module

The NI 9201 module is a Current Analog Input Module with 8 channels, 16 bit resolution and an output range of $\pm 20\ mA$ [79]. There are two 9201 modules with 16 total inputs, connected to 15 Cerabar pressure transducers (3 sensors for each of the 5 measurements sections). Transducers need to be supplied at 24 V and show a $4-20\ mA$ output signal. They have been connected according to the wiring diagram shown in Fig. 3.23.

3.3.4 Slave 2: CompactRIO NI 9144

The second CompactRIO Chassis is located inside the second cabinet (Fig. 3.24), and it is constituted by 8 slots:

- Slots 1/2: cRIO NI 9217 module;
- Slots 3/4/5: cRIO NI 9203 module;
- Slot 6/7/8/9 Empty.

NI 9217 module

The NI 9217 module is a PT100 RTD (Resistance Temperature Detector) with 4 channels, 24 bit resolution and an output range of $\pm 20\ mA$ [80]. It is used to measure the temperature by PT100 probes in the field. The PT100 probe was automatically recognized by the module.

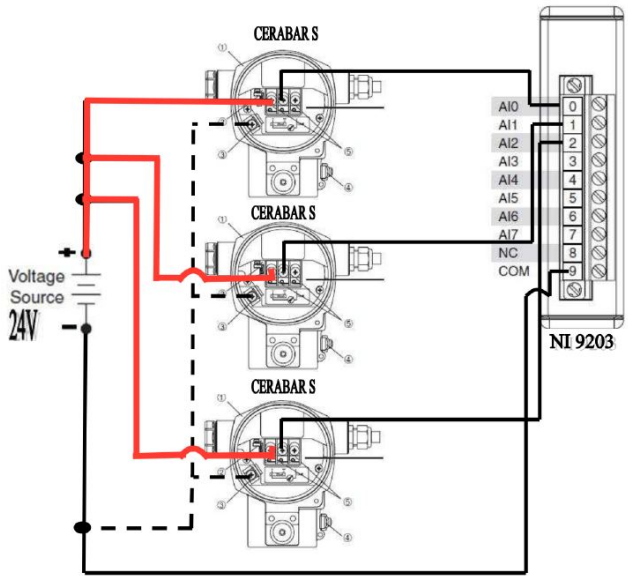

FIGURE 3.23: Wiring scheme of the Cerabar pressure transducer and the NI 9203 module.

A "four wires " wiring has been used: two wires supply the RTD and the other two transmit the signal. This method offers the advantage of not being influenced by the cable resistances, since the latter are on a high-impedance path that passes through the device during voltage measurement, making the measurement of voltage variation of the RTD more accurate, which is usually of the order of some mV.

NI 9203 module

The NI 9201 module is a Current Analog Input Module with 8 channels, 16 bit resolution and an output range of $\pm 20\ mA$. The channel 1 was used to read the flow rate from the electromagnetic flow meter, as a $4 - 20\ mA$ signal.

Channels 2 and 3 have been connected to the analog output of the two HBM P60. These two signal conditioners receive frequency impulses respectively from the torque meter and the encoder (installed on the shaft of the PaT), which are converted in $4 - 20\ mA$ signals that can be read by the NI 9203 module.

FIGURE 3.24: Second cRIO chassis with its I/O modules.

3.4 Development of the System Remote Control Software

After the creation of the hardware architecture, described in the previous sections, a real time NI LabVIEW software has been implemented in order to remotely control the test rig. The software has been installed on the PC in the control room. It allows to remotely control DC motors and control valves, acquire in real time and save measurements from all the instrumentation in the field. Moreover, it was created a Human Machine Interface (HMI) in order to let the user to perform a test by checking operating conditions in real time.

3.4.1 Introduction to LabVIEW

LabVIEW is a system-design platform and development environment for a visual programming language from National Instruments. LabVIEW is commonly used for data acquisition, instrument control, and industrial automation. The programming paradigm used in LabVIEW, sometimes called G, is based on data availability. Execution flow is determined by the structure of a graphical block diagram (the LabVIEW-source code) on which the programmer connects different function-nodes by drawing wires. These wires propagate variables and any node can execute as soon as all its input data become available. Since this might be the case for multiple nodes simultaneously, LabVIEW can execute inherently in parallel.

Virtual Instruments VIs

LabVIEW programs-subroutines are termed Virtual Instruments (VIs) because their appearance is similar to that of physical instruments. LabVIEW has a complete set of tools for data acquisition, analysis, visualization and storage. LabVIEW VIs have two main components:

- Front Panel;
- Block Diagram.

Front Panel

The front panel is the user interface of the VI and is constructed using controls and indicators that are the interactive inputs and outputs terminals of the VI, respectively. Controls can be knobs, buttons, and other devices that simulate input instrumental devices and provide data to the block diagram. Instead, the indicators are graphs, LEDs and other simulated output instrumental devices and display the data that the block diagram acquires or generates. Each control or indicator has a type of data associated with it and the most commonly used are numeric, boolean, and strings. The control palette contains, divided into the various menus, controls and indicators to be used to construct the front panel.

Block Diagram

The block diagram contains the graphical source code. All of the objects placed on the front panel will appear on the back panel as terminals. The block diagram also contains structures and functions which perform operations on controls and supply data to indicators. The structures and functions are found on the Functions palette and can be placed on the block diagram. Collectively controls, indicators, structures,

and functions are referred to as nodes. Nodes are connected to one another using wires, e.g., two controls and an indicator can be wired to the addition function so that the indicator displays the sum of the two controls. Thus a virtual instrument can be run as either a program, with the front panel serving as a user interface, or, when dropped as a node onto the block diagram, the front panel defines the inputs and outputs for the node through the connector panel. This implies each VI can be easily tested before being embedded as a subroutine into a larger program.

3.4.2 Creation of the LabVIEW Project

As first step, a project file has been created in order to contain all the developed VIs and the hardware configuration. As depicted in Fig. 3.25, the project tree is constituted by two main elements:

- My Computer: the PC where LabVIEW is installed and it works as interface between user and control system;
- NI-PXIe-8135: The hardware architecture core.

The master NI PXIe has been added in the project tree with its two two CompactRIO NI 9144, as slaves. For each CompactRIO chassis, it is possible to view all the I/O channels of all the C Series modules.

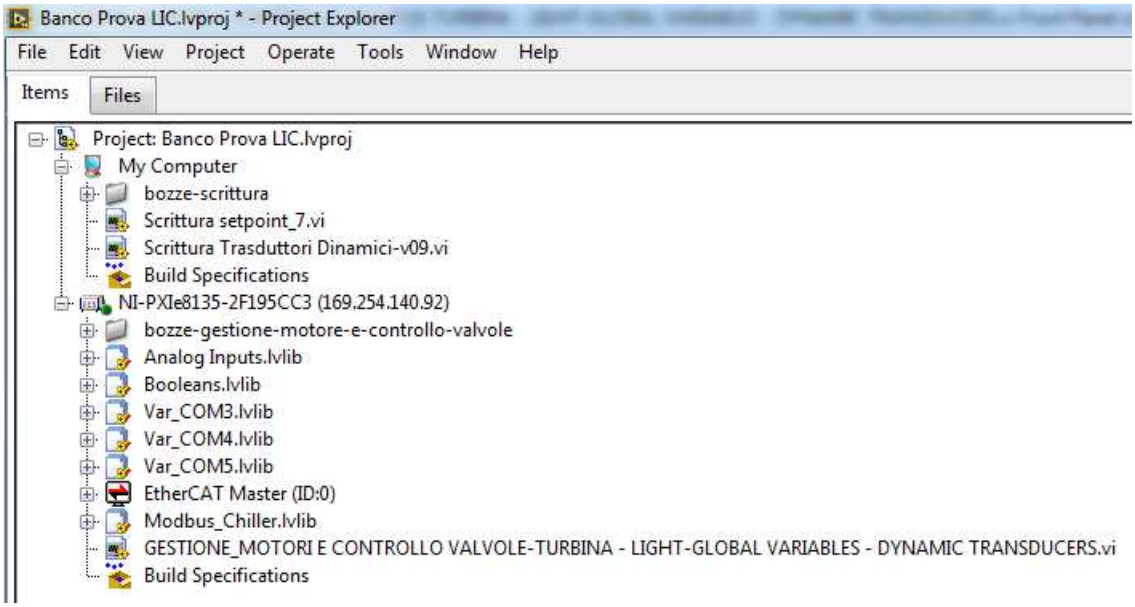

FIGURE 3.25: LabVIEW Project Tree.

The main idea was to run the acquisition and control software on the CPU of the NI-PXIe and to write all the acquired data on the PC. This solution guarantees the best controller performance in the management of the real-time software. Indeed, writing operations could slow down the execution. This idea has been decided in order to have a more performing system during experimental tests.

Fig. 3.26 shows how the software architecture has been implemented. A main VI, "*Gestione motori e controllo valvole.vi*", is constituted by two main subVIs which work in parallel: the first is based on a "*Scan Mode cycle*" in order to refresh in real time the system control variables and acquire data from the so-called "low" transducers,

whereas the second was developed in order to acquire data from dynamic pressure transducers at "high" frequency up to 20 kHz.

This choice is due to the different signal frequency rates. The "*Scan Mode cycle*" function updates the values of the I/O variables at a frequency up to 1 kHz, whereas the cycles for "fast" acquisition are performed at a frequency up to 20 kHz, in agreement with the NI 4499 specifications.

Each of them communicates with their respective *writer VIs* by means of *Network Streaming* functions in order to send and write data files. Each of these VIs will be described in detail in the next sections.

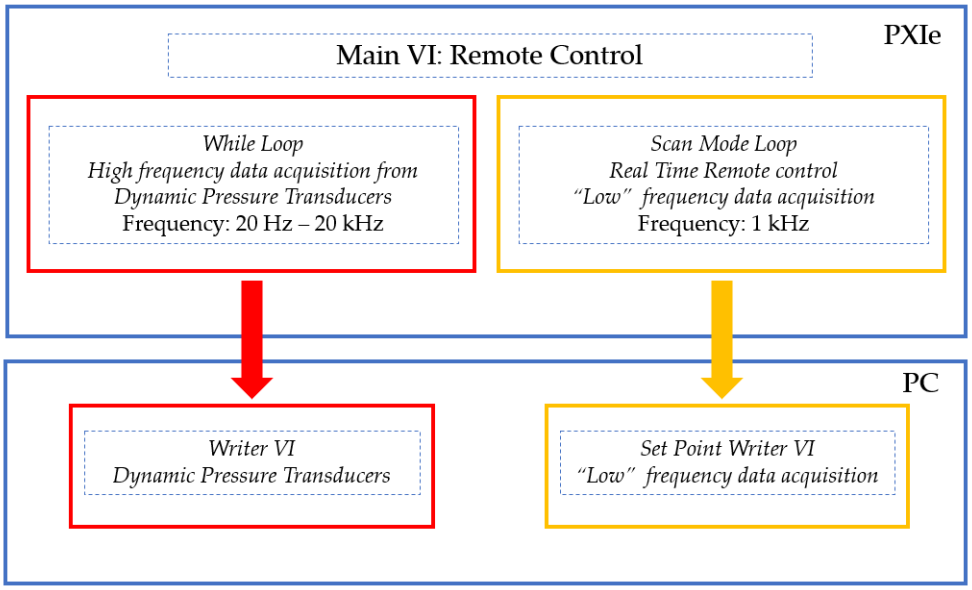

FIGURE 3.26: Architecture of the developed system remote control software.

3.4.3 Real-Time Remote Control VI

A main VI hsa been implemented in order to let the user to control all the variable in field in real-time. An *ad hoc* HMI has been created in the front panel of this VI, as depicted in Fig. 3.27. It represents the layout of the test rig with all its components. Moreover, the interface is provided with indicators and controls, which assist the user to read and control all the processing variable involved during a test, such as:

- Acting on the opening percentage of each control valve and read the actuator position;
- Start up DC motors by imposing the set points and read their parameters;
- Read all the measurements from the field.

Front Panel

The interface has been divided into several sections. In Fig. 3.28 it is possible to note the section dedicated to the management of DC motors, which are constituted by:

- Button "*marcia*": "start" command to the DC motor;

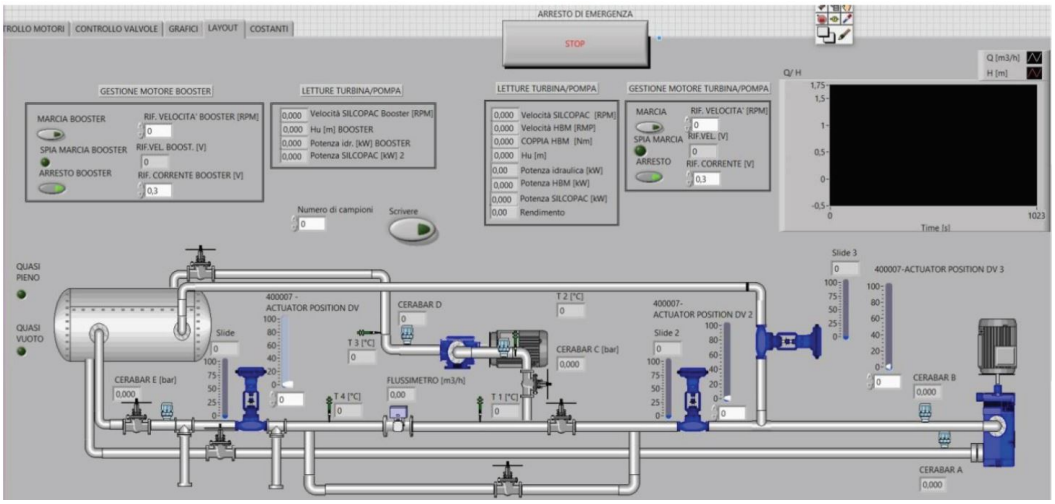

FIGURE 3.27: Front Panel of the Main VI.

- Button "*arresto*": "stop" command to the DC motor;
- Led "*marcia*": if the motor is running, it is turned ON;
- Control "*Riferimento velocità RPM*": desired DC motor Rotational speed set point;
- Indicator "*Rif. Vel. V*": indicates the speed set point converted in *V*;
- Control "*Rif. Corrente*": desired DC motor armature current set point.

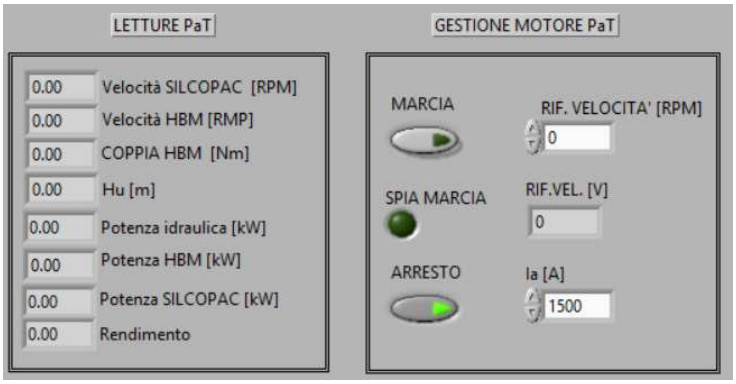

FIGURE 3.28: Detail of the DC motor control part of the main Block Diagram.

As depicted in Fig. 3.28, the "*stop*" buttons of both motors have a green led, which indicates that the relays inside the NI-9481 module are normally closed (NC). This is possible because both the relays have been set NC as default value. This has been done to allow the control of both motors even in local mode through the a pre-existing control panel. Therefore, thanks to the status of this relays, DC motors can be powered even when the LabVIEW program is not running. On the other hand, the "*start*" buttons have been set as normally open (NO). This means that when the program is running, DC motors start to run when these button are pressed.

Two sections, close to the previous ones, are dedicated to reading parameters related to the booster pump and the testing PaT, such as:

- "*Velocità Silcopac [RPM]*": it provides an average value of the rotation speed of the motor. This value is read by the PLC (Programmable Logic Controller) predisposed to the feedback control of the motors and consequently the value read in tension is numerically processed in the Block Diagram so that the end user has the speed reading in RPM;
- "H_u *[m]*": indicates the machine head;
- "*Potenza idraulica [kW]*": indicates the hydraulic power;
- "*Potenza elettrica [kW]*": indicates the electric power absorbed by the DC motor;
- "*Velocità HBM [RPM]*": indicates the rotational speed measured by the HBM encoder;
- "*Coppia HBM [Nm]*": indicates the torque measured by the HBM torque meter;
- "*Potenza HBM [kW]*": indicates the mechanical power absorbed (in pump test) or generated (in turbine test);
- "*Rendimento*": indicates the efficiency as the ratio between the hydraulic power and the mechanical power absorbed by the pump.

Block Diagram

The front panel just examined finds its corresponding code in the Block Diagram, which has been composed of a main temporized while loop, called "*Timed Loop*". All the I/O channels are refreshed in sync with the PXI Scan Engine (set to 1 *ms*). The while loop executes the code until the "*conditional terminal*", an input terminal present in the cycle, does not receive a specific Boolean value. In this case the "*conditional terminal*" is connected, via a wire, to a Boolean control which corresponds, in the Front Panel, to the "*emergency STOP*". The code implemented in the main "*Timed Loop*" was subdivided in several parts:

- "Start" and "Stop" commands: 4 Digital Outputs, two for each DC motor, connected to booleans controls "*marcia*" and "*arresto*" (Fig. 3.29);

FIGURE 3.29: Digital Outputs for Start and Stop commands.

- Booster Pump: 3 Analog Inputs read armature voltage, armature current and rotational speed of the DC motor coupled to Booster Pump in form of $0 - 10\ V$ from output channels of the Silcopac D. All the three readings are manipulated in order to let the user to read the same value with their unit of measurement (V, A and rpm). Then, the voltage value is multiplied by the current to obtain the electrical power, "*Potenza Silcopac [kW]*" (Fig. 3.30);

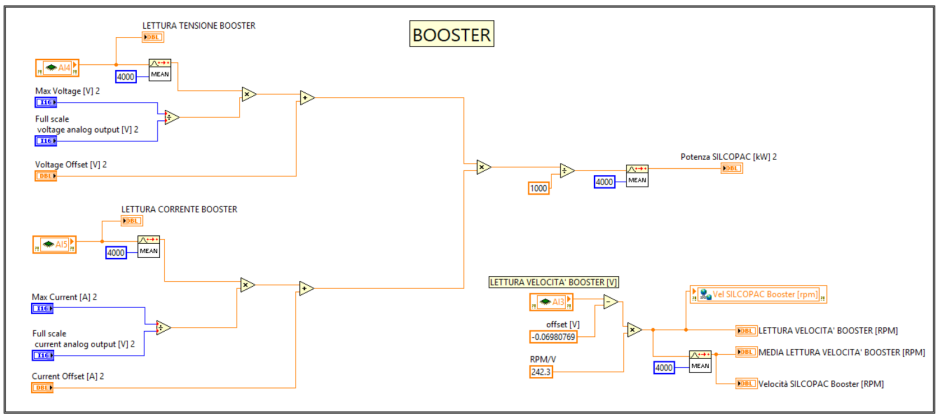

FIGURE 3.30: Block Diagram particular: Speed, current and voltage readings of the DC motor coupled with the Booster Pump.

- PaT: 3 Analog Inputs read armature voltage, armature current and rotational speed of the DC motor coupled to Booster Pump in form of $0 - 10\ V$ from output channels of the Silcopac D. All the three readings are manipulated in order to let the user to read the same value with their unit of measurement (V, A and rpm). Then the voltage value is multiplied by the current to obtain the electrical power, "*Potenza Silcopac [kW]*" (Fig. 3.31);

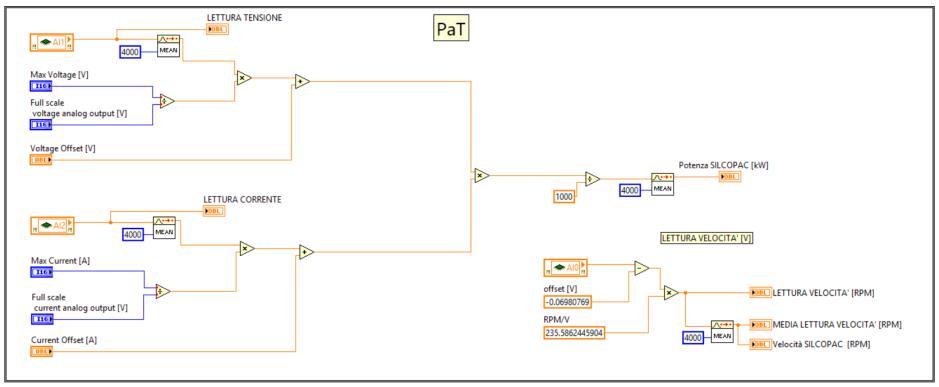

FIGURE 3.31: Block Diagram particular: Speed, current and voltage readings of the DC motor coupled with the PaT.

- Set Points: 4 Analog Outputs, two for each DC motor, for the rotational speed and armature current set points, which are manipulated in order to transform the set point in a $0 - 10\ V$ Analog Output to the PLC (Fig. 3.32);
- Electromagnetic Switches: 2 Analog Inputs from electromagnetic switches of the water level indicator of the tank. A case structure, which is the equivalent of a *if case*, lights up a led on the Front Panel to warn the user in the event that the water level in the tank reaches the "empty" or "full" limit (Fig. 3.33);
- Control Valves: three identical sections have been implemented for each control valve. Fig. 3.34 depicts one of the these three sections, where 7 variables have been connected to 7 LEDs in order to indicate several states of the valve (i.e. actuator moving, closed limit, running closed, open limit, running open, remote selected and local selected). These variables are taken from the variable library present in the project. Indeed, a serial Modbus type I/O server

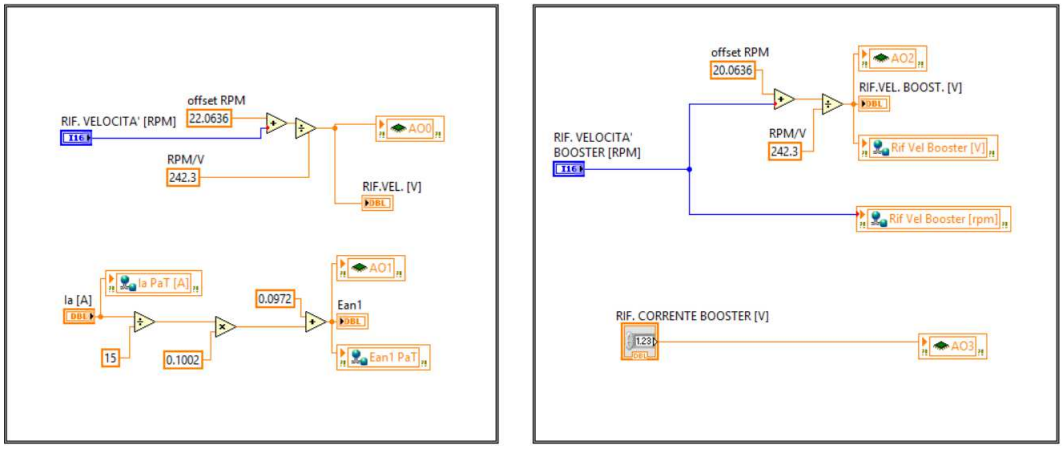

FIGURE 3.32: Block Diagram particular: Set points for the DC motor coupled with the PaT (left) and the Booster Pump (right).

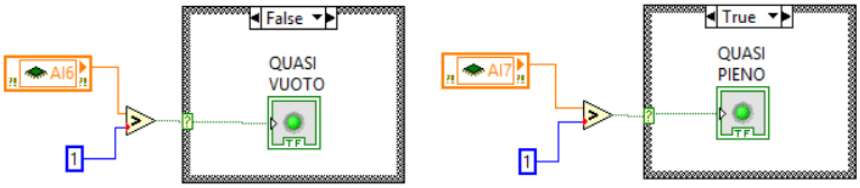

FIGURE 3.33: Block Diagram particular: Analog Inputs from electromagnetic switches of the water level indicator of the tank.

has been created in the project file, in order to create a serial communication with control valves. Fig. 3.35 shows the setup of the I/O Modbus server, which contains the variable libraries for each valve.

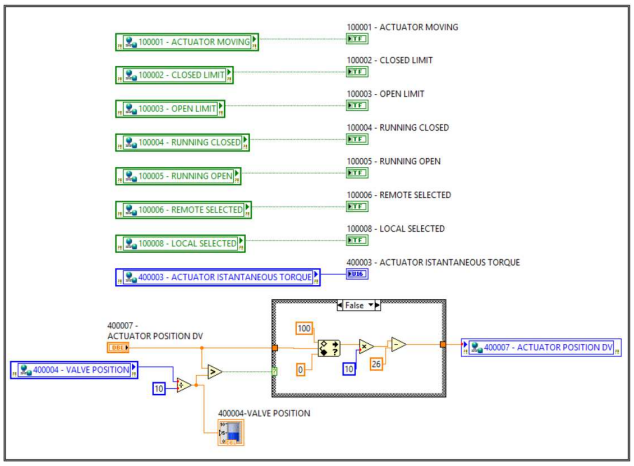

FIGURE 3.34: Block Diagram particular: Valve remote control.

Furthermore, there is a numerical indicator for the instantaneous torque value and a numerical indicator which shows the valve opening value. Below we find a numerical controller connected to a case structure. The input value for the case structure is given by the comparison between the set point and the current actuator position. If the desired value is greater than the current value, the case structure executes the *true* case, otherwise the *false* case. In both the

two cases a numerical conditioning of the input value is carried out in such a way that the valve opening value corresponds to the opening value desired by the user;

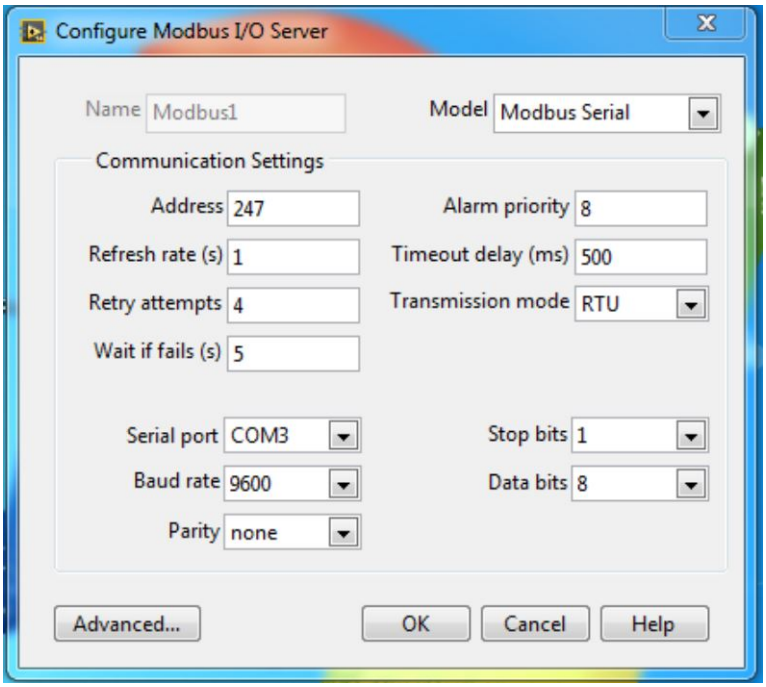

FIGURE 3.35: Block Diagram particular: Modbus I/O server setup.

- Data acquisition: a section in which signals are acquired from the different modules of the Compact Rio NI 9144. From Fig. 3.36 and Fig. 3.37, it is possible to see how the signals have been divided into different groups:
  - Pressure measured by all the 15 Cerabar in the field;
  - Temperature measured by the 4 RTD;
  - Flow rate measured by the electromagnetic flow meter;
  - Torque to the PaT shaft, measured by the torque meter;
  - Rotational speed of the PaT shaft measured by the encoder.

It is possible to notice from the previous figures how the signals were manipulated to obtain the parameters, useful for the study of the PaT and of the booster pump (head, hydraulic power, mechanical power and efficiency).

All the acquired signals are transmitted to another VI, which runs on the PC and writes acquired data on a TDMS file (Technical Data Management Streaming). Indeed, each acquired data has been saved in a corresponding "*shared variable*". These variables type are useful to share variables between VIs running on different devices. All these "*shared variables*" have been inserted into a *case structure*, which is controlled by the state of "*write*" button. When the user push this button, the *true* case is active and data can be transferred for a period decided by the user at each second.

3.4.4 Set point writer VI

A VI has been implemented in order to write on a TDMS file all the measurements useful to the characterization of the testing machine (flow rate, downstream and upstream pressure, temperature, torque and rotational speed).

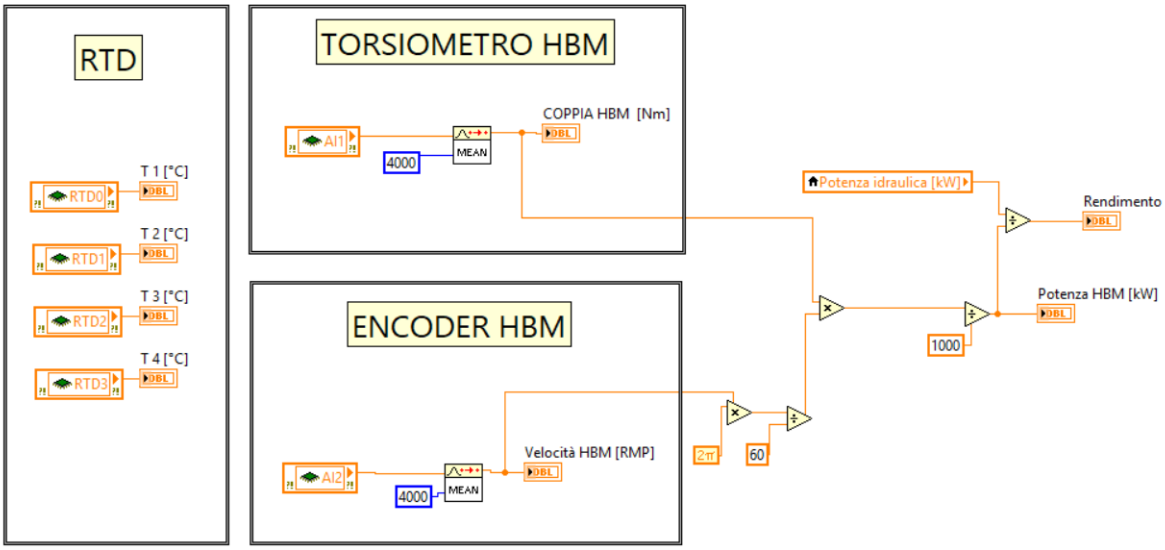

FIGURE 3.36: Block Diagram particular: Torque meter, encoder and RTD.

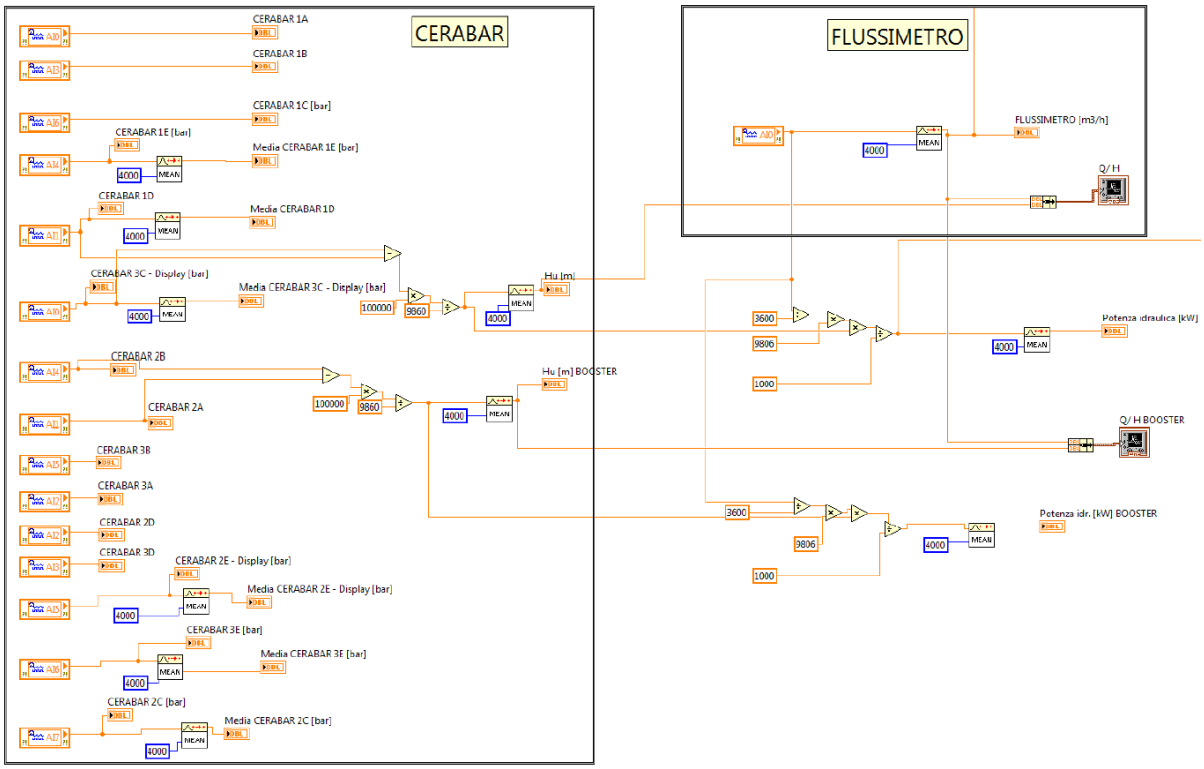

FIGURE 3.37: Block Diagram particular: Cerabar.

Front Panel

The Front Panel of the Set point writer VI (Fig. 3.38) is simply constituted by:

- "*Write*" button: the user decides when start to write data;
- "*Stop*" button: the user decides when stop the VI;
- Control "*N. of samples*": the user decides how many samples can be acquired per second (in our case 30);
- Indicator "*# Set point*": the user can read the set point number that is going to be acquired.

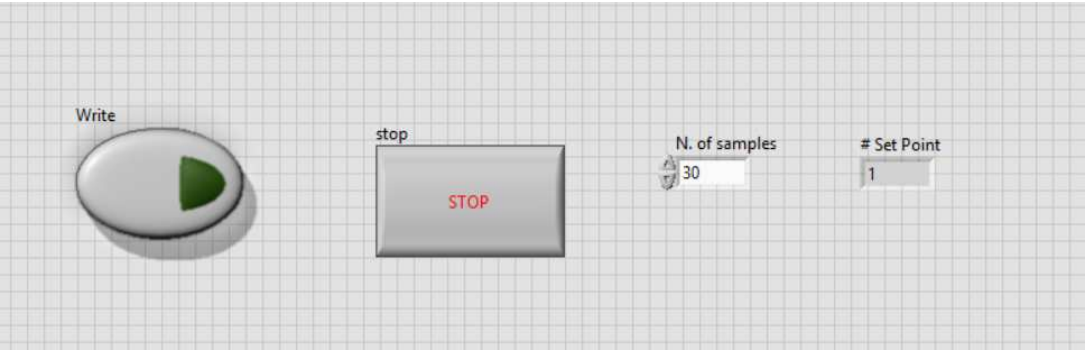

FIGURE 3.38: Front Panel of the Set point writer VI.

Block Diagram

The Block Diagram is characterized by different steps: firs of all, a TDMS file is created by specifying the path file and the "*create or replace*" operation in order to create the file as soon as the VI is lunched. Then, a main while loop has been created in order to execute continuously the code until the "*Stop*" button is pushed. A "*Flat Sequence*" has been added inside the while loop in order to run the code step by step according the following criterion:

- Creating an array of 30 elements for each global variable acquired from the main VI;
- Computing average and deviation standard for each array of acquired data;
- Writing mean, deviation standard and all the acquired data in a TDMS file.

Fig. 3.39 shows in detail how the first part of the VI works. After the creation of the file, a case structure was inserted inside the main while loop. When the user pushes the "*Write*" button, the true case is activated and all the code can be executed. Indeed, the first sequence is to create an array of 30 elements for each global variable by means of a inner "*for loop*". This "*for loop*" is temporized with the "*wait until*" function, set to 1 *s*. The building of arrays is presses when the number of samples is equal to the "*for loop*" index, that starting from 0 is upgraded each second. Then, the second flat sequence can start by computing the average and deviation standard for each array. In the last flat sequence, all the array are concatenated in order to create three matrices: data, mean and standard deviation. These matrices can be written on different sheets of a single data file by mean of the "*write to TDMS*" function Fig. 3.40.

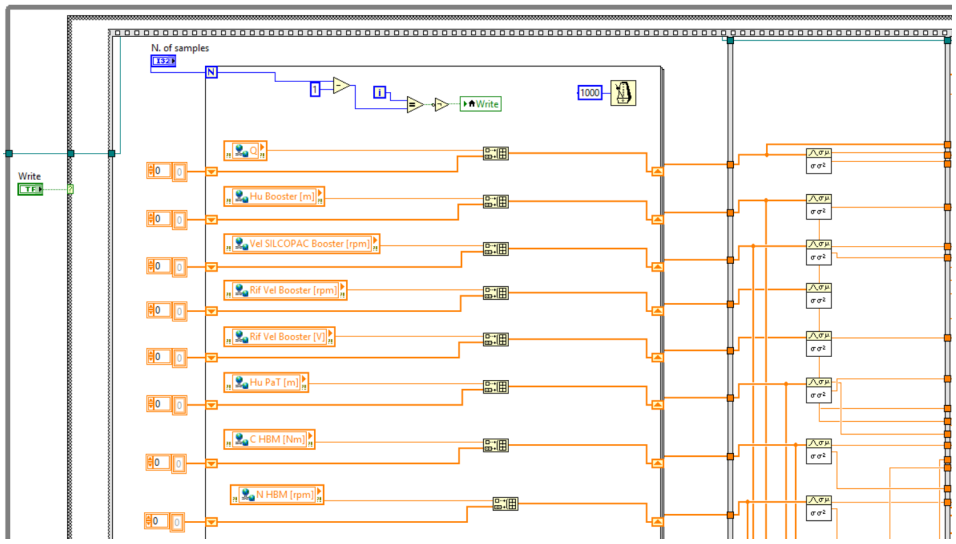

FIGURE 3.39: Particular of the Block Panel of the Set Point Writer VI.

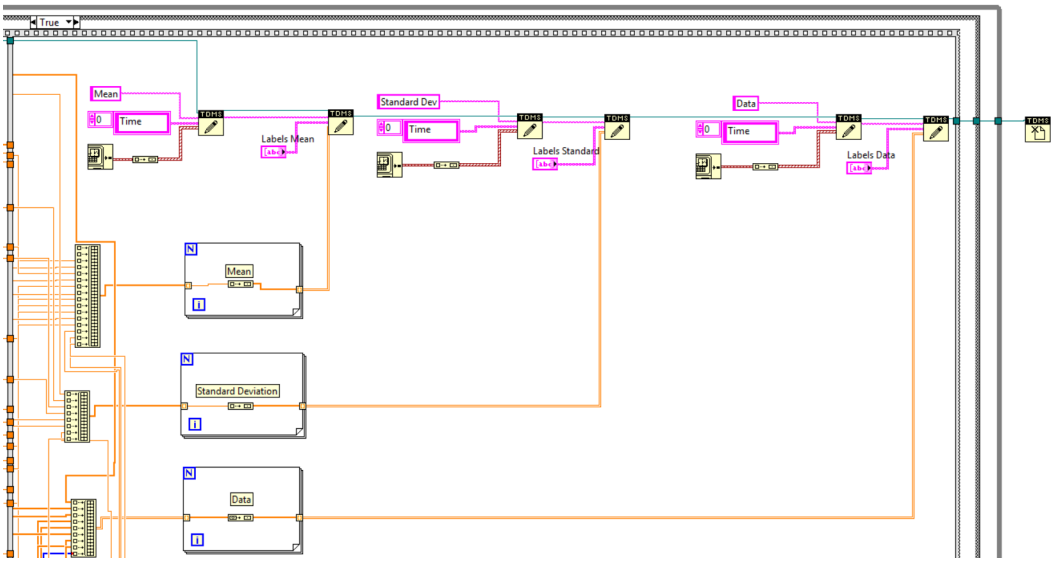

FIGURE 3.40: Particular of the Block Panel of the Set Point Writer VI.

3.4.5 High Frequency Data Acquisition

A software has been created to acquire and write signals from the pressure transducers PCB-113B21, already installed on the system and connected to the National Instrument NI PXIe-4499. The acquisition software has been implemented separately from the system control and management VI (described in the previous section) and after several tests it has been integrated within the latter to allow the operator to use only one graphical interface.

The PCB-113B21 pressure transducer is a sensor for dynamic measurements, which must be connected to a DAQ (Data Acquisition) device because its voltage modulated signal can be read and conditioned. DAQ devices differ from CompactRIO devices because the former are almost exclusively to the acquisition, whereas the latter are focused on real time monitoring and control.

The difference becomes even more marked in the programming phase. Indeed, CompactRIO modules are programmed with a loop function called "*Scan Mode*", where a component of LabVIEW Real-Time, called "*NI Scan Engine*", updates the values of the I/O variables at the frequency specified by the user, up to a maximum of 1 kHz. This frequency seems to be quite limited for dynamic sensors. This frequency limit is related to the maximum clock frequency of the operating system, so it is independent of the type of CompactRIO modules used, unless a different type of programming called FPGA (Field Programmable Gate Array) is used.

In this case, the DAQ NI 4499 communicates with the LabVIEW software by means of the "*NI-DAQmx*" driver. NI-DAQmx shows several advantages including the "*DAQ Assistant*" for channels configuration and measurement tasks for each device.

Analysis and choice of the software architecture

In a first phase, the software architecture has been evaluated in order to exploit the available hardware and software in terms of performance and to avoid delays in the acquisition or writing phase. The two options analyzed were:

1. Creation of a single VI that deals with both acquisition and writing data, to be performed on the PXIe in the field or on the PC in the Control Room;
2. Creation of two separate VIs, one for the acquisition part to be executed on the PXIe and one for the writing part to be executed on the PC in the Control Room.

The first approach highlighted two problems:

- The first problem is that the DAQ modules connected to the PXIe are not recognized on the PC in the Control Room if the VI is executed on the PC;
- The second is that if the VI is executed on the PXIe instead, we do not have the possibility to open, read and modify the TDMS file, on which the acquisitions are written; this is because the file is written and saved on the PXIe hard disk, not reachable from the control room PC.

Therefore, the second option has been decided, i.e. the creation of two separate VIs, one dealing with the data acquisition (running on the PXIe) and one dealing with the acquired data log (running on the PC in the control room). This represents a distributed solution also to unload the PXIe from the writing task that is instead

performed by the PC in the Control Room, which receives the acquired data and proceeds to write them in a file with a TDMS extension.

In this section it is analyzed in detail the structure and operation of the Acquisition VI and how the acquired data are transferred to the Writing VI. It deals with the setting of the acquisition channels connected to the pressure transducers and the sending of the acquired data to the Writer VI, if the writing condition is true.

Acquisition VI: Front Panel

The Front Panel (Fig. 3.41) is subdivided in the following sections:

- Indicator "*Graph*": it shows the values in V acquired by the PCB pressure transducers;
- Control "*Number of Samples in the Graph*": it defines the number of samples that are displayed simultaneously in the graph;
- Button "*Write*": it manages the data writing;
- Control "*Acquisition Time*": the user can set how long to write the data;
- Indicator "*Elapsed Time*": it shows the time that has elapsed since the write button has been pressed, and it automatically locks when the time set in "*Acquisition Time*" expires;
- Button "*Stop*": it stops the acquisition.

Therefore, after setting the acquisition frequency and writing time, the user can start the VI and press the "*Write*" button to start writing data.

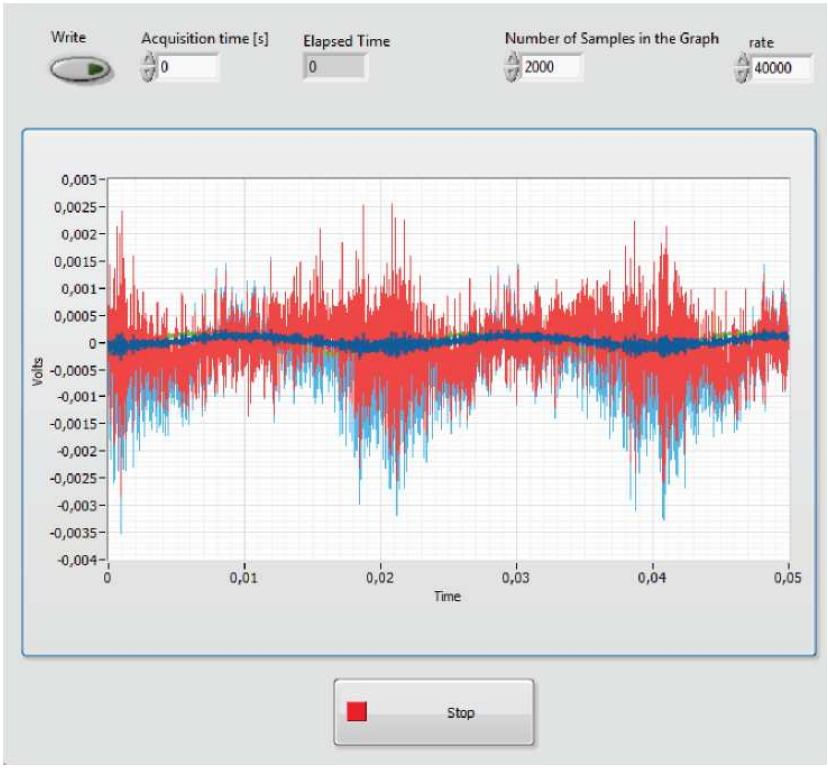

FIGURE 3.41: Acquisition VI: Front Panel.

Acquisition VI: Block Diagram

Fig. 3.42 shows the block diagram of the Acquisition VI, which has been subdivided into two main while loops: the first acquires, visualizes and adds data to a queue, which is decomposed by the second while loops that sends the acquired data to the Writing VI by means of a "*Network Endpoint*" function.

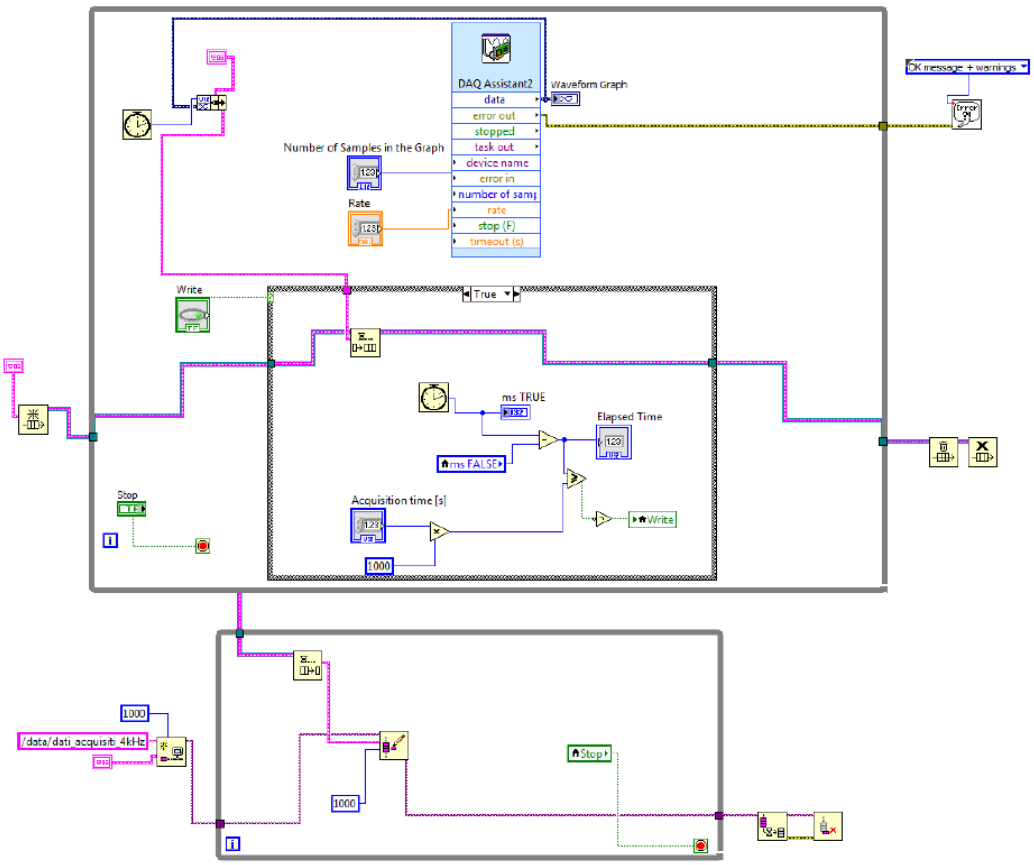

FIGURE 3.42: Acquisition VI: Block Diagram.

Data are acquired using the "*DAQ Assistant*" tool, which has been configured by selecting the acquisition module and its 5 Analog channels (ch0 - ch4). This information will be stored in a so-called "*task*", i.e. a collection of one or more virtual channels with all its properties.

After creating the task, it has been possible to configure specific settings for each channel such as:

- "*Signal Input range*";
- "*Custom Scaling*";
- "*Terminal Configuration*";
- "*Time Settings*"

"*Signal Input range*" allows us to specify the signal range. In our case, it has been set $\pm 10\ V$; It is possible to scale the input data through "*Custom Scaling*" for a change of unit of measurement or to correct a possible systematic error (offset or BIAS). "*Terminal Configuration*" instead allows us to indicate the type of analog input (differential or pseudodifferential type). In our case the pseudodifferential type of connection

has been selected. Through the "*Timing Settings*" section of the DAQ Assistant it is also possible to set and then subsequently modify the type of acquisition, the acquisition frequency and the number of samples per cycle. The selected "*acquisition mode*" was a continuous sampling. The acquisition frequency can be selected by the user using a "*Rate*" checkbox.

Once the DAQ Assistant is configured, it is ready in the block diagram. The tool is positioned within a while loop because the continuous acquisition mode has been chosen. Therefore at each execution of the cycle the DAQ Assistant returns a set of N values equal to the number specified in "*Number of Samples in the Graph*", acquired at the "*Rate* " frequency, as "*Dynamic Data*" type.

The "*Dynamic Data*" type stores the information generated or acquired by an Express VI and appears as a dark blue terminal. Most of the Express VIs accept and / or return a type of "*Dynamic Data*". The acquired "*Dynamic Data*" are plotted on the "*Waveform Graph*". Most of the other VI and functions in LabVIEW do not accept the "*Dynamic Data*" type. For this reason, in order to use them in other functions, these data have been converted by means of "*Convert from Dynamic Data*" Express VI.

A queue is created using the "*Obtain Queue*" function and initialized with the data type "*Dynamic Data*". This operation is performed outside the while loop so that it is executed only once, at the VI start. If the "*Write*" button is pressed (i.e. the condition of the Boolean "*Case Structure*" becomes true), the data sets exiting the "*DAQ Assistant*",("*Dynamic Data*" type), are added to the queue through the "*Enqueue Element*" function. This allows the VI to send data to the writing VI.

Moreover, when the "*Write*" button is pressed and assumes a Boolean value True, the "*true Case Structure*" is executed by starting a timer in milliseconds to check when the "*Elapsed Time*" value, i.e. the time elapsed since the button is pressed, becomes greater than or equal to the "*Acquisition time*", which can be set by the user from the front panel. In this case the button is returned to False condition, by a "*logic not*" and acquired data stop to be added to the queue, as provided by the "*false Case Structure*".

In the second while loop, which runs in parallel to the first, a "*Network Endpoint Writer*" was created using the "*Create Network Stream Writer Endpoint*" function. It acts as a communication node between the acquisition VI and the writer VI. The Writer Endpoint was set with the name "*/ data / data_acquis_4kHz*", the buffer size and the data type to be written, fitting to that of the queue or "*Dynamic Data*". In this second while loop (next to the "*Network Endpoint Writer*"), the elements are extracted from the queue with the "*Dequeue Element*" function and written individually to the buffer using the "*Write Single Element To Stream*" function. If the VI stops, the data flow between the acquisition VI and the writer VI is destroyed by the "*Destroy Stream Endpoints*" function.

Writer VI: Front Panel

The Front Panel (Fig. 3.43) is subdivided in the following sections:

- Control "*Target IP Address*": the user enters the IP address of the PXIe, from which to read the data;
- Indicator "*Concatenated string*": after starting the VI a string is concatenated representing the complete address of the endpoint to read from ;
- Indicator "*Available Elements to Read*": indicates the number of items waiting to be read;

- Control "*Read speed*": the user can select with a drop-down menu the speed with which read the received data;
- Indicator "*Acquired data*": shows the data coming from the VI Acquisition through a graph and is useful to verify that the data flow arrives correctly;
- Indicator "*Error I/O*": this is a debug window where errors are indicated, identified by a code that is reported;
- Button "*Stop*": it stops the VI.

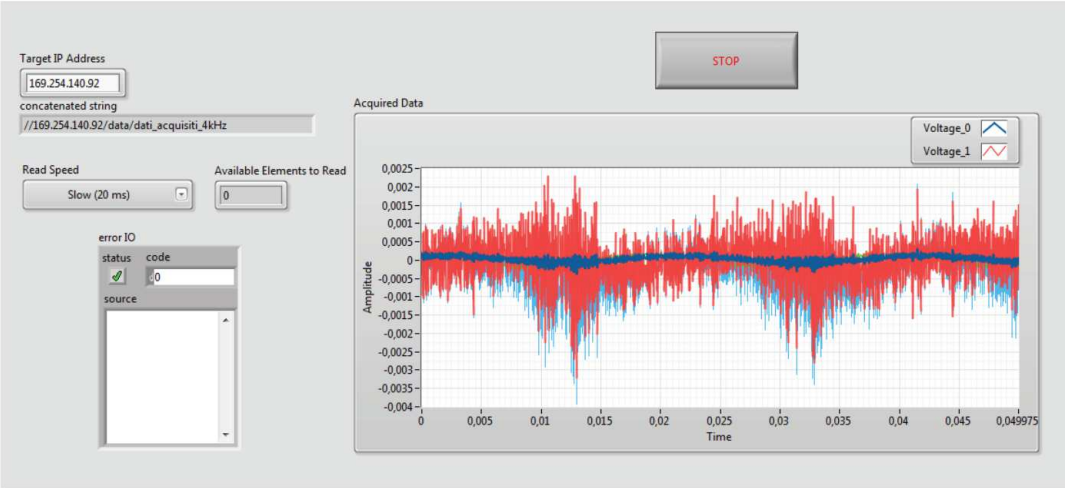

FIGURE 3.43: Writer VI: Front Panel.

Writer VI: Block Diagram

The Block Diagram (Fig. 3.44) is divided into two parts. In the upper part it deals with the communication with the Acquisition VI to receive the data flow, visualize and add them to a queue, while in the lower part it decomposes the data inside the queue and writes them in a file with the TDMS extension.

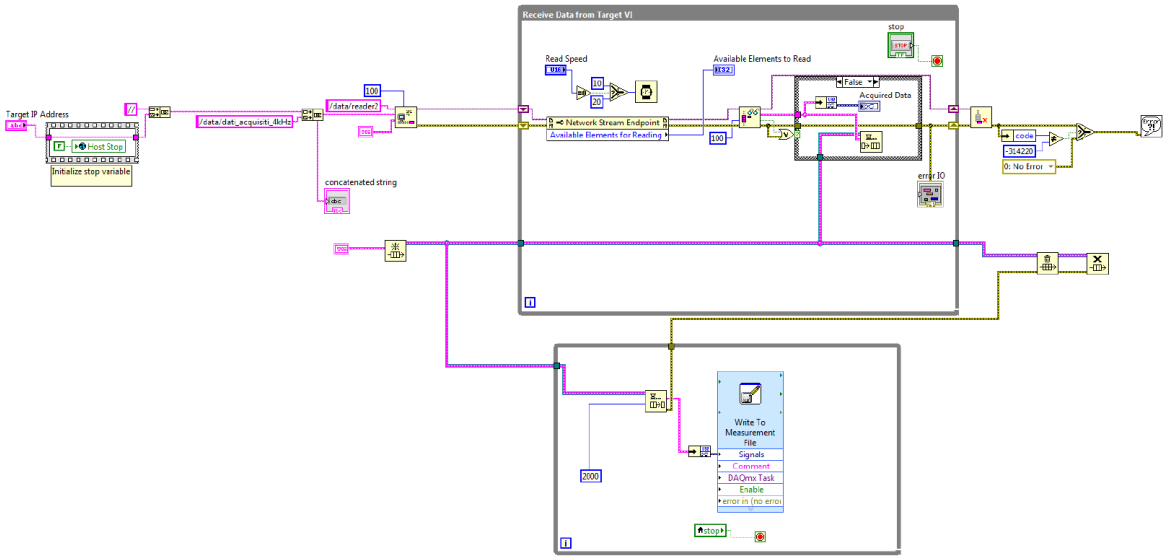

FIGURE 3.44: Writer VI: Block Diagram.

In order to create a connection with the Acquisition VI, an "*Endpoint Reader*" has been created using the "*Create Network Stream Reader Endpoint*" function. It represents a network node that reads the data sent by the "*Endpoint Writer*" of the Acquisition VI, named "*/ data / data_acquis_4kHz*".

Then, the reader has been initialized with the name "*/ data / reader2*", the size of the reader buffer, the type of data to be read which is always *Dynamic Data* and the string containing the complete address from which to receive the data. The latter is obtained by concatenating through the "*Concatenate String function*" the PXIe IP address (from which we receive the data) with the name of the "*Endpoint Writer*" that writes the data in the Acquisition VI (Fig. 3.45).

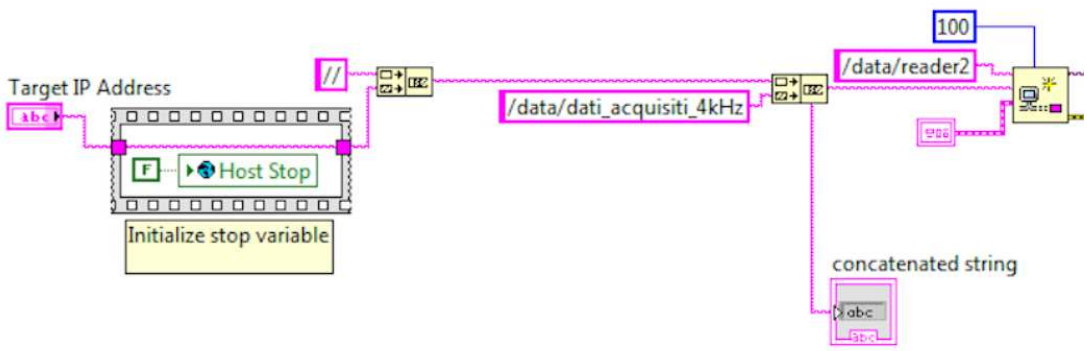

FIGURE 3.45: Creation and initialization of the Endpoint Reader.

Subsequently, within a while loop, the "*Read Single Element From Stream*" function reads individually the elements available inside the buffer at a speed equal to the timing of the while loop, called "*Read Speed*". The "*Select Function*" allows the user to select a reading period of 10 or 20 milliseconds, i.e. a frequency of 100 *Hz* or 50 *Hz* respectively. The number of available elements within the reader buffer is obtained through the "*Available Elements for Reading*" property of the "*Network Stream Endpoint*" and shown via an indicator on the Front Panel (Fig. 3.46).

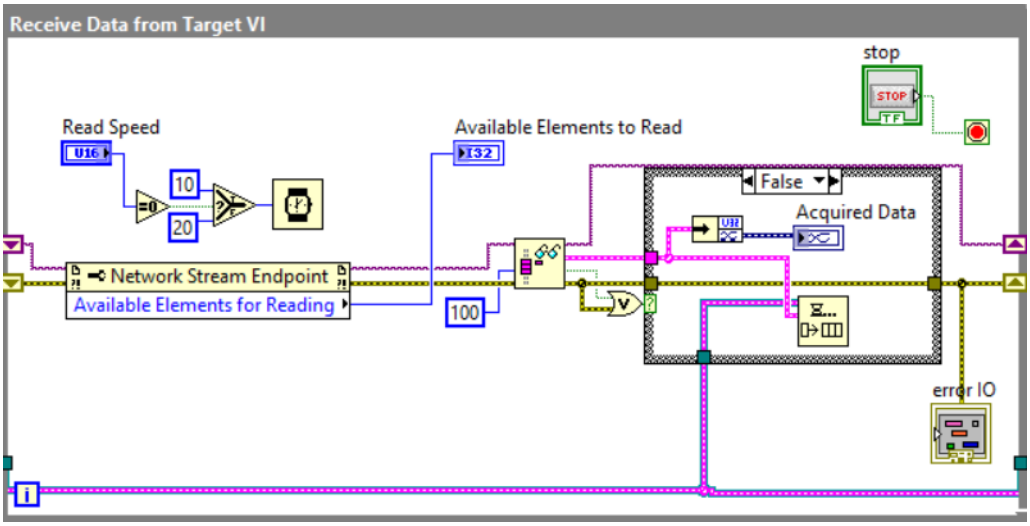

FIGURE 3.46: Data Reading and visualization from the reading buffer.

Outside the while loop a queue is created using the "*Obtain Queue*" function, which is initialized with the same type of data as the reader, i.e. *Dynamic Data*. Each read element is added to the queue with the "*Enqueue Element*" function. Then, elements in the queue converge in a second while loop where they are again extracted from the queue with the "*Dequeue Element*" function (Fig. 3.47).

The single element is then written via "*Write To Measurement File*", an Express VI that writes data into a spreadsheet in TDMS extension. This Express VI can open the file, write it and close it. The "*Write To Measurement File*" Express VI was set up by specifying various options:

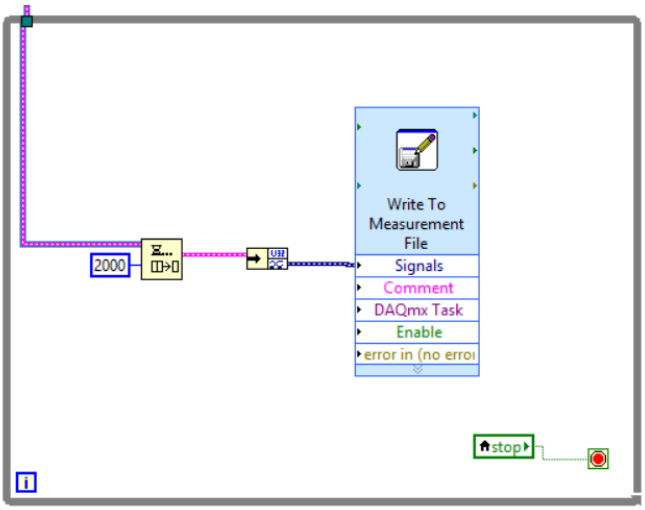

FIGURE 3.47: TDMS data file creation.

- *File name*: it requires the Path file;
- *Action*: it allows the user to decide how to save and what to do when the file already exists;
- *File Format*: allows you the user to select the file format (in our case .TDMS);
- *Segment Headers*: the user can select how to manage the tabs within the file calculation, whether to use a single sheet or generate a new sheet for each iteration;
- *Time Columns*: select whether to create a time column for each channel or a single column (Fig. 3.48).

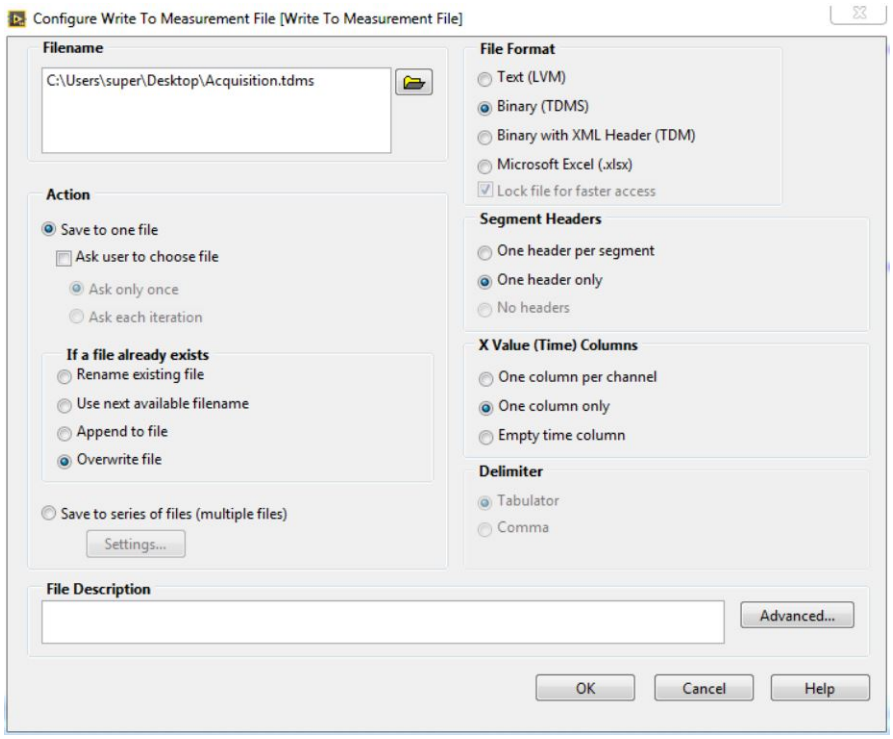

FIGURE 3.48: Configuration of the Express VI Write To Measurement File.

Finally, the data flow between the writer and the reader is destroyed by the "*Destroy Stream Endpoints*" function. The "*Flush Stream*" function ensures that all data sent by the writer has been received by the reader, which in the Acquisition VI is called the before the writer is destroyed. It is possible to select among two "*wait conditions*":

- *All Elements Read from Stream*;
- *All Elements Available for Reading*.

By specifying "*All Elements Read from Stream*" the "*Flush Stream*" function will wait until all data are transferred to the reader and all have been read (Fig. 3.49). By specifying the "*All Elements Available for Reading*" option, the function will wait until all data is transferred to the reader, but not read. Not using "*Flush Stream*", or destroying the "*Endpoint Reader*" before the "*Endpoint Writer*", all data still in transit or all

data still in the write buffer may be lost (Fig. 3.50). When the "*Endpoint Writer*" is destroyed before the "*Endpoint Reader*", subsequent reader calls will be handled until the buffer is empty. At that point, a subsequent reading call generates an error with code 314220, which informs us that the writer on the other side no longer exists (Fig. 3.51).

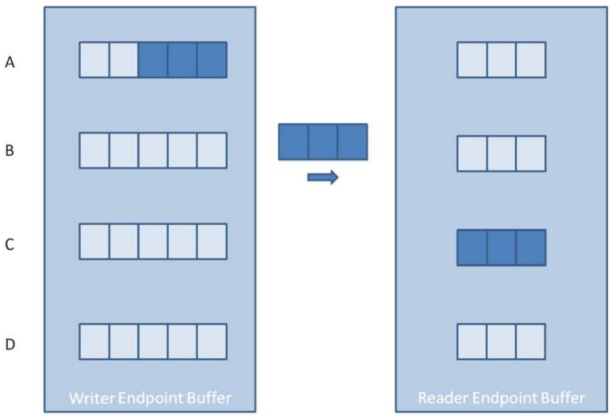

FIGURE 3.49: Data transfer steps and buffer statesData transfer steps and buffer states.

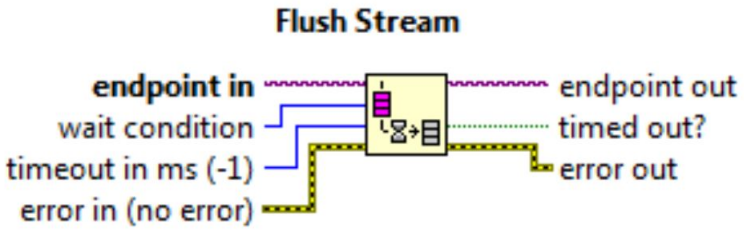

FIGURE 3.50: Flush Stream Node.

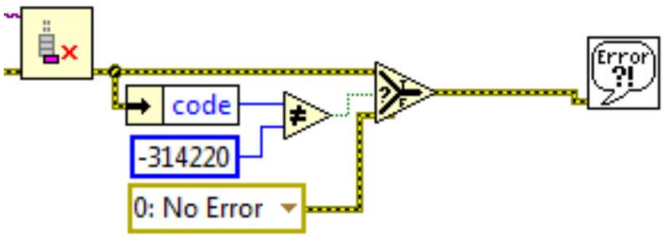

FIGURE 3.51: 314220 error management.

Data file .TDMS

In order to verify the correct operation of the VI, a data acquisition and writing test has been performed for 5 seconds at a sampling rate of 4 kHz. The result was that the TDMS file, containing the acquired data, has been correctly created. Fig. 3.52 shows the file summary page showing information such as the total number of samples, the sampling period, the data type and the unit of measure. Fig. 3.53 shows

the second page in which the various acquisitions are saved. By examining the data and the sampling period of the same, it is possible to confirm that the sampling frequency has been respected and the number of samples obtained coincides with that expected. The software is therefore ready for future acquisitions for the experimental characterization of the PaT.

	A	B	C	D	E	F	G	H
1	**Root Name**	**Title**	**Author**	**Date/Time**	**Groups**	**Description**		
2	acquisizioneTrasduttori.tdms		super		1			
3								
4	**Group**	**Channels**	**Description**	*wf_xcolumns*				
5	Untitled	6		One				
6								
7	**Untitled**							
8	**Channel**	**Datatype**	**Unit**	**Length**	**Minimum**	**Maximum**	**Description**	*NI_ChannelName*
9	**Time**	DT_DATE	s	20000				
10	**Trasduttore 4A**	DT_DOUBLE	Volts	20000				Trasduttore 4A
11	**Trasduttore 4B**	DT_DOUBLE	Volts	20000				Trasduttore 4B
12	**Trasduttore 4C**	DT_DOUBLE	Volts	20000				Trasduttore 4C
13	**Trasduttore 4D**	DT_DOUBLE	Volts	20000				Trasduttore 4D
14	**Trasduttore 4E**	DT_DOUBLE	Volts	20000				Trasduttore 4E
15	**Implicit**	**Start**	**Interval**	**Length**				
16	Time	0	0,00025	20000				

FIGURE 3.52: Summary work sheet of the TDMS file.

	A	B	C	D	E	F	G
1	**Time**	**Time***	**Trasduttore 4A**	**Trasduttore 4B**	**Trasduttore 4C**	**Trasduttore 4D**	**Trasduttore 4E**
2	10/04/2018 07:35:34,865 AM	0	0,0002262	9,87053E-05	0,000205636	5,48363E-06	0,000156283
3	10/04/2018 07:35:34,865 AM	0,00025	0,000219345	8,7738E-05	0,000228941	4,11272E-06	3,70145E-05
4	10/04/2018 07:35:34,866 AM	0,0005	0,00019604	0,000100076	0,000205636	-2,74181E-06	7,67708E-05
5	10/04/2018 07:35:34,866 AM	0,00075	0,000193298	7,4029E-05	0,000202894	-3,016E-05	0,000104189
6	10/04/2018 07:35:34,866 AM	0,001	0,000190556	9,32217E-05	0,00021112	-7,95126E-05	0,000123382
7	10/04/2018 07:35:34,866 AM	0,00125	0,000190556	0,000108302	0,000212491	-9,59635E-05	5,20945E-05
8	10/04/2018 07:35:34,867 AM	0,0015	0,000178218	9,04799E-05	0,000198781	-0,000122011	0,000112414
9	10/04/2018 07:35:34,867 AM	0,00175	0,000207007	9,32217E-05	0,000200152	-0,000134349	0,000193298
10	10/04/2018 07:35:34,867 AM	0,002	0,000157654	9,59635E-05	0,000198781	-0,000141203	0,000207007
11	10/04/2018 07:35:34,867 AM	0,00225	0,000168622	9,73344E-05	0,000201523	-0,000174105	0,000100076
12	10/04/2018 07:35:34,868 AM	0,0025	0,000172734	7,95126E-05	0,000198781	-0,000193298	0,000132978
13	10/04/2018 07:35:34,868 AM	0,00275	0,00016588	8,22544E-05	0,000190556	-0,00019604	0,00025773
14	10/04/2018 07:35:34,868 AM	0,003	0,000172734	9,18508E-05	0,000187814	-0,000213861	0,00031805
15	10/04/2018 07:35:34,868 AM	0,00325	0,000142574	8,7738E-05	0,000179589	-0,000263214	0,000276923
16	10/04/2018 07:35:34,869 AM	0,0035	0,000153542	8,22544E-05	0,000189185	-0,000275552	0,000235796
17	10/04/2018 07:35:34,869 AM	0,00375	0,000139832	5,07236E-05	0,000191927	-0,00031805	0,000261843
18	10/04/2018 07:35:34,869 AM	0,004	0,00013572	8,7738E-05	0,000164509	-0,000308454	0,000339985
19	10/04/2018 07:35:34,869 AM	0,00425	0,000119269	6,99162E-05	0,000186443	-0,000355065	0,000281036
20	10/04/2018 07:35:34,870 AM	0,0045	0,000111043	6,99162E-05	0,000176847	-0,000371516	0,000250876
21	10/04/2018 07:35:34,870 AM	0,00475	0,000126123	6,71744E-05	0,000167251	-0,000364661	0,000324905
22	10/04/2018 07:35:34,870 AM	0,005	0,000100076	6,16908E-05	0,000176847	-0,00040853	0,000327647
23	10/04/2018 07:35:34,870 AM	0,00525	8,08835E-05	5,07236E-05	0,000193298	-0,000431836	0,000148058
24	10/04/2018 07:35:34,871 AM	0,0055	0,000100076	3,29018E-05	0,00021112	-0,000457883	0,0001508
25	10/04/2018 07:35:34,871 AM	0,00575	9,04799E-05	4,66108E-05	0,000202894	-0,00046885	0,000187814
26	10/04/2018 07:35:34,871 AM	0,006	9,73344E-05	3,29018E-05	0,000201523	-0,000470221	0,000132978
27	10/04/2018 07:35:34,871 AM	0,00625	6,85453E-05	3,56436E-05	0,000198781	-0,000512719	5,75781E-05
28	10/04/2018 07:35:34,872 AM	0,0065	5,75781E-05	2,8789E-05	0,000202894	-0,000525057	4,24981E-05
29	10/04/2018 07:35:34,872 AM	0,00675	7,26581E-05	1,508E-05	0,000212491	-0,000527799	3,97563E-05
30	10/04/2018 07:35:34,872 AM	0,007	6,71744E-05	2,19345E-05	0,000191927	-0,000525057	2,8789E-05

FIGURE 3.53: Some of acquired samples saved in the .TDMS file.

Chapter 4

Experimental Results

A KSB Etanorm 200-150-400 PaT was tested in the test rig in order to use its experimental curves for the achievement of some objectives of this work that will be debated in next chapters, such as the development of PaT performance prediction models and the assessment of a PaT installation in a real case study. The experimental characterization was carried out for a wide range of flow rates. During pump test, the four-quadrant AC/DC converter automatically maintains constant the rotational speed ($0 \div 2400\ rpm$) independently of the flow rate Q. During turbine operation mode, the rotational speed is kept constant by varying the electric motor torque, through the same four-quadrant AC/DC converter, at the different booster operation points. Data were collected at 1 s interval for a duration of 30 s, after having reached steady state conditions. In order to prove the repeatability of the measurements, three tests were carried out in different months. Furthermore, test acceptance criterion was applied to pump curves, according to UNI EN ISO 9906:2012.

4.1 Test Arrangements

In order to compute the characteristic curves of the machine, it is essential to know all the dimensions of the piping elements that constitute the test arrangements. Fig. 4.1 shows the real scheme of the testing zone. Pressure downstream the testing machine is measured in section A, positioned at a length of $L_1 = 1.3\ m$ from the pump suction flange (section 1). The discharge piping is constituted by a gradual enlargement because the nominal diameter of the pump discharge flange is equal to 6″, whereas the piping has a nominal diameter of 8″. After the gradual enlargement, there is a straight pipe 0.45 m long (L_2) and an elbow bend. Pressure upstream the machine is measured in section B, positioned at a length of $L_3 = 1.2\ m$ from the elbow flange. The distance between the axes of both horizontal pipes is equal to $\Delta z = z_B - z_A = 1.5\ m$.

As stated by equation 4.1, the total head of a pump, H_u, can be computed by summing up the total head difference between the two pressure measuring sections, H_B^0 and H_A^0, and the total hydraulic loss in the piping Z_h.

$$H_u = H_B^0 - H_A^0 + Z_h = \frac{p_B - p_A}{\rho\, g} + (z_B - z_A) + \frac{c_B^2 - c_A^2}{2g} + (Z_f + Z_L) \tag{4.1}$$

For a turbine, the total head is instead calculated by equation 4.2, where the total hydraulic loss, Z_h, is subtracted from the total head difference between the two pressure measuring section, H_B^0 and H_A^0.

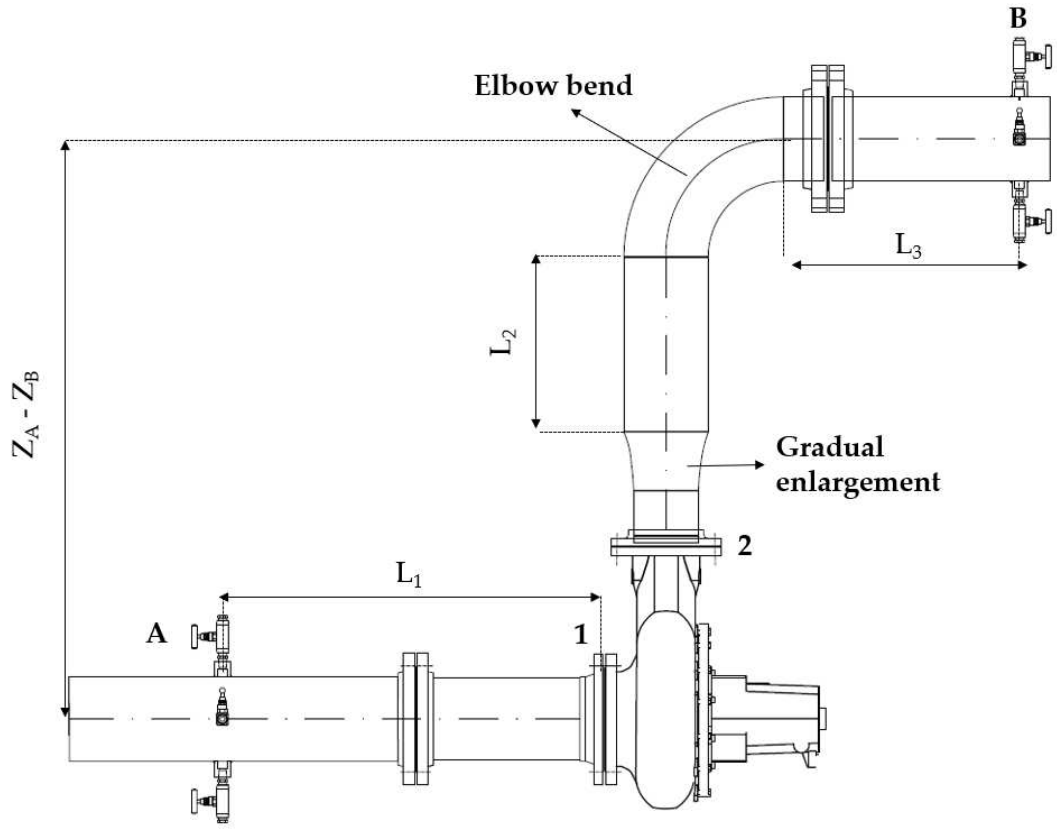

FIGURE 4.1: Test arrangements sketch.

$$H_t = H_B^0 - H_A^0 - Z_h = \frac{p_B - p_A}{\rho\, g} + (z_B - z_A) + \frac{c_B^2 - c_A^2}{2g} - (Z_f + Z_L) \tag{4.2}$$

The total hydraulic loss, Z_h, is obtained by summing up friction, Z_f, and local losses, Z_L. The former can be computed for each pipe by means of Darcy-Weisbach equation 4.3, where L, D and c, are respectively the pipe length, the pipe diameter and the mean fluid velocity. Moreover, f is the friction coefficient that can be evaluated by the Colebrook equation (equation 4.4). The local losses can be instead computed by using equation 4.5, where ζ is the local loss coefficient that depends on element by element of the piping.

$$Z_f = f\,\frac{L}{D}\,\frac{c^2}{2g} \tag{4.3}$$

$$\frac{1}{\sqrt{f}} = -2\log\left(\frac{2.51}{Re\,\sqrt{f}} + \frac{\epsilon/D}{3.71}\right) \tag{4.4}$$

$$Z_L = \zeta\,\frac{c^2}{2g} \tag{4.5}$$

4.2 Experimental Tests in Pump Operation Mode

During pump test, the user can remotely set the desired rotational speed, whose value is transferred to the four-quadrant AC/DC converter that automatically maintains constant the rotational speed ($0 \div 2400\ rpm$) independently of the flow rate Q. Once the desired rotational speed is reached, user can start to regulate the flow rate by changing the set point of the control valve. In this way, it is possible to characterize the machine for different flow rates at different rotational speeds. Once steady state conditions are reached, user can acquire all the data useful for the machine characterization:

- Pressure downstream the pump (p_A);
- Pressure upstream the pump (p_B);
- Flow rate (Q);
- Rotational speed (N);
- Torque (C)

It was decided to acquire data at 1 s interval for a duration of 30 s. This means that for each parameter, 30 data are collected. A post-processing procedure computes the average and the standard deviation for each sample of 30 collected data. In order to obtain the real characteristic curve, it is essential to evaluate the hydraulic losses in the piping. Friction losses were calculated by considering a total piping length $L = L_1 + L_2 + L_3 = 2.95\ m$ and $D = 0.2101\ m$, whereas the friction coefficient contemplates a roughness for steel pipes $\epsilon = 0.05\ mm$. Two local losses were considered because of the presence of the gradual enlargement and the elbow bend. Tab. 4.1 shows different local loss coefficients for gradual enlargement at different diameter ratios and cone angles. In our case, $\zeta = 0.2$ considering $D/d = 1.3$ and $\theta = 20°$. For the elbow bend, the local loss coefficient was $\zeta = 0.24$ considering the ratio $r/D = 1.5$.

TABLE 4.1: loss coefficients for gradual enlargement at different cross section ratios and cone angle [81].

	Angle of Cone θ				
D/d	**10°**	**15°**	**20°**	**25°**	**30°**
1.1	0.03	0.05	0.10	0.13	0.16
1.2	0.04	0.09	0.16	0.21	0.25
1.4	0.06	0.12	0.23	0.30	0.36
1.6	0.07	0.14	0.26	0.35	0.42
1.8	0.07	0.15	0.28	0.37	0.44
2.0	0.07	0.16	0.30	0.39	0.48

Once the hydraulic loss were computed, it was possible to calculate the pump head, H_u, using equation 4.1, where the kinetic energy difference between section A and B is neglected. Moreover, the mechanical power was obtained by multiplying the torque, c, by the rotational speed, N, whereas the efficiency by dividing the hydraulic power, P_{hydr}, by the mechanical power, P.

$$P = C \left(\frac{2\ \pi\ N}{60} \right) \tag{4.6}$$

$$\eta = \frac{P_{hydr}}{P} = \frac{\rho\, g\, H_u\, Q}{P} \tag{4.7}$$

Fig. 4.2, Fig. 4.3 and Fig. 4.4 show the characteristic curves (H, P and η vs. Q) of the PaT under pump operation mode at different rotational speeds: 800 rpm, 1000 rpm, 1200 rpm and 1520 rpm. The experimental efficiency points are provided with their standard deviation bands, whereas the standard deviation of the experimental head and power, being within ± 3 %, are not depicted.

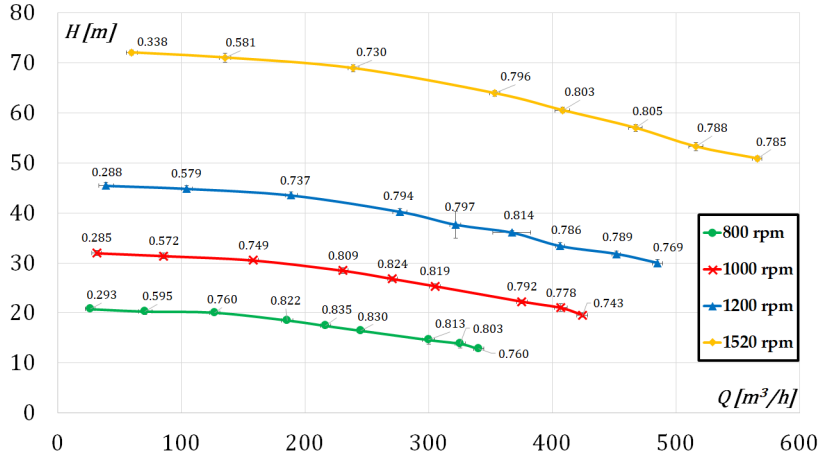

FIGURE 4.2: Experimental head, H, vs. discharge, Q, under pump operation mode at different rotational speeds.

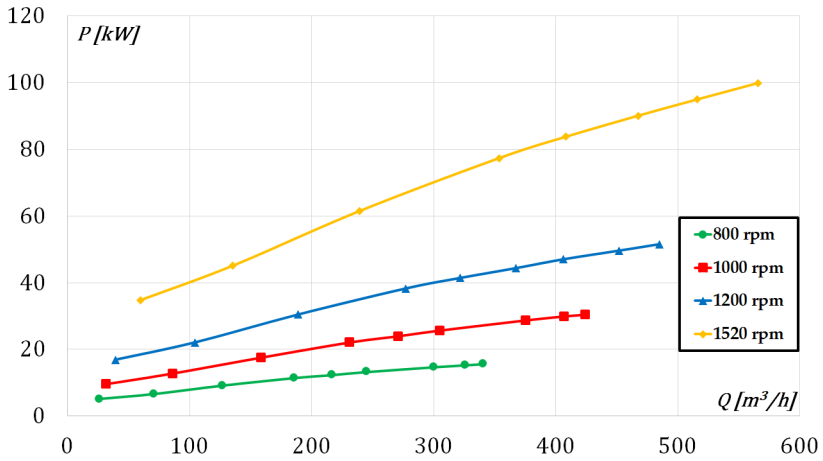

FIGURE 4.3: Experimental power, P, vs. discharge, Q, under pump operation mode at different rotational speeds.

4.2.1 Test repeatibility

Test at 1000 rpm was repeated three times in different months in order to test the repeatibility of measurements. Fig. 4.5, Fig. 4.6 and Fig. 4.7 show respectively the experimental head, power and efficiency at 1000 rpm measured in different months: May 2017, June 2017 and July 2018. Although months or years passed from one test to another, similar performance curves were obtained by showing good repeatibility.

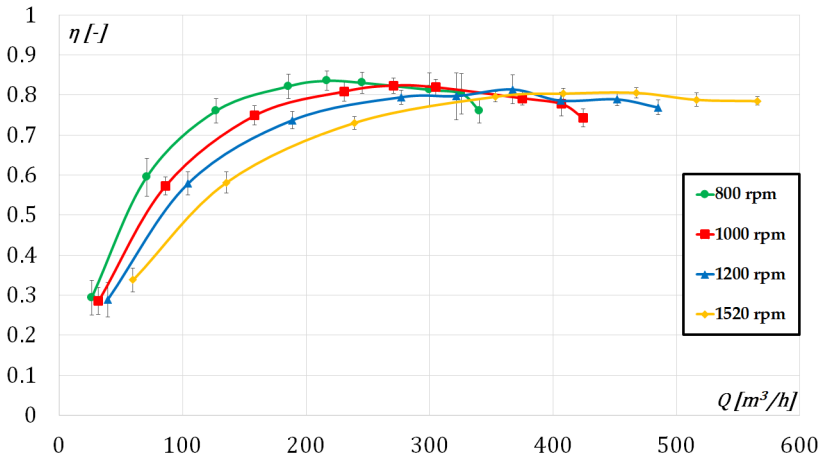

FIGURE 4.4: Experimental efficiency, η, vs. discharge, Q, under pump operation mode at different rotational speeds.

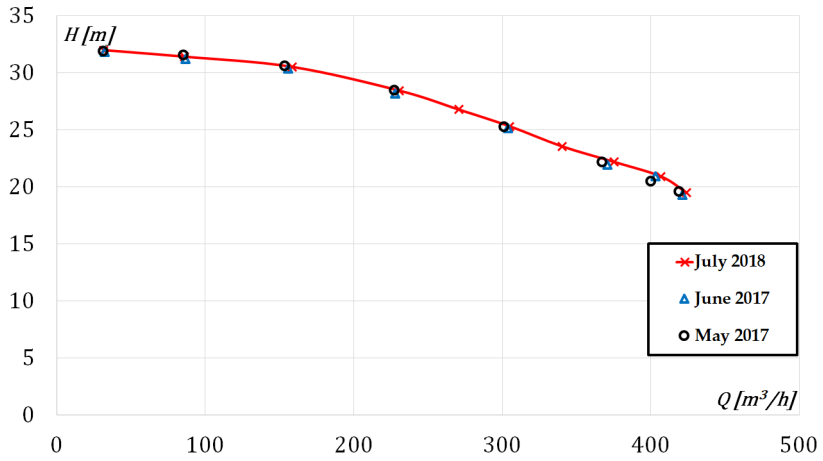

FIGURE 4.5: Comparison of experimental head curves, H, vs. discharge, Q, acquired in different measurements campaigns.

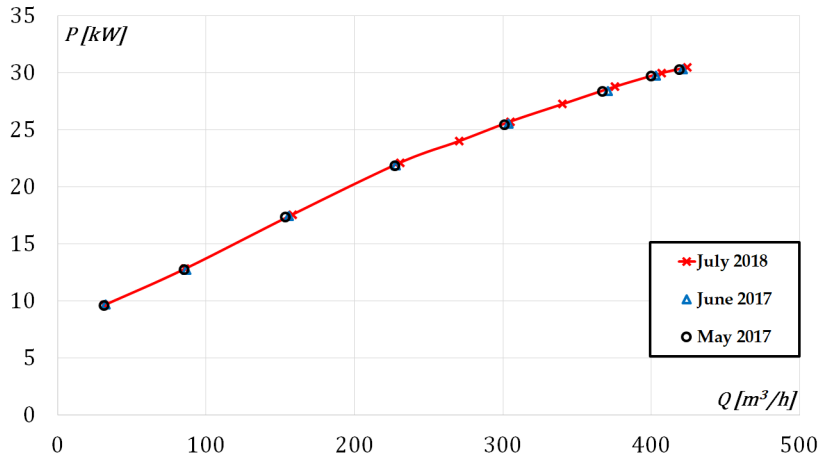

FIGURE 4.6: Comparison of experimental power curves, P, vs. discharge, Q, acquired in different measurements campaigns.

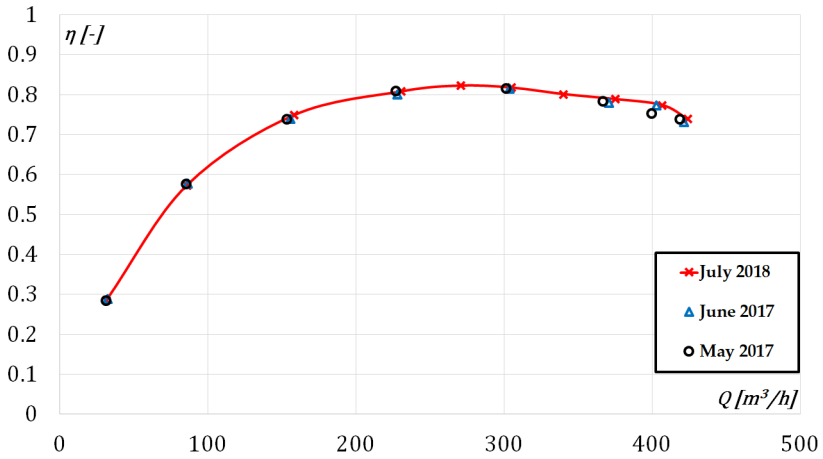

FIGURE 4.7: Comparison of experimental efficiency curves, η, vs. discharge, Q, acquired in different measurements campaigns.

4.2.2 Affinity laws

In order to verify the validity of the measurements at different rotational speeds, the experimental curves at 800 rpm, 1200 rpm and 1520 rpm were also obtained by scaling the curve at 1000 rpm by using affinity laws. Indeed, Fig. 4.8 shows how the scaled points (in black) overlap the experimental ones.

$$Q = Q' \left(\frac{N}{N'} \right) \tag{4.8}$$

$$H = H' \left(\frac{N}{N'} \right)^2 \tag{4.9}$$

$$P = P' \left(\frac{N}{N'} \right)^3 \tag{4.10}$$

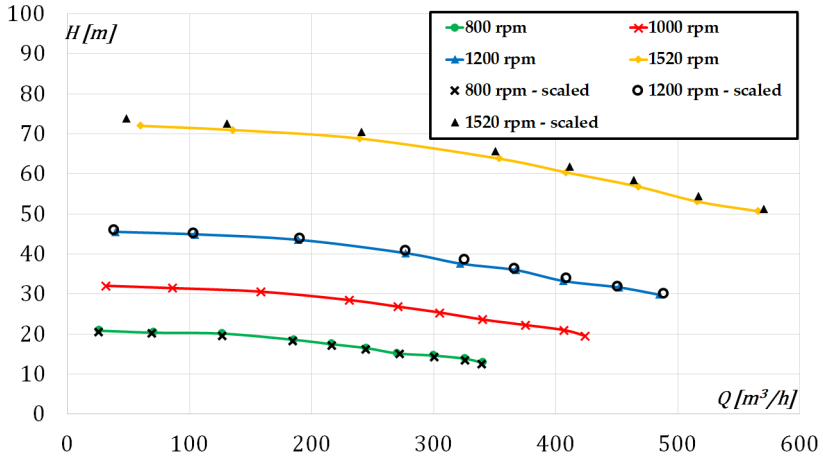

FIGURE 4.8: Comparison between the experimental head curves with the scaled ones under pump mode operation.

4.2.3 Test Acceptance: UNI EN ISO 9906:2012

The machine certificate was provided according to the standard UNI EN ISO 9906 [82]. This standard contemplates six pump performance test acceptance grades (1B, 1E, 1U, 2B, 2U and 3B). Grade 1 is the most stringent grade, with 1U and 2U having a unilateral tolerance and grades 1B, 2B and 3B having a bilateral tolerance. Grade 1E is also bilateral in nature and is important to those concerned with energy efficiency.

The purchaser and the manufacturer may agree to use any grade to judge wheiter or not a specific pump meets a guarantee point. If a guarantee point is given, but no acceptance grade is specified, this standard reverts to a default test acceptance grade (2B for water distribution networks). Moreover, the acceptance grades for flow rate and head are mandatory, whereas those for power and efficiency are optional. Guarantee point acceptance grades for pump head, flow rate, power and efficiency are provided in Tab. 4.2.

TABLE 4.2: Pump test acceptance grades and corresponding tolerance from UNI EN ISO 9906:2012.

Grade	1			2		3	
Acceptance grade	**1U**	**1E**	**1B**	**2B**	**2U**	**3B**	Guarantee requirement
Q	$+10$ %	± 5 %		± 8 %	± 16 %	± 9 %	Mandatory
H	$+6$ %	± 3 %		± 5 %	± 10 %	± 7 %	Mandatory
P	$+10$ %	$+4$ %		$+8$ %	$+16$ %	$+9$ %	Optional
η	≥ 0 %		-3 %	-5 %		-7 %	Optional

Our tested machine was provided with its certificate with acceptance grade 3B. This means that the guaranteed point is provided with its tolerances (Q: $\pm 9\%$, H: $\pm 7\%$, P: $+9\%$, η: -7%). According to the standard, guarantee point evaluation shall be performed at the rated speed. For tests in which the test speed in different from the rated speed, each test point shall be recalculated to the rated speed, using affinity laws. The tolerances for flow and head shall be applied in the following manner:

- The pump flow tolerance shall be applied to the guaranteed flow, Q_G, at the guaranteed head, H_G;
- The pump head tolerance shall be applied to the guaranteed head, H_G, at the guaranteed flow, Q_G.

Acceptance is achieved if either flow or head, or both, are found to be within the applicable tolerance. Therefore, the experimental head, H, power, P, and efficiency, η, at 1000 rpm were scaled to the rated speed (1800 rpm) and compared with their corresponding certificate curves. Indeed, Fig. 4.9, Fig. 4.10 and Fig. 4.11 show how the guaranteed point can be accepted because both the flow rate and the head are found within the applicable tolerance.

4.2.4 FFT Analysis

PCB pressure transducers were used in order to perform a FFT analysis. Two operating points (1080 rpm and 1200 rpm with 30 % opening valve) were acquired at high frequency (4 kHz) for 1 s by the PCB installed upstream the pump. As results, Fig. 4.12 shows that both signals are characterized by the prevailing harmonics, whose frequencies are equal to 6 times the respective mechanical frequencies (18 Hz at 1080 rpm and 20 Hz at 1200 rpm). This means that the number of blades is equal to 6.

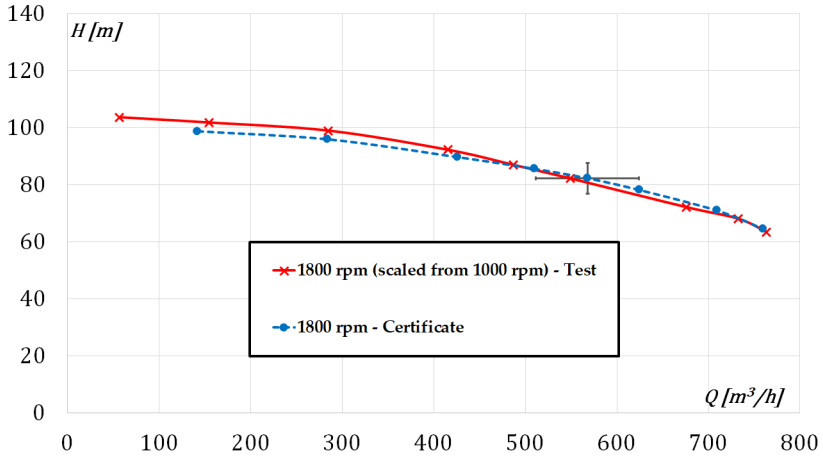

FIGURE 4.9: Experimental and certificate head, H, vs. discharge, Q, under pump operation mode at 1000 rpm.

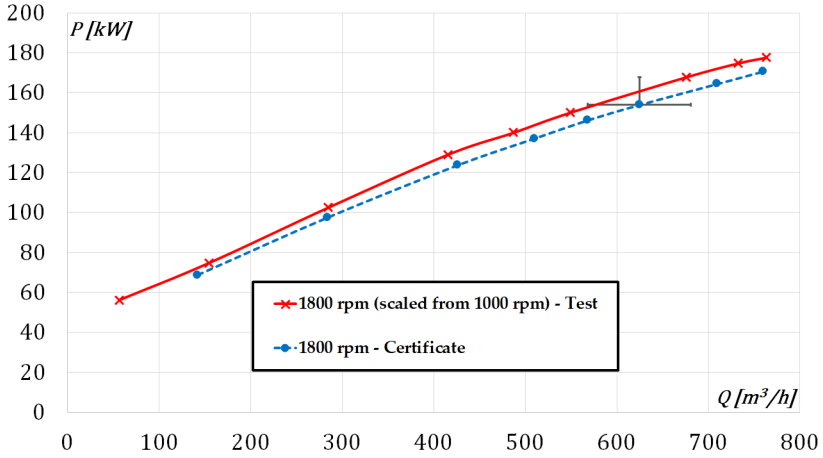

FIGURE 4.10: Experimental and certificate power, P, vs. discharge, Q, under pump operation mode 1000 rpm.

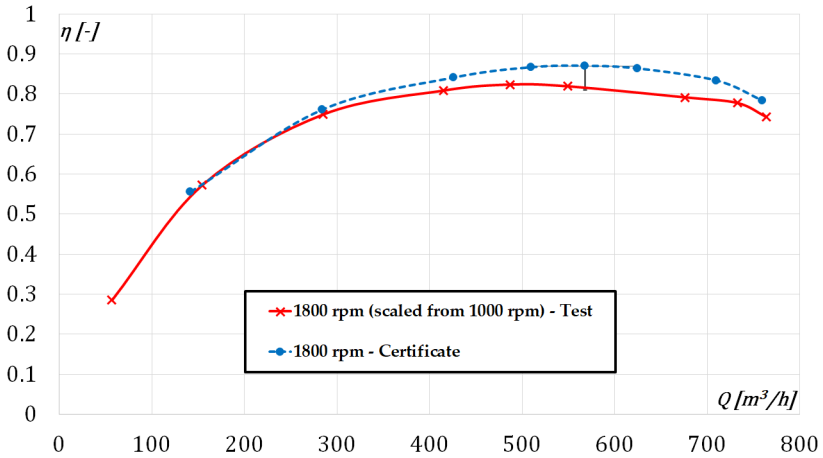

FIGURE 4.11: Experimental and certificate efficiency, η, vs. discharge, Q, under pump operation mode 1000 rpm.

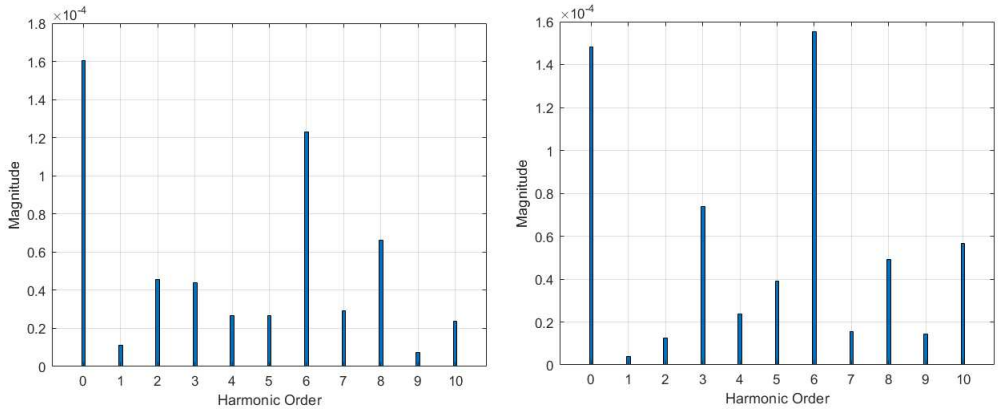

FIGURE 4.12: FFT of high frequency pressure measurements at 1080 rpm (left) and 1200 rpm (right).

4.3 Experimental Tests in Turbine Operation Mode

During turbine test, the user can remotely set the desired operating point of the booster pump by setting its rotational speed and the opening percentage of its control valve. The flow rate is pumped towards the PaT that can be ketp at constant rotational speed by varying the electric motor torque, whose value is transferred to the same four-quadrant AC/DC converter, at the different booster operation points. In this way, it is possible to characterize the machine for different flow rates at different rotational speeds. Once desired rotational speed and steady state condition are reached for each operating condition, user can acquire all the data useful for the machine characterization:

- Pressure downstream the turbine (p_A);
- Pressure upstream the turbine (p_B);
- Flow rate (Q);
- Rotational speed (N);
- Torque (C)

It was decided to acquire data at 1 s interval for a duration of 30 s also in turbine test. This means that for each parameter, 30 data are collected. A post processing procedure computes the average and the standard deviation for each sample of 30 collected data.

Also in turbine test, it is essential to evaluate the hydraulic losses in the piping, as for pump test. Hydraulic losses could be computed in a method as identical as in pump case, but it was necessary to change the local loss for gradual enlargement into a local loss for gradual contration in this case. Indeed, the flow rate is inverted and it flows through a gradual contraction before entering in the machine. For this reason, the local loss coefficient had to be changed in $\zeta = 0.03$ (Fig. 4.13).

Once the hydraulic loss were computed, it was possible to calculate the turbine head, by using equation 4.2, where the kinetic energy difference between section A and B was neglect. Also in this case, the mechanical power was obtained by multiplying the torque by the rotational speed, whereas the efficiency by dividing the the mechanical power, P, by hydraulic power, P_{hydr}.

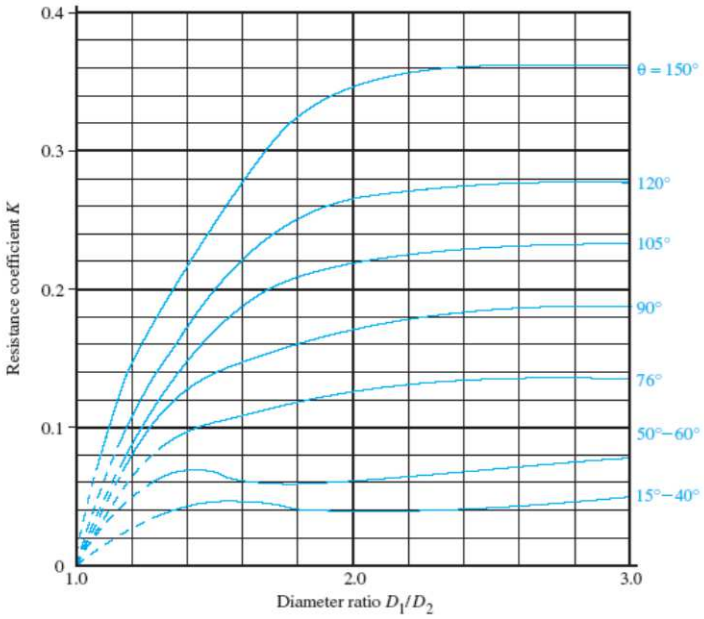

FIGURE 4.13: Local loss coefficient for gradual contraction [81].

$$P = C\left(\frac{2\,\pi\,N}{60}\right) \tag{4.11}$$

$$\eta = \frac{P}{P_{hydr}} = \frac{P}{\rho\,g\,H_t\,Q} \tag{4.12}$$

Fig. 4.14, Fig. 4.15 and Fig. 4.16 show the characteristic curves (H, P and η vs. Q) of the PaT under turbine operation mode at different rotational speeds: 760 rpm, 1000 rpm, 1200 rpm and 1520 rpm. The experimental efficiency points are provided with their standard deviation bands, whereas the standard deviation of the experimental head and power are within ± 3 %. Moreover, also the runway and the blocked rotor curves were acquired in order to examine the limit operating conditions in turbine mode.

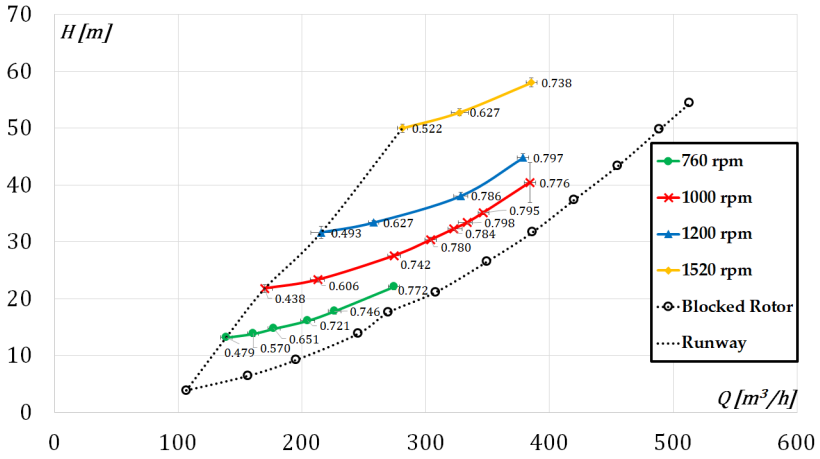

FIGURE 4.14: Experimental head, H, vs. discharge, Q, under turbine operation mode at different rotational speeds.

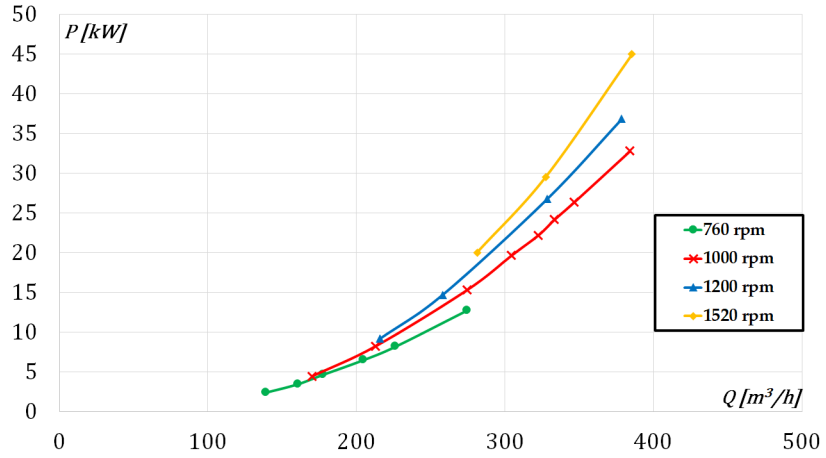

FIGURE 4.15: Experimental power, P, vs. discharge, Q, under turbine operation mode at different rotational speeds.

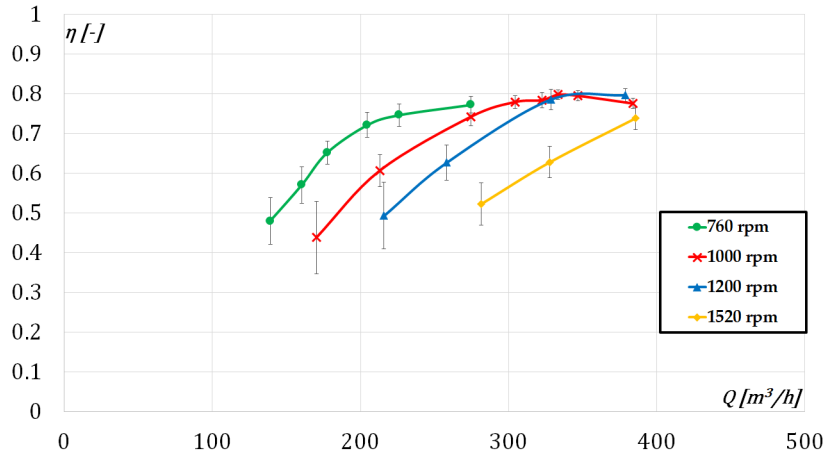

FIGURE 4.16: Experimental efficiency, η, vs. discharge, Q, under turbine operation mode at different rotational speeds.

4.3.1 Test repeatibility

Also in turbine mode the test at 1000 rpm was repeated three times in different months in order to test the repeatibility of measurements. Fig. 4.17, Fig. 4.18 and Fig. 4.19 show respectively the experimental head, power and efficiency at 1000 rpm measured in different months: May 2017, June 2017 and July 2018. Although months or years passed from one test to another, the similar performance curves were obtained.

4.3.2 Affinity laws

In order to test the experimental set up, curves at 760 rpm, 1200 rpm and 1520 rpm were also obtained by scaling the curve at 1000 rpm, using affinity laws. Indeed, Fig. 4.20 shows how the scaled points perfectly overlap the experimental ones.

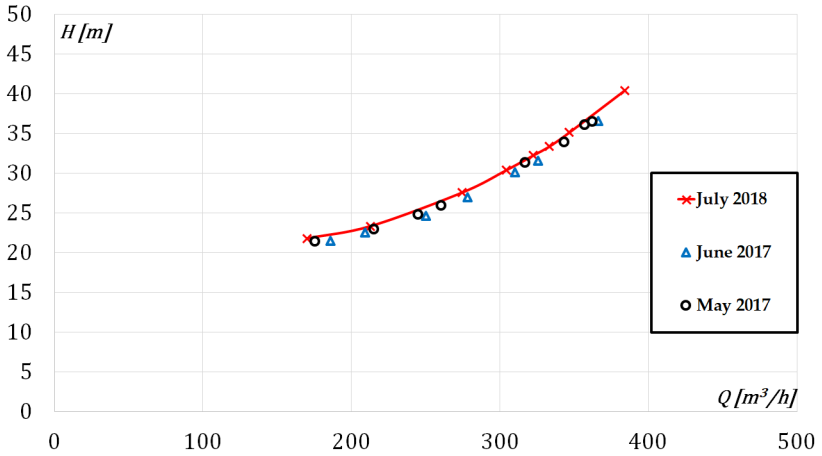

FIGURE 4.17: Comparison of experimental head curves, H, vs. discharge, Q, acquired in different measurements campaigns.

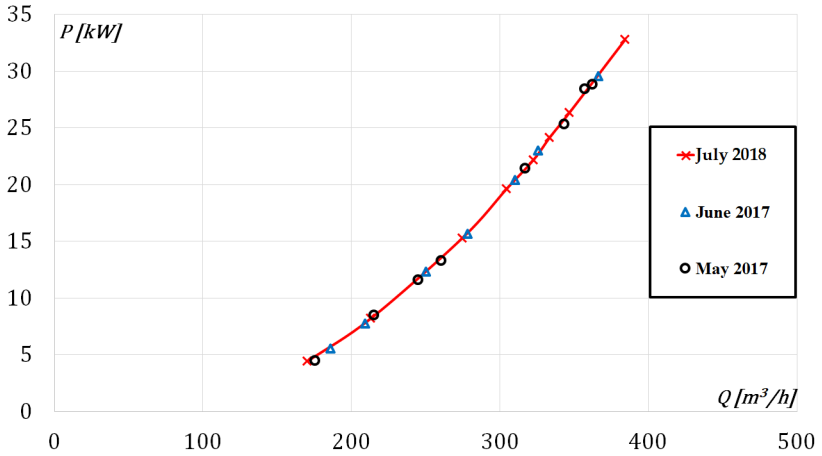

FIGURE 4.18: Comparison of experimental power curves, P, vs. discharge, Q, acquired in different measurements campaigns.

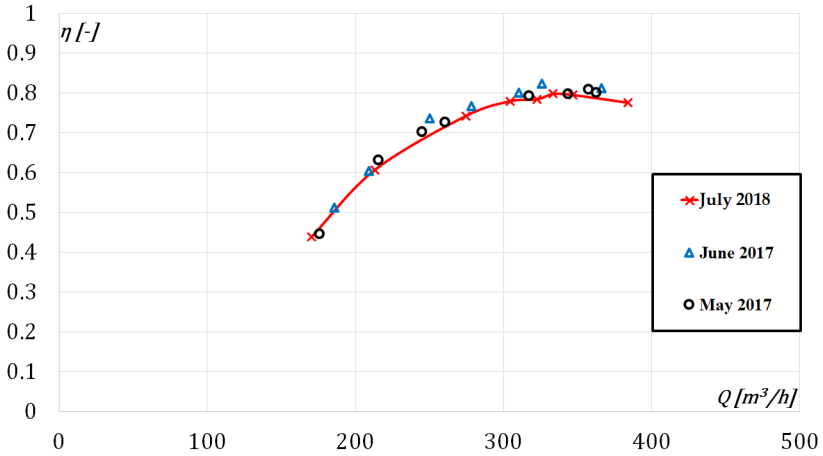

FIGURE 4.19: Comparison of experimental efficiency curves, η, vs. discharge, Q,acquired in different measurements campaigns.

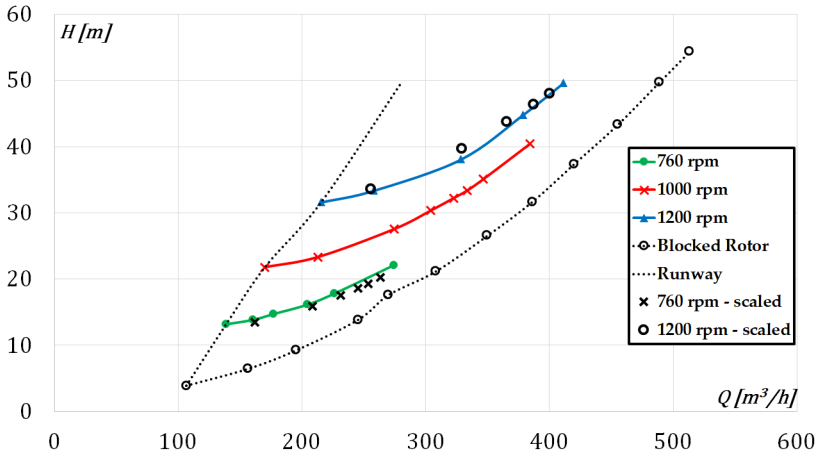

FIGURE 4.20: Comparison between the experimental head curves with the scaled ones under turbine mode operation.

4.4 Measurement uncertainty

In metrology, measurement uncertainty is a non-negative parameter characterizing the dispersion of the values attributed to a measured quantity. All measurements are subject to uncertainty and a measurement result is complete only when it is accompanied by a statement of the associated uncertainty. Uncertainty has a probabilistic basis and reflects incomplete knowledge of the quantity value. The uncertainty is classified in:

- Combined standard uncertainty, $u_c(y)$: it is the standard deviation, σ, which indicates the confidence interval of 68 %.
- Expanded uncertainty, $U(y)$: it is obtained by multiplying the standard deviation, $u_c(y)$, by coverage factors k. It indicates intervals where the measured values shows a higher confidence level. ($K = 2$ for a confidence of 95 % and $K = 3$ for a confidence of 99 %).

During measurements, two types of errors can occur: the systematic error, u_S, and the random error, u_R. The former always has the same value and the same sign, which depends mainly on the measuring instrument, whereas the latter includes all errors caused by environmental factors or that can be committed in the measurement procedure and present themselves with different values and sometimes even with opposite signs. The uncertainty of measurement is given by:

$$u = \sqrt{u_S^2 + u_R^2} \tag{4.13}$$

4.4.1 Procedure

Initially, the standard uncertainty and the 95 % expanded uncertainty were calculated for each direct measurement: flow rate, Q, torque, C, pressure, p, and rotational speed, N.

Since the number of samples for each set-point is $N_{samples} = 30$, a t-student distribution was considered for the values, which requires the knowledge of the number of degrees of freedom (DOF) in order to calculate of the extended uncertainty. In our case:

$$DOF = N_{samples} - 1 = 29 \tag{4.14}$$

Once degrees of freedom are calculated, it was possible to know the corrective factor ($t = 2.045$) that allows to compute the 95 % expanded uncertainty, according to the following equations:

$$u_{68\%} = \frac{\sigma}{\sqrt{N_{samples}}} = \frac{\sigma}{\sqrt{30}} \tag{4.15}$$

$$u_{95\%} = t\, u_{68\%} = 2.045\, u_{68\%} \tag{4.16}$$

Tab. 4.3 and 4.4 summarize the standard deviation and the uncertainty for direct measurements during pump test at 1000 rpm.

TABLE 4.3: Standard deviation and overall uncertainty for flow rate, torque and rotational speed (pump test - 1000 rpm).

Point	Q $[m^3/h]$	σ $[m^3/h]$	u_Q [%]	C $[Nm]$	σ $[Nm]$	u_C [%]	N $[rpm]$	σ $[rpm]$	u_N [%]
1	85.8	3.795	±1.7	166.3	1.521	±0.5	995.0	1.916	±0.1
2	158.3	3.896	±1.0	209.0	1.663	±0.5	995.4	0.892	±0.1
3	230.7	3.810	±0.8	227.1	1.712	±0.5	995.5	1.155	±0.1
4	270.6	4.206	±0.8	243.4	1.787	±0.4	994.9	1.151	±0.1
5	305.0	4.851	±0.8	257.9	1.348	±0.5	994.9	1.182	±0.1
6	375.3	4.474	±0.7	272.0	2.744	±0.5	994.9	1.325	±0.1
7	406.8	4.937	±0.7	283.2	2.332	±0.5	995.3	1.027	±0.1
8	424.2	4.256	±0.6	288.0	2.531	±0.5	994.7	0.979	±0.1

TABLE 4.4: Standard deviation and overall uncertainty for upstream, P_B, and downstream, P_A, pressure (pump test - 1000 rpm).

Point	p_B $[bar]$	σ $[bar]$	u_{P_B} [%]	p_A $[bar]$	σ $[bar]$	u_{P_A} [%]
1	3.908	0.031	±0.3	1.003	0.006	±0.2
2	3.821	0.061	±0.6	1.004	0.006	±0.2
3	3.606	0.037	±0.4	0.999	0.020	±0.7
4	3.440	0.041	±0.5	0.997	0.010	±0.4
5	3.291	0.053	±0.6	0.994	0.013	±0.5
6	3.107	0.036	±0.4	1.009	0.007	±0.3
7	2.977	0.073	±1.0	1.000	0.008	±0.3
8	2.853	0.045	±0.6	1.012	0.006	±0.2

Afterwards, the standard uncertainty for the head measurement was calculated. Since the head, H, the power, P, and the efficiency, η, are indirect measurements, it was necessary to apply uncertainty propagation formula:

$$u_c(y) = \sqrt{\left(\frac{\partial y}{\partial x_1} u_c(x_1)\right)^2 + \cdots + \left(\frac{\partial y}{\partial x_N} u_c(x_N)\right)^2} \tag{4.17}$$

where y is the indirect measurement (the head in our case), $x_1 \ldots x_2$ the variables on which the indirect measurement depends and $u_c(x_1) \ldots u_c(x_2)$ their respective uncertainties. Moreover, in order to obtain the extended uncertainty, it is necessary to calculate the equivalent degrees of freedom, ν_{eq}. This is done indirectly through the Welch-Satterthwaite formula. Then, each value of ν_{eq} was calculated for each value of head. Therefore, for each of them, it was calculated the t-student factor, t, that, multiplied by the standard uncertainty, gives the extended uncertainty.

TABLE 4.5: Permissible values of overall uncertainty, according to ISO 9906:2012 standard.

Quantity	**Grade 1** [%]	**Grade 2, 3** [%]
Flow rate	±2	±3.5
Speed of rotation	±0.5	±2.0
Torque	±1.4	±3.0
Pump total head	±1.5	±3.5
Power	±1.5	±3.5
Pump efficiency	±2.9	±6.1

Finally, it was possible to compute the overall uncertainty by means of equation 4.13. The standard UNI EN ISO 9906 provides the permissible values of overall measurement uncertainties, which are summarized in Tab. 4.5 for different acceptance grades. As example, Tab. 4.6 shows an uncertainty analysis for the experimental curves in pump mode(upper part) and the turbine mode (lower part) at 1000 rpm. All the performance values (i.e. Q, H, P, η) are provided with their overall uncertainties. These results are extremely low and they are within the permissible ranges imposed by the standard. Moreover, they and representative for all conducted laboratory measurements at different rotational speeds.

TABLE 4.6: Uncertainty analysis for the experimental curves in pump mode(upper part) and the turbine mode (lower part) at 1000 rpm.

Q $[m^3/h]$	H $[m]$	P $[kW]$	η $[-]$	u_Q [%]	u_H [%]	u_P [%]	u_η [%]
Pump							
85.8	30.5	17.6	0.749	±1.7	±0.6	±1.9	±1.7
158.3	28.5	22.1	0.809	±1.0	±0.6	±1.4	±1.3
230.7	26.8	24.0	0.824	±0.8	±0.6	±1.1	±0.9
270.6	25.4	25.7	0.819	±0.8	±0.6	±1.1	±0.9
305.0	23.4	27.3	0.796	±0.8	±0.5	±1.3	±1.1
375.3	22.3	28.8	0.792	±0.7	±0.6	±1.1	±0.8
406.8	21.0	30.0	0.778	±0.7	±0.6	±1.6	±1.4
424.2	19.6	30.5	0.743	±0.6	±0.6	±1.2	±1.0
Turbine							
209.3	23.2	7.8	0.594	±0.8	±2.2	±2.5	±3.4
212.9	23.3	8.2	0.606	±1.0	±1.8	±2.1	±3.0
274.4	27.6	15.3	0.742	±0.9	±1.1	±1.0	±1.7
304.3	30.4	19.6	0.780	±0.7	±1.2	±0.7	±1.6
322.4	32.2	22.2	0.784	±0.9	±1.0	±0.7	±1.5
333.4	33.4	24.2	0.798	±0.7	±0.9	±0.7	±1.3
346.7	35.1	26.4	0.795	±0.7	±0.9	±0.6	±1.3

Chapter 5

Proposed Performance Prediction Models

As mentioned in the introduction, PaTs can be considered a cost-effective alternative to traditional turbine as long as their turbine mode performance can be predicted. The two proposed prediction models are described in this chapter: (i) an experimental model for the prediction of the BEP of PaTs, as a selection tool for users; (ii) a 1-D model for the prediction of the entire characteristic, as a design tool for manufactures.

The first model has been proposed for users who would select the best PaT for a specific application. The model has been based on a greater number of samples constituted by gathering all the PaTs found in the literature, in order to have a better accuracy and a more general applicability in the prediction of PaT Best Efficiency Point.

The second model is a new 1-D prediction model, which has been developed in partnership with Nuovo Pignone in order to predict the entire characteristic of a PaT, by taking into account detailed geometrical information of the machine, hydraulic losses and the influence of the slip phenomenon at the outlet section of the runner during turbine operation. Three machines by Nuovo Pignone have been used as case studies (i.e., two single-stage centrifugal pumps, and a two-stages centrifugal pump). As results, the use of detailed geometrical information, the introduction of the slip factor and a new modeling of hydraulic losses have implied a more accurate prediction of the design and off-design operating points. Part of this chapter is already published in [83], [84] and [49].

5.1 Best Efficiency Point Prediction Model

Most of BEP prediction models have been developed for users who can only retrieve information from the pump datasheet (flow rate, head and efficiency at the BEP). For this reason, these prediction models are extremely simple but seldom consider off-design points. Furthermore, these models show a low applicability, being usually based on experimental correlations from a limited number of samples. For this reason, a literature survey of PaT models has been conducted and a new model, with a more general applicability, has been proposed.

5.1.1 Creation of the PaT sample

Thanks to the literature survey, a sample constituted by 27 pumps tested in turbine mode has been considered. These machines operate in a a wide range of specific speed, $N_{s,P}$, from 9 to 80 (rotational speed, N, in rpm flow rate, Q, in m^3/s and head, H, in m). All pumps are listed in Tab. 5.1, sorted by $N_{s,P}$, with their main

characteristic values at BEP, both under pump and turbine operation modes. The KSB Etanorm PaT in the list is the machine that was installed and tested in the test rig of the Department of Mechanics, Mathematics and Management of the Polytechnic University of Bari. The experimental BEP of the machine has been included in the data set.

The approach of some authors (Singh [38], Nautiyal [36] Derakhshan [35], Tan [40] and Barbarelli [14]) is to predict the BEP under turbine operation mode by correlating the prediction factors $h = H_{BEP,T}/H_{BEP,P}$ and $q = Q_{BEP,T}/Q_{BEP,P}$ to the pump specific speed under pump mode operation, $N_{s,P}$. Other authors (Yang [12], Alatorre [3], Sharma [43]) have preferred to correlate h and q to the best efficiency in pump mode, $\eta_{BEP,P}$

As known, the specific speed number, N_s, allows one to correlate the parameters of machine performance (rotational speed, N, flow rate, Q, and head, H) to the shape of the impeller. Therefore, N_s is a more useful engineering tool than the pump efficiency at BEP in the prediction of PaT performance. For this reason, in this work, the proposed prediction method is actually based on the $N_{s,P}$.

TABLE 5.1: BEPs of pumps tested in both modes in literature.

Pump	$N_{s,P}$ [−]	$Q_{BEP,P}$ [m^3/h]	$H_{BEP,P}$ [m]	$\eta_{BEP,P}$ [−]	$Q_{BEP,T}$ [m^3/h]	$H_{BEP,T}$ [m]	$\eta_{BEP,T}$ [−]	$N_{s,T}$ [−]
Barbarelli 1	9.05	26.6	33.01	0.44	47.09	93.28	0.43	5.52
Barbarelli 2	9.48	27.1	31.41	0.45	50.8	110.8	0.35	5.04
Barbarelli 3	12.8	25.1	20	0.55	38.3	43.66	0.51	8.81
Derakhshan 1	14.97	28.8	17.8	0.65	44.86	36.48	0.64	10.9
Barbarelli 4	16.34	19	12	0.55	34.99	25.5	0.59	12.6
Barbarelli 5	20.23	59.4	19.3	0.65	93.67	38	0.65	15.28
Singh 1	20.98	38.9	14.5	0.77	71.76	25.81	0.725	18.49
Derakhshan 2	23.26	85.3	20.4	0.76	135.9	39.83	0.73	17.77
Singh 2	24.46	95.4	21.5	0.78	180.8	47.37	0.765	18.62
Barbarelli 6	25.47	96.4	19.6	0.73	145	33.2	0.73	21.01
KSB Etanorm	26.44	302.5	24.4	0.784	333.4	33.4	0.798	21.90
Barbarelli 7	28.72	35	8.5	0.67	55	13.1	0.73	26.03
Barbarelli 8	30.3	87	14.52	0.74	131.47	22.4	0.78	26.91
Barbarelli 9	31.21	83.5	12.02	0.72	112.39	17.6	0.76	29.82
Singh 3	35.33	91.4	12.8	0.785	118.8	20.66	0.81	28.12
Singh 4	36.42	55.1	8.38	0.744	84.79	14.43	0.715	30.06
Pugliese 1	37.67	148	39	0.787	217.18	72.29	0.83	28.73
Derakhshan 3	39.52	205.9	18.1	0.865	304.5	31.26	0.74	31.89
Singh 5	39.66	237.2	19.8	0.85	320.2	27.81	0.835	35.71
Barbarelli 10	43.48	150	12.9	0.76	180	18.8	0.84	35.91
Pugliese 2	44.76	88.5	44	0.765	108.3	57.21	0.86	40.67
Singh 6	45.16	118.8	10.5	0.8	163.56	14.72	0.8	41.13
Singh 7	46.28	48.6	5.6	0.76	64.25	8.75	0.76	38.08
Derakhshan 4	55.43	385.2	17.5	0.87	439.1	23.45	0.78	47.52
Singh 8	61.26	104	6.4	0.72	161.8	9.32	0.743	57.63
Barbarelli 11	64.04	208.5	9.59	0.82	303.59	13.3	0.84	60.46
Barbarelli 12	77.39	77.39	5.32	0.78	157.1	7.82	0.7	64.77
Singh 9	79.21	370.8	10.6	0.84	469.36	14.64	0.755	69.95

5.1.2 Experimental correlations

Thanks to the collected experimental data, the specific speed number under turbine mode operation, $N_{s,T}$, and $N_{s,P}$ have been correlated. Successively, the head prediction factor, h, and the empirical $N_{s,T}$ have been correlated. Fig. 5.1 and Fig. 5.2 show these correlations with the interpolating curves, written in equation 5.1 and equation 5.2.

Considering the data trend, a linear interpolating curve has been used for the correlation between $N_{s,T}$ and $N_{s,P}$, showing an R squared value equal to 0.98. This means a good agreement with experimental data. In the case of correlation between h and $N_{s,T}$, a third order polynomial has been considered, due to the highest R squared value (equal to 0.82), if compared with logarithmic or power trend lines.

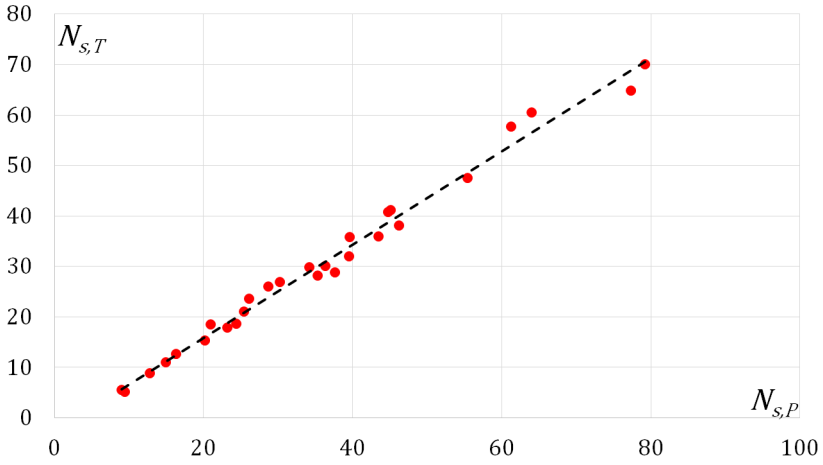

FIGURE 5.1: Specific speed number in turbine mode, $N_{s,T}$, vs. specific speed number in pump mode, $N_{s,P}$.

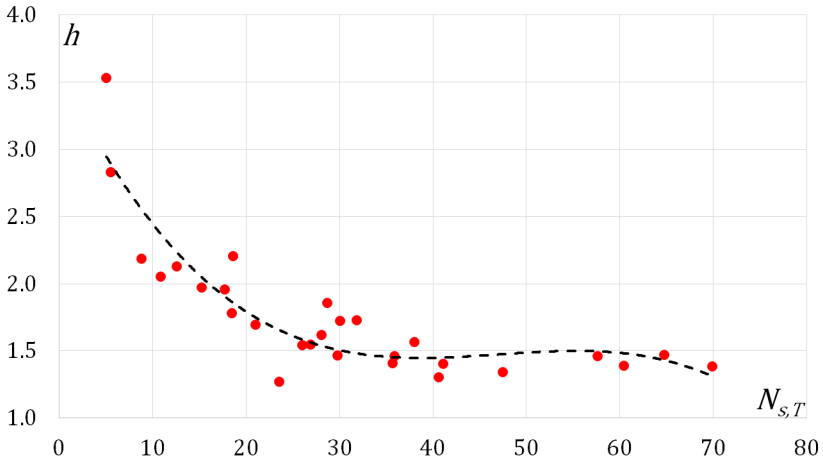

FIGURE 5.2: Head prediction factor, h, vs. specific speed number in turbine mode, $N_{s,T}$.

The procedure that allows one to predict the turbine operation mode at BEP is summarized as follows: once the specific speed under pump operation mode, $N_{s,P}$, has been calculated, it is possible to evaluate the specific speed under turbine operation mode, $N_{s,T}$, by using equation 5.1. The head prediction factor, h, can be calculated thanks to $N_{s,T}$ with equation 5.2:

$$N_{s,T} = 0.9237 N_{s,P} - 2.6588 \tag{5.1}$$

$$h = -0.000023 N_{s,T}^3 + 0.003206 N_{s,T}^2 - 0.145781 N_{s,T} + 3.604636 \tag{5.2}$$

Therefore, the head, $H_{BEP,T}$, and discharge, $Q_{BEP,T}$, at BEP in reverse mode can be calculated by means of the following equations:

$$H_{BEP,T} = h\, H_{BEP,P} \tag{5.3}$$

$$Q_{BEP,T} = \left(\frac{N_{s,T}\, H_{BEP,T}^{3/4}}{N} \right)^2 \tag{5.4}$$

Obviously the model allows not only to predict the BEP in turbine mode of a single stage centrifugal pump, but also to help the user to select the proper pump for a specific site. Fig. 5.3 depicts the flowchart for the selection of a pump to be used as turbine for a specific site. Indeed, the flow rate and the head of the site, Q_{site} and H_{site}, represent the operating condition that the PaT should respect at its BEP. Thanks to this values, it is possible to evaluate the required specific speed of the site (equal to the turbine specific speed, $N_{s,T}$). Then, the specific speed that the machine should have in pump mode can be calculated by means of equation 5.1. Afterwards, the head at BEP in pump mode can be computed by means of equation 5.2, whereas the flow rate by means of the definition of specific speed. At this point, the user may consult pump catalogs in order to select respectively the pump family and the specific pump.

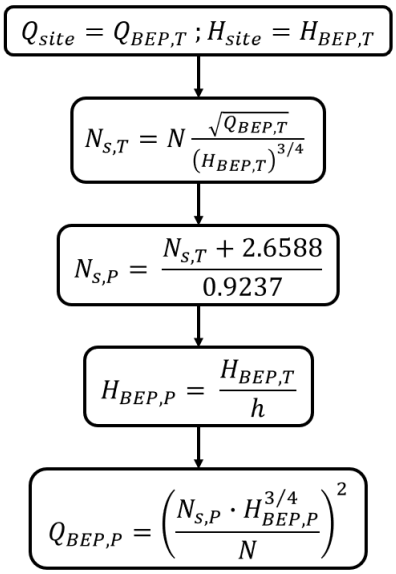

FIGURE 5.3: Selection flowchart for the selection of a pump to be used in turbine mode.

5.1.3 Results and discussion

The proposed PaT performance prediction model has been applied to a different set of 11 pumps found in other recent works [40], [85], [86], [20], [12]. The proposed

model has been compared with other models in terms of both head and flow rate prediction errors. Indeed, Fig. 5.4 and Fig. 5.5 show the comparison of relative error in estimating the head, $H_{BEP,T}$, and discharge, $Q_{BEP,T}$, with respect to the experimental data, e_H and e_Q for each pump.

$$e_H = \frac{H_{predicted} - H_{experimental}}{H_{experimental}}, \; e_Q = \frac{Q_{predicted} - Q_{experimental}}{Q_{experimental}} \tag{5.5}$$

The model shows a good applicability with a wide range of pumps that are different not only in terms of operating BEPs, but also because they are produced by different manufacturers. Indeed, 7 pumps out of 11 are characterized by a head prediction error within ± 10 %, whilst 8 out of 11 are characterized by a discharge prediction error within ± 10 %.

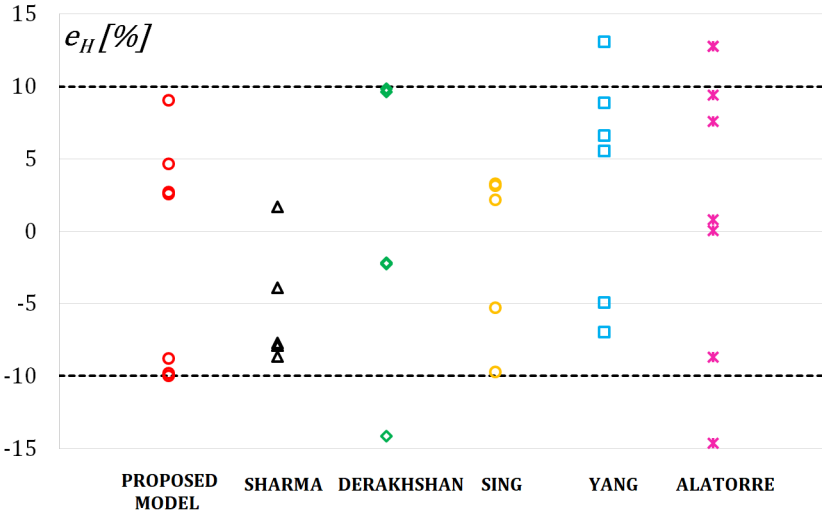

FIGURE 5.4: Comparison of different models for BEP in turbine mode in terms of head prediction error, e_H.

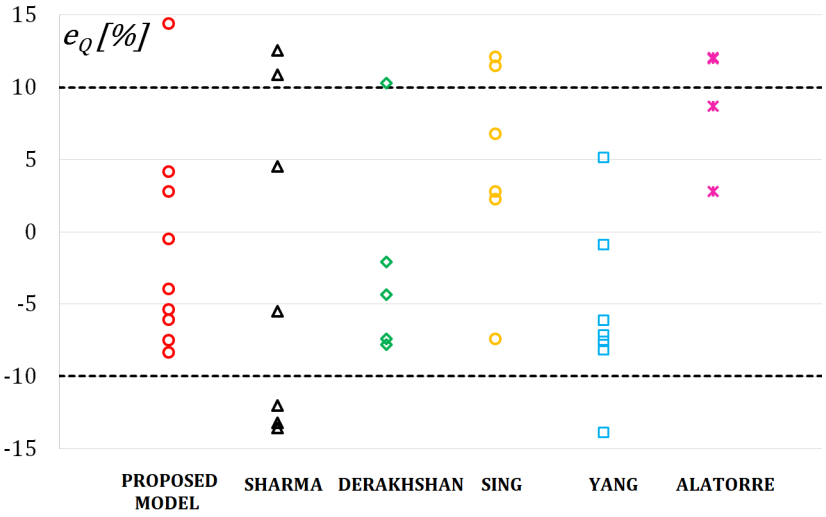

FIGURE 5.5: Comparison of different models for BEP in turbine mode in terms of flow rate prediction error, e_Q.

Obviously, the results given by models in this field depend both on the proposed method and on the set of machines used for calibration. As the calibration set gets

richer, the model can gain in generality but may lose accuracy. Indeed, the new 11 pumps, used to validate the model, have been added to the starting data set. As result, the new interpolating curve $N_{s,T} = f(N_{s,P})$ shows a R squared value equal to 0.98, similar to the previous one. On the contrary, the correlation between h and $N_{s,T}$ shows a R squared value equal to 0.72, which is lower than the previous one (0.82). At this point, it is fair to wonder whether partitioning the starting data set by a particular property of the pumps, could lead to more accurate forecasts. In this way, it could be possible to obtain "specialized" models to be applied only to the pumps with that property. For example, our data set of centrifugal pumps can be partitioned by the specific speed of the pump in order to take into account both the geometry and the performance of the machines. According to Fig. 5.6, it is possible to split the data set into three ranges of $N_{s,P}$ ($10 \div 20$ for radial-vane types, $20 \div 60$ for Francis-vane types and $60 \div 100$ for mixed-flow types). Tab. 5.2 reports the R squared values of the two experimental correlations of the model for each machine type group. In the radial-vane types, the R values are higher than the ones of the proposed model, whereas there is a significant decrease for Francis-vane and Mixed-flow types. Probably, further experiments are thus required in order to add a bigger number of pumps for each specific sample.

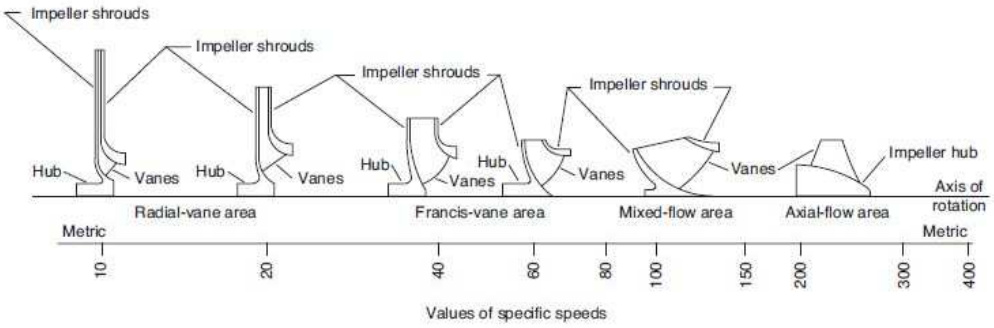

FIGURE 5.6: General pump impeller types.

TABLE 5.2: Comparison of the R squared values of correlation trend lines for different impellers types.

	R Squared Value		
	Radial-vane types	Francis-vane types	Mixed-flow types
$N_{s,T} = f(N_{s,P})$	0.994	0.902	0.942
$h = f(N_{s,T})$	0.966	0.577	0.579

5.2 Nuovo Pignone PaTs: First Studies

Nuovo Pignone, as leader company in pump manufacturing, showed a strong interest in the study of its machines in reverse mode. Indeed, Nuovo Pignone developed a model in the past, which was able to predict both the BEP and the characteristic curve of its machines in reverse mode. The objective of our collaboration with Nuovo Pignone has been to improve its pre-existing home-made model and to study more deeply the behavior of their pumps operating in turbine mode. As first step, Nuovo Pignone has selected and tested seven machines in both modes. Tab. 5.3 reports the main characteristics of these machines, where information about the type, diameter or other detailed information are not described for confidential reasons.

TABLE 5.3: List of Nuovo Pignone pumps tested in reverse mode.

Pump	Stages	Type	$N_{s,P}$
Pump 1	4	A	11.91
Pump 2	5	A	20.88
Pump 3	8	A	22.06
Pump 4	6	A	23.23
Pump 5	2	B	28.12
Pump 6	3	C	37.05
Pump 7	1	D	40.17

As indicated in Tab. 5.3, the sample is heterogeneous because of the need to create a sample as general as possible. Indeed, the selected machines are different from each other not only in terms of specific speed, but also in terms of type of machine and number of stage (up to 8 stages). The specific speed of each machine is calculated as the stage specific speed, as stated by equation 5.6:

$$N_s = N \frac{\sqrt{Q_{BEP}}}{(H_{BEP}/N_{stages})^{0.75}} \tag{5.6}$$

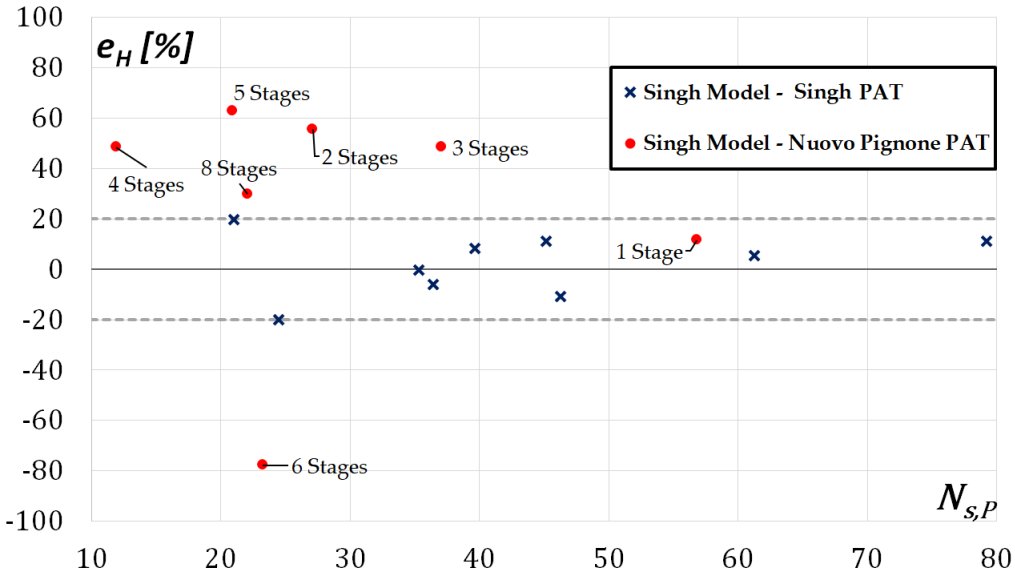

FIGURE 5.7: BEP head prediction error, e_H, of Sing's model applied to own PaTs and Nuovo Pignone PaTs.

All the BEP prediction models found in the literature and described in the background, have been applied to Nuovo Pignone PaTs. Unfortunately, this particular sample has highlighted how these models are not sufficiently general in order to predict the BEP in turbine mode of each PaT. Indeed, these kind of models are constitued by experimental correlations, which are based on a limited number of samples. For example, the model proposed by Singh [38] has been applied both to those PaTs tested by Singh and to Nuovo Pignone machines. It is possible to notice in Fig. 5.7 how the model can predict better the head at BEP of Singh's PaTs than Nuovo Pignone machines. The figure shows the BEP head prediction error, e_H, vs. the specific speed in pump mode, $N_{s,P}$. This means that each $N_{s,P}$ corresponds to a specific PaT.

All the Singh's PaTs are within 20 % error range, whereas Nuovo Pignone PaTs are out of this range. Probably, this is due to the fact that Nuovo Pignone sample is constituted by machines different from those tested by Singh (only single stage centrifugal pumps). Indeed, only the single-stage PaT is within the tolerance range.

At this point, as first step of this work, the pre-existing model has been tuned on all the PaTs tested by Nuovo Pignone in order to reduce the overall error prediction on the entire curve in reverse mode. Indeed, Fig. 5.8, Fig. 5.9 and Fig. 5.10 show the results of this preliminary assessment on the 2-stages, 5-stages and 6-stages PaTs, as examples. Figures illustrate the comparison of some experimental models found in literature (i.e. Sharma [43] and Derakshan [35]) with the pre-existing model and the new tuned one in terms of head prediction error on the whole experimental curve in turbine mode. Sharma and Derakshan have been selected because they are able to predict both the BEP and the curve in turbine mode.

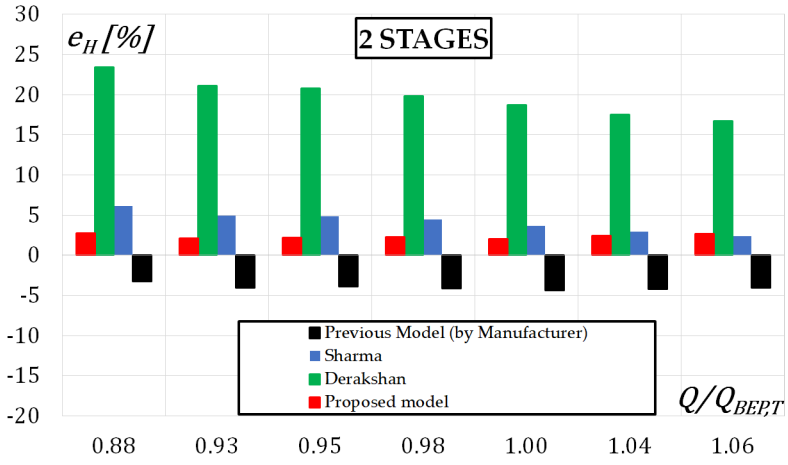

FIGURE 5.8: Comparison of models in terms of head prediction error, e_H, in the prediction of the curve in turbine mode of the 2-stages pump.

As first aspect, there is an evident variability in results of the models from one machine to another. Indeed, models overestimates the head for all the flow rates in some cases, whereas in other cases, they underestimate the head at low flow rates and overestimate the head at high flow rates or vice versa. Furthermore, the tuning of the previous model by Nuovo Pignone has involved an overall reduction of head prediction error with respect to the previous one.

Although this improvement, the model is based on experimental correlation on a limited number of machines (in this case the Nuovo Pignone sample), yet. For this reason, it has been necessary to develop a model more accurate than the pre-existing

one, which takes into account theoretical aspects, some complex phenomena like hydraulic losses and the real geometry of the machine in order to better estimate the behavior in reverse mode. Indeed, a 1-D model has been proposed as a tool that could support Nuovo Pignone to predict the turbine mode performance from the knowledge of pump characteristics. This model will be accurately described in the next section.

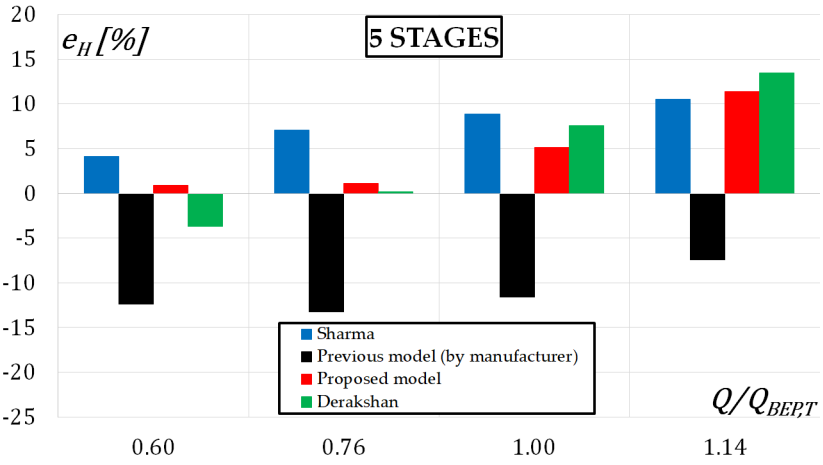

FIGURE 5.9: Comparison of models in terms of head prediction error, e_H, in the prediction of the curve in turbine mode of the 5-stages pump.

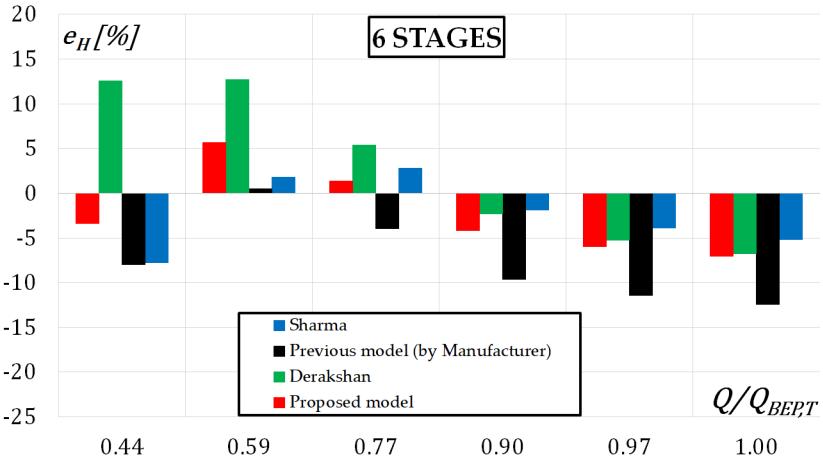

FIGURE 5.10: Comparison of models in terms of head prediction error, e_H, in the prediction of the curve in turbine mode of the 6-stages pump.

5.3 Curve Prediction Model

Thanks to the partnership with a leader company in pump manufacturing, Nuovo Pignone, a new theoretical 1-D model is proposed in order to predict the entire characteristic of a PaT starting from the knowledge of its geometrical parameters and the availability of related tests in turbine mode operation.

Theoretical methods are quite comprehensive but they are difficult to be applied in practice because they need very detailed geometric information, which are available only to manufacturers. For this reason, the development of an accurate analytical prediction model needs a strong collaboration with manufacturers in order to merge both the academic and the industrial know-hows and create a tool that could support them not only in the prediction of the turbine mode operation, but also to design *ad hoc* PaTs.

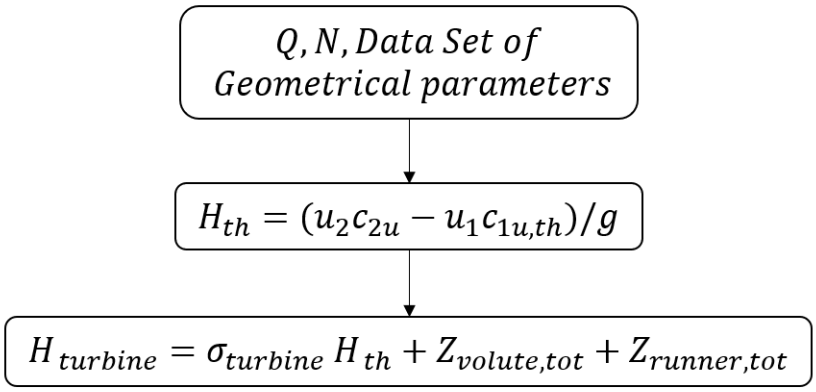

FIGURE 5.11: Flow chart of the proposed model.

Fig. 5.11 schematically shows how the proposed model works: thanks to the knowledge of detailed geometrical data, flow rate, Q, and rotational speed, N, it is possible to accurately calculate the correct velocity triangles and the theoretical head, H_{th}, in reverse mode operation. Afterwards, volute and runner losses are modeled to finally predict the real PaT head, $H_{turbine}$.

Fig. 5.12 depicts typical velocity triangles in turbine mode. According to Gülich [44], the proposed model leaves unchanged for PaT the conventional section numbers used for pumps:

- Section 4 for the volute inlet or the discharge nozzle;
- Section 3 for the volute throat section;
- Section 2 for the inlet runner section;
- Section 1 for the outlet runner section.

In Fig. 5.12, w, c and u are the relative, the absolute and the tangential velocities, respectively. The absolute and the relative flow angles are α and β, respectively, whereas i_2 is the the incidence at the leading edge of runner blade.

Gülich was one of the first to propose a theoretical approach with simplified assumptions. If compared to Gülich's approach, the introduction of a detailed geometry, instead of a simplified geometry (square shaped cross sections of the machine), requires the use of new hydraulic parameters, which allow a better prediction of the turbine head. These parameters are:

- The flow incidence loss at the inlet section of the runner;
- The blade blockage factor that influences the inlet velocity triangles, causing the contraction of the inlet cross section area, hence a loss due to the variation of the radial velocity component;
- The slip factor, $\sigma_{turbine}$, i.e., the ratio between the real, $W_{turbine}$, and the theoretical turbine work, W_{th}.

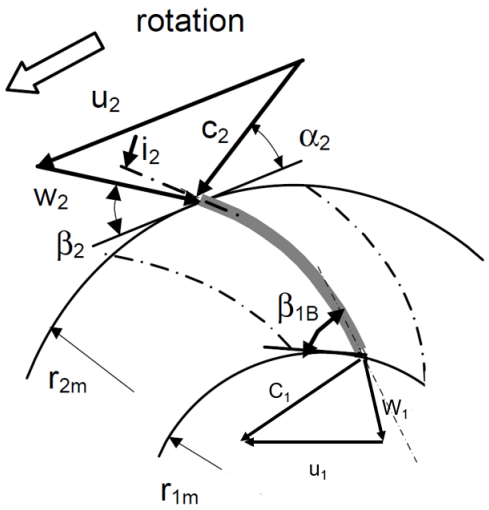

FIGURE 5.12: Velocity triangles in turbine mode.

This last parameter contemplates the influence of a limited number of runner vanes on the flow deflection with respect to the outlet blade angle during turbine mode operation. Actually, this deflection causes a reduction of the Euler's work. The results of the new prediction model have shown a more accurate prediction of the PaT performance, under design and off-design conditions, than the results of other prediction models found in the literature.

5.3.1 Theoretical Work

As mentioned in the previous paragraph, the first step of the model is to calculate the theoretical head of the PaT, H_{th}, by evaluating velocity triangles in both inlet and outlet sections of the runner. The objective is to calculate the circumferential components of the absolute velocities, c_{2u} and $c_{1u,th}$, in order to estimate the theoretical work, W_{th} by means of Euler's equation:

$$W_{th} = u_2 \, c_{2u} - u_1 \, c_{1u,th} \tag{5.7}$$

Section 3: Volute Throat Area

During turbine mode operation, the fluid flows across the machine in a reverse mode. Before entering the runner, the flow is guided by the pump volute. The correct knowledge of the volute throat area is important for the calculation of the fluid velocity in the volute. Indeed, some researchers, like Gülich [44] and Barbarelli [45], consider a square shaped area instead of the real shape of the volute throat area, which could be for example trapezoidal. This assumption overestimates the fluid

velocity. Thus, it is possible to calculate fluid velocity in this section, c_3, by knowing the flow rate, Q, and the volute throat area, A_3. Its circumferential component is $c_{3u} \cos \alpha_3 = c_{3u} \cos \alpha_{3B}$, where α_{3B} is the outflow geometrical angle from the throat area. The blade angle, α_{3B}, can be estimated from the throat volute height, a_3, and the pitch, t_3, as depicted in Fig. 5.13. As proposed by Gülich, since $\alpha_{3B} = \arcsin(a_3/t_3)$ is a relatively small angle, errors in assuming $\alpha_3 \approx \alpha_{3B}$ have a negligible effect on $\cos \alpha_{3B}$.

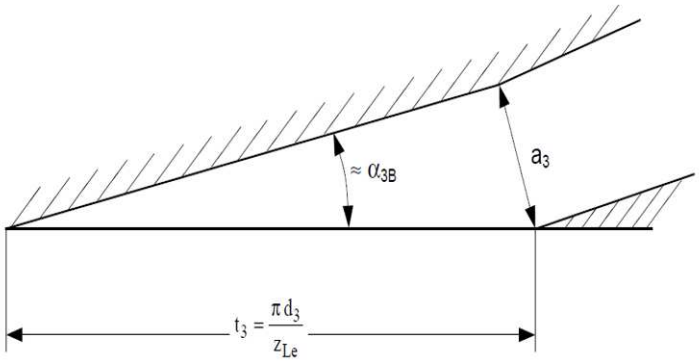

FIGURE 5.13: Evaluation of the outflow angle, α_3, from throat height, a_3, and pitch, t_3 [44].

Section 2: Runner Inlet Section

The flow rate entering the runner is reduced by the effect of the volumetric efficiency, η_v, due to leakage losses.

Thanks to the knowledge of the mean outer diameter, D_{2m}, the axial width of the the runner channels, b_2, and the number of blades, Z_{blades}, it is possible to calculate the inlet cross area of the runner, A_2. For double-exit impellers (double suction impellers or double discharge runners), b_2 and Q are defined per side of the impeller.

$$A_2 = (\pi D_{2m} b_2) / Z_{blades} \tag{5.8}$$

Once A_2 is calculated, it is possible to evaluate the inlet velocity triangle. Indeed, the first step is to calculate the meridian component of the absolute velocity vector, c_{2m}. The circumferential component c_{2u} is obtained by applying the free vortex theory:

$$c_{2u} = c_{3u} \frac{r_{3,eff}}{r_{2m}} \tag{5.9}$$

where r_{2m} is the mean outlet radius and $r_{3,eff}$ is the effective radius of the center of the volute throat area [44]:

$$r_{3,eff} = r_3 + e_3 + k_3 a_3 \tag{5.10}$$

In equation 5.10, k_3 is an empirical coefficient ($0.2 \leq k_3 \leq 0.5$), which contemplates the aspect ratio of the volute throat area, whereas a_3 is the height of the volute throat area and e_3 is the volute tongue thickness. Thus, knowing c_{2m}, c_{2u} and the tangential velocity, u_2, it is possible to calculate the absolute, α_2, ad relative, β_2, fluid angles.

$$\alpha_2 = \arctan\left(\frac{c_{2m}}{c_{2u}}\right) \tag{5.11}$$

$$\beta_2 = \arctan\left(\frac{c_{2m}}{u_2 - c_{2u}}\right) \tag{5.12}$$

Section 1: Runner Outlet Section

Also for the outlet section of the runner, the cross area A_1 is calculated by means of the mean outlet diameter, D_{1m}, the radial width of the channel, b_1, and the blade blockage factor, ξ_1.

$$A_1 = (\pi D_{1m} b_1 \xi_1) / Z_{blades} \tag{5.13}$$

where the blade blockage factor at the outlet section of the runner, ξ_1, depends on the blades number, Z_{blades}, the thickness of the trailing edge blade, e_1, outlet runner blade angle, β_{1B} and tip diameter in the outlet runner section, $D_{1,tip}$:

$$\xi_1 = 1 - \frac{Z_{blades}\, e_1}{\pi\, \sin\beta_{1B}\, D_{1,tip}} \tag{5.14}$$

Knowing flow rate flowing through the runner, $Q_{runner} = Q\ \eta_v$, (with the assumption that the volumetric efficiency is equal to the volumetric efficiency of the machine in direct mode, $\eta_v = \eta_{v,P}$) and the cross area, A_1, the meridian component of the relative outlet velocity, w_{1m}, is obtained.

Once the meridian component of the relative velocity vector is calculated, w_{1m}, the circumferential component of the theoretical relative velocity, $w_{1u,th}$, can be calculated.

$$w_{1u,th} = w_{1u,m}\, \frac{\sin\beta_{1B}}{\cos\beta_{1B}} \tag{5.15}$$

Thus, the theoretical absolute circumferential component $c_{1u,th}$ can be obtained by means of $w_{1u,th}$ and u_1.

$$c_{1u,th} = u_1 - c_{1u,th} \tag{5.16}$$

Finally, it is possible to calculate the theoretical head, H_{th}, with equation 5.7.

5.3.2 Volute Losses

Fig. 5.14 shows a generic double volute constituted by the inner and the outer volute. Volute losses are evaluated for the inner volute because of the inner volute losses are assumed equal to the outer volute losses. In Fig. 5.14, the inner volute has been divided into three parts: the inlet convergent channel (part 1), half volute collector (part 2) and the vane-less space between the throat volute section and the runner inlet section (part 3).

Generally, two kinds of losses are considered in the volute: friction losses, Z_f, and local losses, Z_L, both determined according to the following equations:

$$Z_f = f\, \frac{L}{D_h}\, \frac{c^2}{2g} \tag{5.17}$$

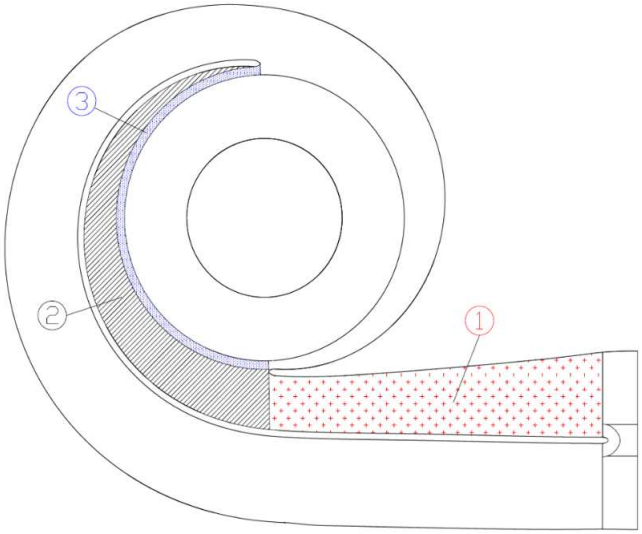

FIGURE 5.14: Division of the volute.

$$Z_L = \zeta \frac{c^2}{2g} \tag{5.18}$$

Head loss coefficient in the inlet convergent nozzle, $\zeta_{vol,1}$, is calculated by means of equation 5.19

$$\zeta_{vol,1} = \left(\frac{\bar{c}_{4-3}}{u_2}\right)^2 \left(\zeta_c + f \frac{L_{4-3}}{D_{h,nozzle}}\right) \tag{5.19}$$

The discharge nozzle is a convergent channel, which starts from the discharge Section 4 and ends in the throat volute Section 3.

In equation 5.19, $\bar{c}_{4-3}$, L_{4-3}, $D_{h,nozzle}$ are the mean velocity, the length and the hydraulic diameter of the inlet convergent channel, whereas ζ_c is a loss coefficient, which contemplates losses due to the sudden geometrical enlargement after the throat volute section. f is the friction coefficient that depends on the Reynolds number and the relative roughness of the volute, ϵ_{vol}.

$$f = \frac{0.31}{\left[\log\left(0.135 \frac{\epsilon_{vol}}{D_{h,nozzle}} + \frac{6.5}{Re_{4-3}}\right)\right]^2} \tag{5.20}$$

with:

$$Re_{4-3} = \frac{\bar{c}_{4-3}\, D_{h,nozzle}}{\nu} \tag{5.21}$$

$$D_{h,nozzle} = 4\frac{A_4 + A_3}{p_4 + p_3} \tag{5.22}$$

The loss coefficient for the volute collector is calculated by means of the following equation 5.23

$$\zeta_{vol,2} = \sum_{i=1}^{N} \frac{c_{f,i}\, c_{vol}^3}{A_{wet,i}\, Q_i\, u_2^2} \tag{5.23}$$

In this case, the volute collector is divided into N parts and their wet surfaces A_{wet} and the mean velocity in the volute, c_{vol}, are calculated. Actually, the volute collector is an open channel and the a loss coefficient for flat plates was considered, as stated in equation 5.24

$$c_f = \frac{0.136}{\left[-\log\left(0.2\frac{\epsilon_{vol}}{L_{collector}} + \frac{12.5}{Re_{collector}}\right)\right]^{2.15}} \tag{5.24}$$

where:

$$Re_{collector} = \frac{c_{vol}\ L_{collector}}{\nu} \tag{5.25}$$

As suggested by Gülich, friction losses in the vane-less space, $\zeta_{vol,3}$, are calculated by equation 5.26

$$\zeta_{vol,3} = \frac{c_f\ r_2}{b_3\ \sin\alpha_3\ (\cos\alpha_3)^2}\left(\frac{c_{3,u}}{u_2}\right)^2\left(1 - \frac{r_2}{r_3}\right) \tag{5.26}$$

Finally, the total volute head loss, $Z_{vol,tot}$, is obtained by summing up all the volute loss contributes:

$$Z_{vol,tot} = \left(\zeta_{vol,1} + \zeta_{vol,2} + \zeta_{vol,3}\right)\frac{u_2^2}{2g} \tag{5.27}$$

5.3.3 Runner Losses

Runner losses have different contributes. The first, $\zeta_{runner,1}$, is connected to the friction loss coefficient inside the impeller channel. As suggested by Gülich, this coefficient could be calculated by means of equation 5.28:

$$\zeta_{runner,1} = 4c_d\ \frac{L_{1-2}}{D_{h,runner}}\left(\frac{w_{av}}{u_2}\right)^2 \tag{5.28}$$

where L_{1-2} is the c-line blade length, $D_{h,runner}$ is the hydraulic diameter of the impeller channel, w_{av} is the average relative velocity between w_1 and w_2 and c_d is the corrected friction loss for flat plates:

$$D_{h,runner} = 4\ \frac{A_2 + A_1}{p_2 + p_1} \tag{5.29}$$

$$p_2 = \frac{2\ \pi\ D_{2,m}}{Z_{blades}} + 2b_2 \tag{5.30}$$

$$p_1 = \frac{\pi\ D_{1,hub} + \pi\ D_{1,tip}}{Z_{blades}} + 2b_1 \tag{5.31}$$

$$c_d = (c_f + 0.001)(1 + 4\frac{b_1}{D_{2,m}}) \tag{5.32}$$

With respect to the Gülich's approach, the current model introduces new hydraulic parameters, which allow a better prediction of the turbine head under off-design operating conditions:

- Flow incidence losses at inlet section of the runner, $\zeta_{runner,2}$ (Fig. 5.15);

- Blade blockage factor that influences inlet velocity triangle, causing the contraction of the inlet cross-area, hence a loss due to the variation of the radial velocity component, $\zeta_{runner,3}$ (Fig. 5.15);
- The slip factor, $\sigma_{turbine}$, i.e., a parameter which depends on the difference between the actual tangential velocity and the theoretical flow tangential velocity at the outlet section of the runner.

This last parameter contemplates the influence of the flow deflection with respect to the blade congruent flow angle at the outlet of the runner during turbine mode operation. This deflection causes a reduction of the work due to the finite number of runner vanes, which are not able to guide perfectly the flow.

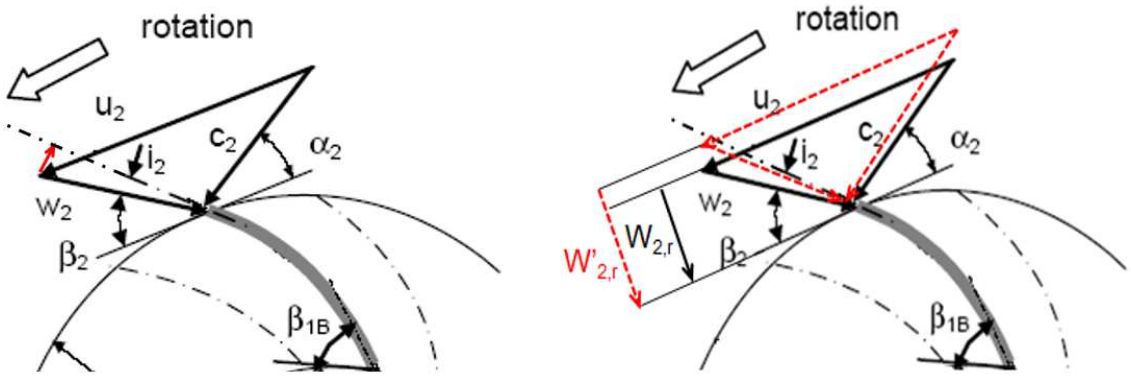

FIGURE 5.15: Runner losses: The flow incidence loss (left); Variation of the radial component of the inlet relative velocity (right).

5.3.4 Slip Factor

Similarly to centrifugal pumps, also in turbines with a limited number of vanes, as in the case of PaT, a slip phenomenon occurs at the outlet section of the runner. With regard to this aspect, there are few works in the literature, which have investigated in detail the effect of the slip phenomenon in PaTs. Indeed, the evaluation of the slip effect is difficult and there are not many experimental correlations.

Ventrone [46] focused on the slip effects at the outlet section of Francis turbines. He showed that Busemann's results, obtained for centrifugal flows into radial blade vanes, are also valid for a centripetal flow. In order to model this phenomenon, numerical simulations have been performed in collaboration with Capurso et al. [49], highlighting the flow deflection with respect to the blade congruent flow angle at the outlet of the runner during turbine mode operation. As shown in Fig. 5.16, this deflection involves the increase of the absolute tangential velocity component of the absolute velocity, c_{1u}, causing a decrease in terms of work done by the turbine.

The proposed model considers the slip factor, $\sigma_{turbine}$, i.e., the ratio between the real work here obtained by CFD, W_{CFD}, and the theoretical work, W_{th}, under the hypothesis with a perfectly guided flow.

$$\sigma_{turbine} = W_{CFD} / W_{th} \tag{5.33}$$

Capurso et al. [49] have correlated the slip factor, $\sigma_{turbine}$, with respect to the ratio between the flow rate, Q, and the flow rate at BEP in pump mode, $Q_{BEP,P}$, as stated in equation 5.34

$$\sigma_{turbine} = 0.2365\left(\frac{Q}{Q_{BEP,P}}\right)^2 - 0.5537\left(\frac{Q}{Q_{BEP,P}}\right) + 1.2846 \tag{5.34}$$

As results, the turbine head is lower than the theoretical head due to the increase of the circumferential component of the absolute velocity at the outlet section of the runner.

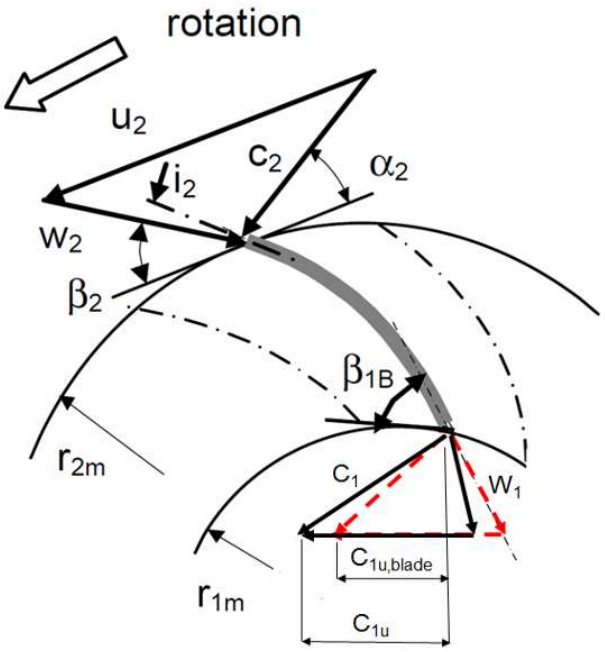

FIGURE 5.16: The slip phenomenon at the outlet section of the runner.

5.3.5 Results and Discussions

The proposed 1-D model has been compared with other models in terms of prediction of the characteristic curve for three different machine by Nuovo Pignone: two single stage double suction centrifugal pumps and one multistage centrifugal pump with 2 stages.

Single Stage Centrifugal Pump as Turbine ($N_{s,P} = 22$)

The proposed model for the prediction of the characteristic curve of a centrifugal pump operating as a turbine was applied to a double suction centrifugal pump of Nuovo Pignone ($N_{s,Pump} = 22$, $D_2 = 9.928''$). Fig. 5.17 shows a sketch of an example of the considered machine type.

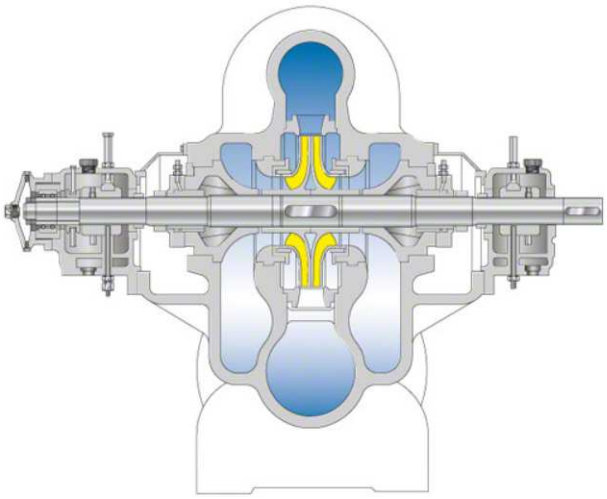

FIGURE 5.17: Example of a Double Suction Single Stage Centrifugal Pump [87].

Fig. 5.18 shows the comparison between the proposed model, the Gülich's model, the Derakshan's model and a previous model used by the manufacturer in the prediction of the characteristic curve during turbine mode.

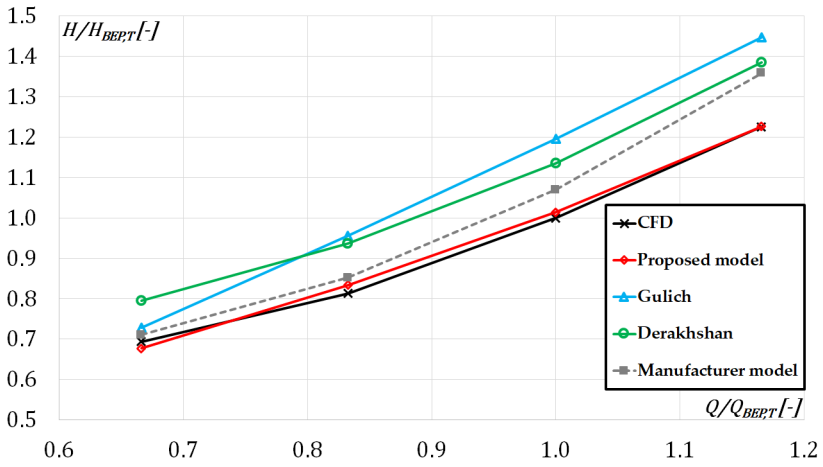

FIGURE 5.18: Comparison of different prediction models for the PaT characteristic curve.

All predicted curves have been compared with respect to that obtained by means of a numerical simulation performed by Capurso et al. [49]. As result, the use of detailed geometrical information, the introduction of a slip factor and a new modelling of the hydraulic losses have involved a more accurate prediction of the PaT performance under design and off-design conditions. Indeed, the proposed 1-D model shows the best prediction at the lowest and the highest flow rates (respectively equal to -2% and 0.1%) with respect to Derakshan's (respectively equal to 14.7% and 13.1%), Gülich's models (respectively equal to 5% and 18%) and to the previous model by manufacturer (respectively equal to 2.4% and 11%), as indicated in Tab. 5.4.

TABLE 5.4: Comparison of different prediction models for PaT characteristic curve in terms of head prediction errors.

$Q/Q_{BEP,T}$	**0.67**	**0.82**	**1**	**1.17**
Gülich	5.0 %	17.5 %	19.7 %	18.1 %
Proposed model	−2.4 %	2.6 %	−1.5 %	0.1 %
Derakhshan	14.7 %	15.2 %	13.5 %	13.1 %
Manufacturer	2.4 %	4.8 %	7.0 %	11 %

Fig. 5.19 shows the contribution of the different hydraulic aspects introduced in the proposed model in order to predict the characteristic curve obtained by CFD. The introduction of volute and runner losses causes an increasing of the turbine head, whereas the slip factor decreases the theoretical work calculated by means of Euler's equation and thus, involves a better prediction for the different operating points. Furthermore, the flow incidence loss and the variation of the radial component of the relative inlet velocity show their remarkable contribution at lower flow rate.

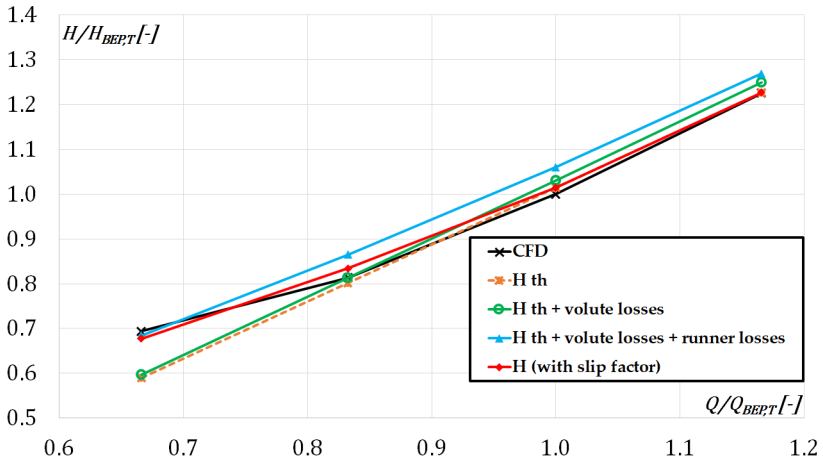

FIGURE 5.19: Comparison of different sources of losses for the performance prediction.

Moreover, three different slip factor definitions have been applied to the 1-D model, as depicted in Fig. 5.20. The results show that the model with the assumption that the slip factor term is negligible ($\sigma_{turbine} = 1$), overestimates the turbine head at the BEP with an error of $+6.4$ %. On the other hand both the Busemann [88] and Stodola [89] formulations applied to the 1-D model provide good results at the BEP, but underestimate the turbine head at the part-loads, with an error of -8 %. The application of the slip factor, as described in Fig. 5.18, tends to minimize the errors over a wide range of flow rate.

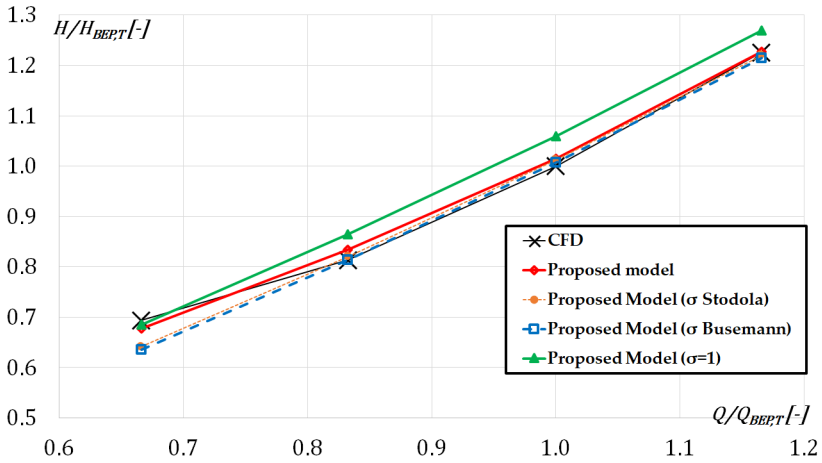

FIGURE 5.20: Comparison of different slip factor definitions (i.e., $\sigma_{turbine}$, σ proposed by Busemann, σ proposed by Stodola and $\sigma_{turbine} = 1$) with the CFD results.

Single Stage Centrifugal Pump as Turbine ($N_{s,P} = 26.46$)

The model has been applied to another machine that has been tested in both modes by Nuovo Pignone ($N_{s,Pump} = 26.46$, $D_2 = 17''$). For this machine, slip factor was evaluated by means of equation 5.34 because of the same number of blades and similar blade angles. Fig. 5.21 shows the comparison between the proposed model and the Derakshan's model in the prediction of the experimental characteristic curve. In this case, Gülich's model is not depicted because it overestimates the head much more than other models, whereas the previous home-made manufacturer model perfectly predicts the curve. Tab. 5.5 reports the head prediction errors for different flow rates in order to highlight the good prediction at off-design operating points.

TABLE 5.5: Comparison of different prediction models for PaT characteristic curve in terms of head prediction errors

$Q/Q_{BEP,T}$	**0.79**	**0.87**	**0.93**	**1**	**1.03**
Proposed model	2.9 %	0.6 %	−1.5 %	−2.9 %	−3.7 %
Derakhshan	18.6 %	13.2 %	9.3 %	6.8 %	5.8 %

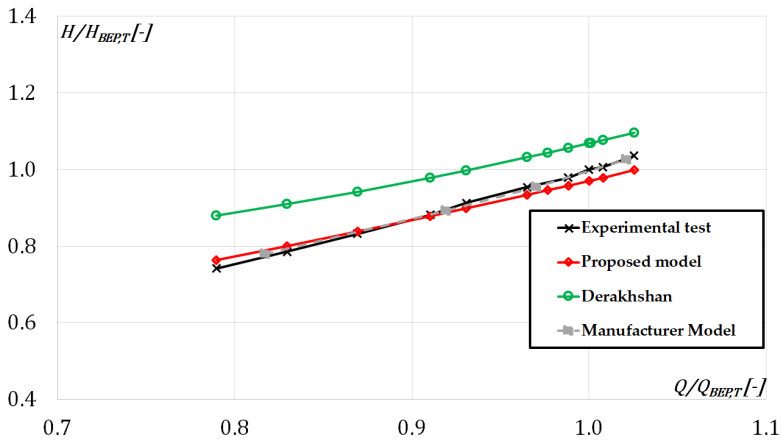

FIGURE 5.21: Comparison of different prediction models for the PaT characteristic curve.

2-stages centrifugal pump as turbine ($N_{s,P} = 28.12$)

In order to test the general applicability of the model, a 2-stages centrifugal pump by Nuovo Pignone has been used as the last case study. This machine ($N_{s,P} = 28.12$) has been tested by Nuovo Pignone in direct and reverse mode. In order to predict its performance in turbine mode, the model has been modified because of the presence of two different stages. Indeed, in multistage centrifugal pumps stages are connected to each other by means of crossover, i.e. inter-stage channels, whose geometry is quite complicated. The first stage is characterized by a double suction back-to-back impeller with double volute, whereas the second stage is a single suction impeller with double volute. Fig. 5.22 shows a sketch of an example of the considered machine type.

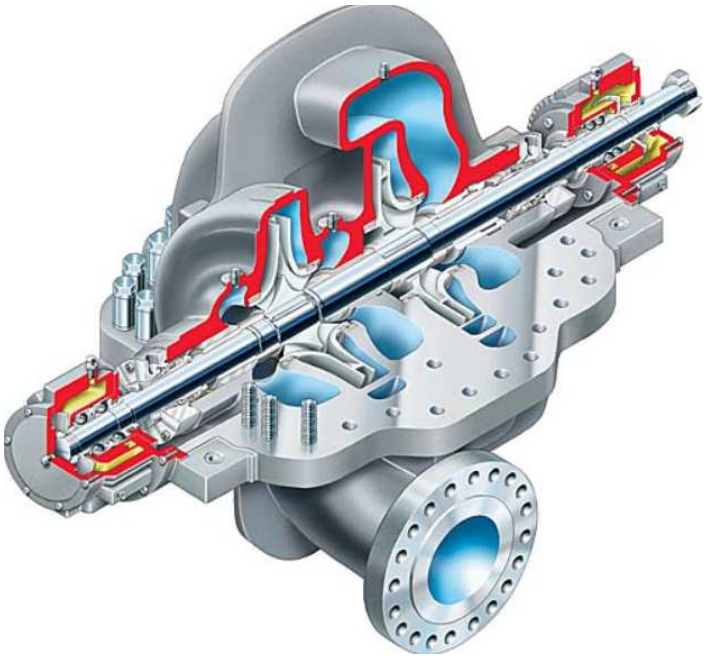

FIGURE 5.22: Example of a Two-stages Centrifugal Pump [90].

The model, described in the previous section, has been modified for multistage machines in order to take into account the head loss in the inter-stage channel. Obviously, in reverse mode, the flow rate crosses the machine by entering from the last stage of the pump (the first in turbine mode) and coming out from the first stage of the pump (the second in turbine mode). The crossover has been assumed to be such as a U-shaped channel, which connects the runner outlet section of the first stage (turbine mode) to the volute throat area of the second stage (turbine mode). For this reason, in the volute loss calculation of the second stage, the head loss in the inlet convergent nozzle is substituted by the head loss in the crossover with this assumptions:

- $c_{inlet} = c_1^{(1^{st}stage)}$;
- $c_{outlet} = c_3^{(2^{nd}stage)}$.

This head loss coefficient in the crossover is constituted by summing up the friction loss coefficient, $\zeta_{f,crossover}$, and the local loss coefficient, $\zeta_{L,crossover}$, due to two elbow bends with the assumption of U-shaped channel.

$$\zeta_{crossover} = \zeta_{f,crossover} + \zeta_{L,crossover} \tag{5.35}$$

where $\zeta_{f,crossover}$ and $\zeta_{L,crossover}$ are calculated by means of equation 5.36 and equation 5.37 respectively.

$$\zeta_{f,crossover} = f \frac{L_{crossover}}{D_{h,crossover}} \left(\frac{\bar{c}_{crossover}}{u_2} \right)^2 \tag{5.36}$$

$$\zeta_{L,crossover} = \xi_{bends} \left(\frac{\bar{c}_{crossover}}{u_2} \right)^2 \tag{5.37}$$

In equation 5.36, $\bar{c}_{crossover}$, $L_{crossover}$, $D_{h,crossover}$ are mean velocity, length and hydraulic diameter of the inter-stage channel, whereas f is the friction coefficient that depends on the Reynolds number and the relative roughness of the volute.

$$f = \frac{0.31}{\left[\log \left(0.135 \frac{\epsilon_{vol}}{D_{h,crossover}} + \frac{6.5}{Re_{crossover}} \right) \right]^2} \tag{5.38}$$

with:

$$\bar{c}_{crossover} = (c_{inlet} + c_{outlet})/2 \tag{5.39}$$

$$Re_{crossover} = \frac{\bar{c}_{crossover} \, D_{h,crossover}}{\nu} \tag{5.40}$$

In equation 5.37, ξ_{bends} is a loss coefficient, which contemplates losses due to the two elbow bends in the inter-stage channel.

Moreover, the number of blades, Z_{blades}, the outlet diameter, $D_{1,m}$, and the outlet blade angle, $\beta_{1,B}$, are different with respect the those of the first machine. For this reason, the slip factor for each of both runners was not evaluated by means of the correlation proposed by Capurso et al. [49] (equation 5.34) but with the Stodola equation.

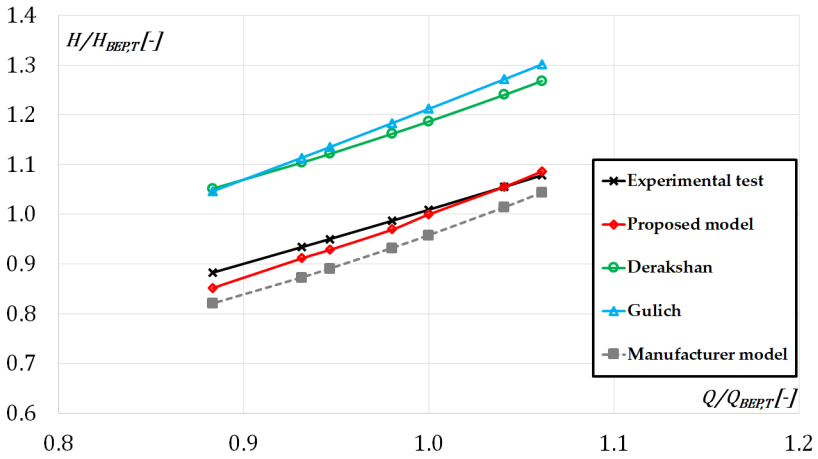

FIGURE 5.23: Comparison of different prediction models for the PaT characteristic curve.

Fig. 5.23 shows the comparison between the proposed model, the Gülich's model, the Derakshan's model and a previous model used by the manufacturer in the prediction of the characteristic curve during turbine mode.

All predicted curves have been compared with respect to the experimental one. As result, the use of detailed geometrical information, the introduction of a slip factor and a new modeling of the hydraulic losses have involved a more accurate prediction of the PaT performance under design and off-design conditions. Indeed, the proposed 1-D model shows the best prediction at the lowest and the highest flow rate (respectively equal to -0.7% and 3.5%) with respect to Derakshan's (respectively equal to 16.7% and 23.4%), to Gülich's models (respectively equal to 19.8% and 22.7%) and to the previous model by manufacturer (respectively equal to -3.3% and -7%), as indicated in Tab. 5.6.

TABLE 5.6: Comparison of different prediction models for PaT characteristic curve in terms of head prediction errors.

$Q/Q_{BEP,T}$	**0.88**	**0.95**	**1**	**1.06**
Gülich	22.8 %	22.2 %	21.2 %	19.8 %
Proposed model	3.50 %	2.30 %	0.92 %	-0.7 %
Derakhshan	23.4 %	20.8 %	18.7 %	16.7 %
Manufacturer	-7.0 %	-6.3 %	-5.1 %	-3.3 %

Chapter 6

Real Case Study of PaT Application

In this chapter a preliminary assessment about the installation of a PaT in a real case study has been conducted. The case study analyzed in this work is the town of Casamassima (BA), located in Puglia (Southern Italy). This work has been carried out in collaboration with the Department of Civil, Environmental, Land, Construction and Chemistry (DICATECh) of the Polytechnic University of Bari.

The experimental characteristic curves of the KSB PaT (showed in in Chapter 4) have been exploited for this work. Then, starting from the analysis of the pressure and flow rate patterns during the day and the night, three installation cases have been evaluated and compared in terms of hydraulic energy harvesting and power output useful to supply an electrical charging station: Case # 1) the installation of two different PaTs (the first works at its BEP during the day, whereas the second works at its BEP during the night); Case # 2) the installation of two identical PaTs: the first works alone during the night and the second works in parallel to the first during the day; Case # 3) the installation of only one PaT, which works during the day and the night. Part of this chapter is already published in [91]

6.1 The Case Study

In this study a real WDN is selected for an interesting application of a PaT for energy recovery which otherwise would be dissipated by means of PRVs. The town analyzed is Casamassima (BA) with 19,860 inhabitants, located in Puglia (Southern Italy), which is supplied by a unique tank. The WDN is subdivided into three DMAs thanks to pressure reduction valves, which permit to disconnect a DMA from another (Fig. 6.1). For the sake of clarity, two pressure reduction valves (PRV2 and PRV3) are installed at the entrance of the city, though downstream the tank, with the aim to subdivide the water network into two DMAs (DIS2 and DIS3). Moreover, one more DMA is located in cascade to DIS2 that supplies several residential buildings and a large golf course (DIS1). In the following analysis, DIS1 has been neglected, due to limited inhabitants. In a recent work, Balacco et al. [21] have reported flow rate values and pressure patterns measured downstream the tank (TANK) and downstream the two PRVs (DIS2 and DIS3), which are respectively depicted in Fig. 6.2 and Fig. 6.3. It can be observed how the two PRVs are set differently because of the different elevation of each DMA and, moreover, each of them is configured according to two different pressure patterns (daily and nightly) to guarantee firstly the necessary pressure level satisfying daily water demand and latter to reduce nightly leaks.

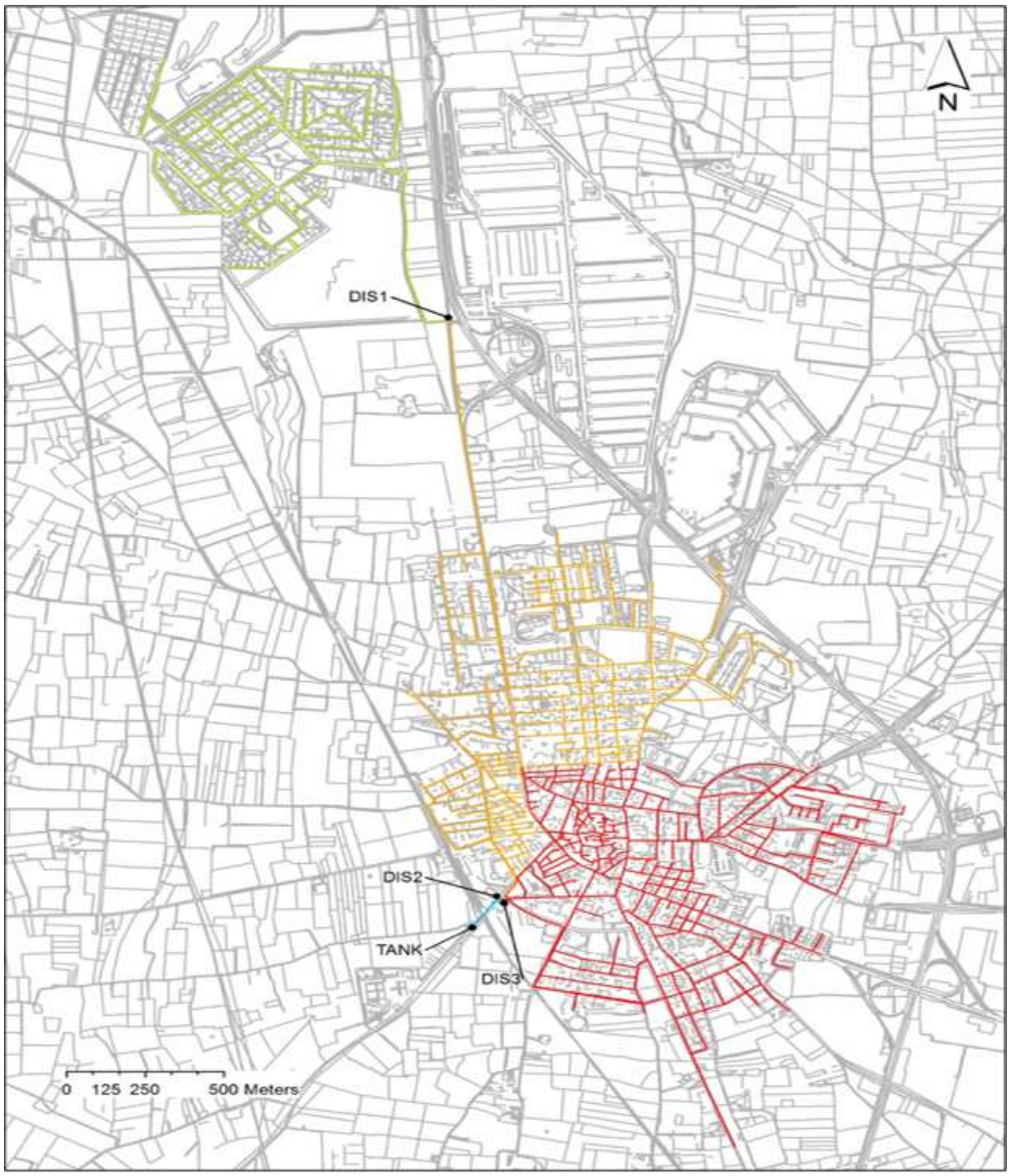

FIGURE 6.1: Water Distribution Network of Casamassima WDN, Italy, used as case study.

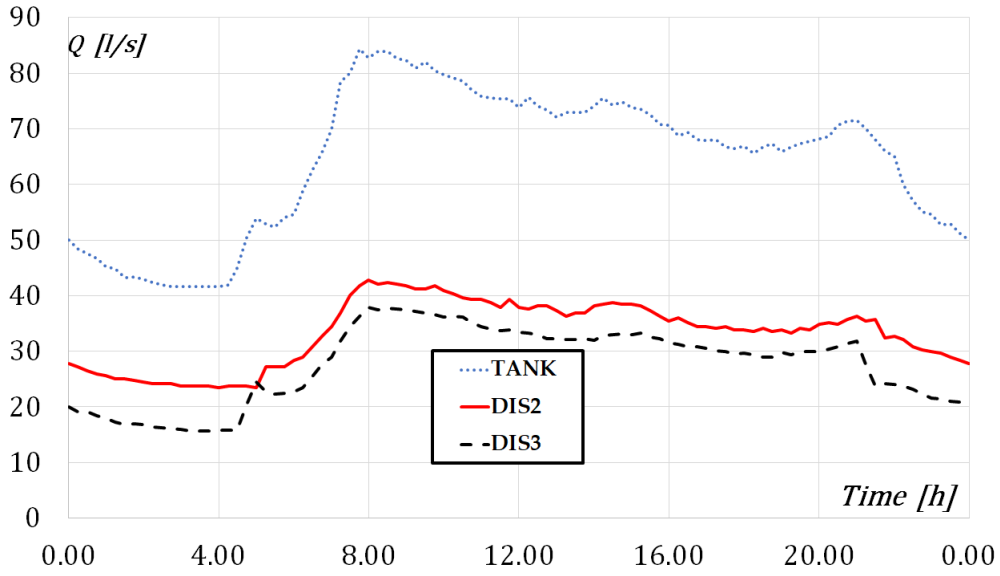

FIGURE 6.2: Flow rate measured for the three selected points (TANK, DIS2 and DIS3).

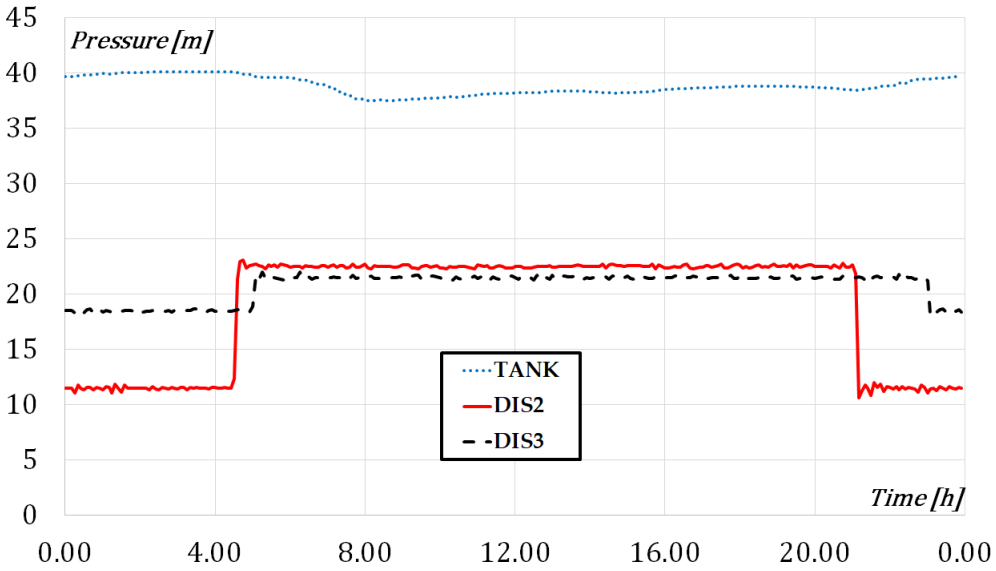

FIGURE 6.3: Pressure patterns measured downstream the TANK and the PRvs of DIS2 and DIS3.

6.2 Preliminary Technical Assessment

In order to evaluate what kind of machine can be more suitable for the case study, it is important to evaluate the required specific speed of the site (equal to the turbine specific speed, $N_{s,T}$) at the minimum and the maximum flow rate conditions, $N_{s,T}(Q_{min})$ and $N_{s,T}(Q_{max})$. By considering a rotational speed equal to 1500 rpm, the required specific speeds at the minimum and the maximum flow rate are respectively equal to 19.74 and 36.85. Once these two values are known, it is possible to evaluate the specific speed that the machine should have in pump mode by means of the correlation proposed in this work (Chapter 5):

$$N_{s,P} = (N_{s,T} + 2.6588)/0.9237 \tag{6.1}$$

According to equation 6.1, the pump specific speed at the minimum and maximum flow rate are respectively $N_{s,P}(Q_{min}) = 24.2$ and $N_{s,P}(Q_{max}) = 42.8$, which are within the conventional range of applicability of centrifugal pumps, showed in Fig. 6.4. As first step, the KSB Etanorm 200-150-400 PaT ($N_{s,T} = 22.06$ and $D_2 = 419\ mm$) has been chosen for the case study. This machine has been tested and showed in Chapter 4). Fig. 6.5 shows the required operating points at the minimum and the maximum flow rate, which are plotted on the PaT performances curves. Unfortunately, both the points are out of the PaT operating range, defined by the runway and the blocked rotor curve.

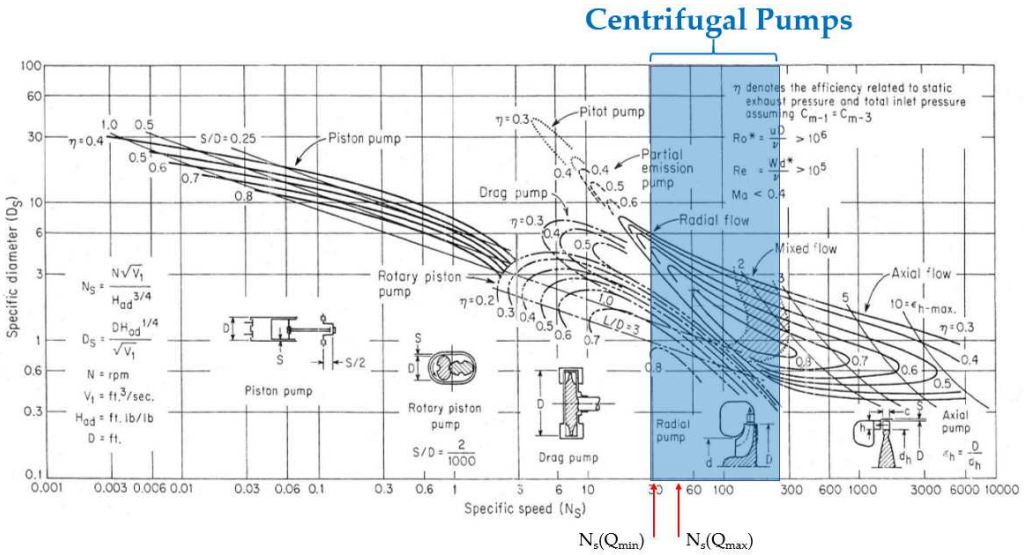

FIGURE 6.4: Pump selection chart [92].

In order to guarantee the required operating points of the water distribution network of Casamassima, it is possible to scale the PaT performance by means of the outer diameter D_2 and rotational speed, N, as stated in equation 6.2 and 6.3 (where $D_{2,ref} = 419\ mm$ and H_{BEP}^{test} and Q_{BEP}^{test} are respectively the experimental head and flow rate evaluated at the rotational speed Nref at the BEP condition.

$$Q = \left[Q_{BEP}^{test} \left(\frac{D_2}{D_{2,ref}} \right)^3 \right] \left(\frac{N}{N_{ref}} \right) \tag{6.2}$$

$$H = \left[H_{BEP}^{test} \left(\frac{D_2}{D_{2,ref}} \right)^2 \right] \left(\frac{N}{N_{ref}} \right)^2 \tag{6.3}$$

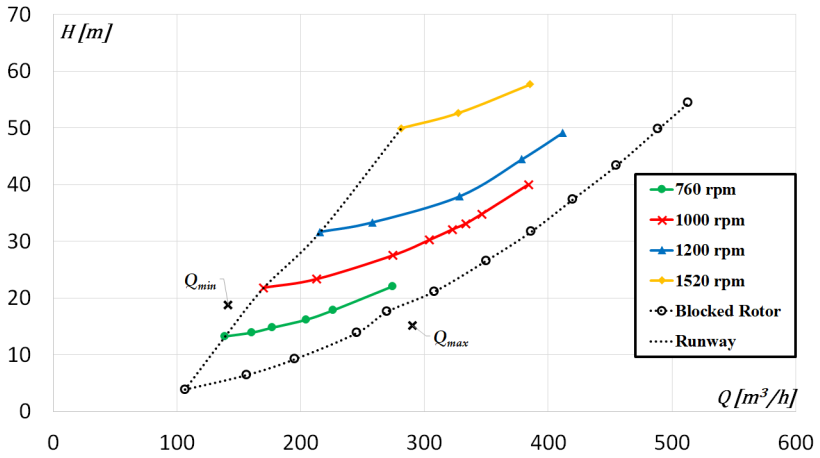

FIGURE 6.5: Minimum and maximum operating conditions in WDN of Casamassima plotted on experimental performance chart of the PaT KSB.

In order to select the design variables (Q and H) to be used, a statistical analysis has been performed for each pattern of operating conditions. The flow rates acquired during the night pattern (23:05 – 4:30) show a mean value $\overline{Q}_{night} = 155.2\ m^3/h$ with a standard deviation $\sigma_{night} = 14.38\ m^3/h$, whereas the day pattern (04:35 – 23:00) is characterized by a mean value $\overline{Q}_{day} = 239.4\ m^3/h$ with a standard deviation $\sigma_{day} = 31.21\ m^3/h$. Fig. 6.6 and 6.7 depict the flow rate frequency distributions, f_Q, and the cumulative available hydraulic power, P_{Hydr}, during the night (Fig. 6.6) and the day (Fig. 6.7). Both of them present the mean values in the range with the highest frequency and the highest available hydraulic power. For this reason, two operative conditions have been chosen: PaT has to work at the BEP with $\overline{Q}_{night} = 155.2\ m^3/h$ and $H_{night} = 19\ m$ during the night, whereas with $\overline{Q}_{day} = 239.4\ m^3/h$ and $H_{day} = 15\ m$ during the day.

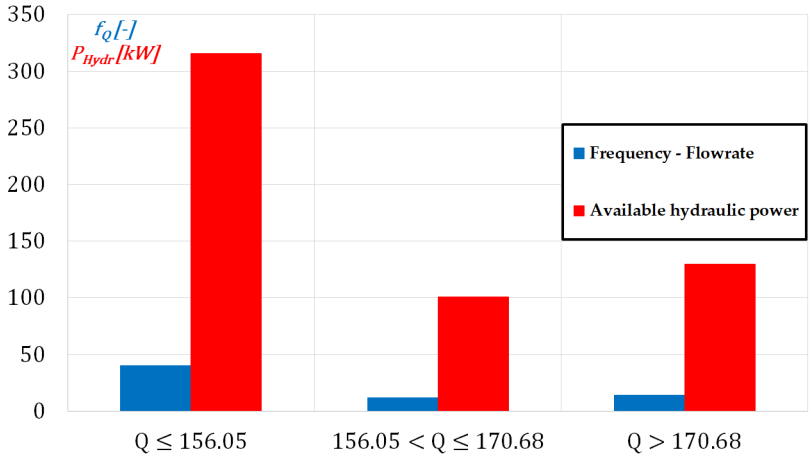

FIGURE 6.6: Flowrate frequency distribution and cumulative available hydraulic power during the night pattern.

Once the operative conditions have been set, it is possible to scale the experimental characteristic by applying equation 6.2 and 6.3 in order to find the new diameter and the new rotation speed, which guarantee the BEP at the selected operating points. As results, a PaT (PaT # 1) with $D_2 = 328.2\ mm$ and $N = 967.5\ rpm$ is required during the night, whereas a second PaT (PaT # 2) with $D_2 = 432.7\ mm$

and $N = 651.9\ rpm$ is required. Considering the wide range of flow rates, three installation cases have been evaluated and compared in terms of hydraulic energy harvesting and power output useful to supply an electrical charging station.

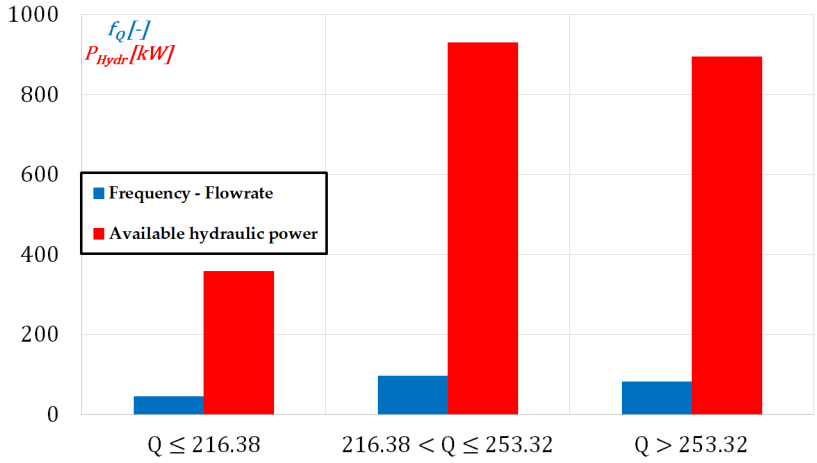

FIGURE 6.7: Flowrate frequency distribution and cumulative available hydraulic power during the daily pattern.

6.2.1 Case 1

Fig. 6.8 shows the layout with PaT # 1 and PaT # 2 installed in parallel. In order to allow the hydraulic regulation, a PRV is installed in series to each PaT and a by-pass line is contemplated in parallel to the entire PaT system. In this case, it is supposed that PaT # 1 works during the night, whereas PaT # 2 during the day. Fig. 6.9 shows the characteristic curve of PaT # 1 and the site characteristic with their intersection at the BEP of the machine, highlighted in red ($\overline{Q}_{night} = 155.2\ m^3/h$ and $H_{night} = 19\ m$). A by-pass line is used when the flow rate exceeds the mean value, $\overline{Q}$. This solution allows the turbine to work always at its BEP condition. Otherwise, for flow rate lower than the mean, the PRV # 1 is used to regulate the head. During the day PaT # 2 is turned on and works alone during all the daytime pattern. Fig. 6.10 shows the characteristic curve of PaT # 2 and the site characteristic during the day with their intersection at the BEP of the machine, highlighted in red ($\overline{Q}_{day} = 239.4\ m^3/h$ and $H_{day} = 15\ m$). The regulation is carried out by means of the by-pass line and the PRV # 2 with the same logic, as previously discussed.

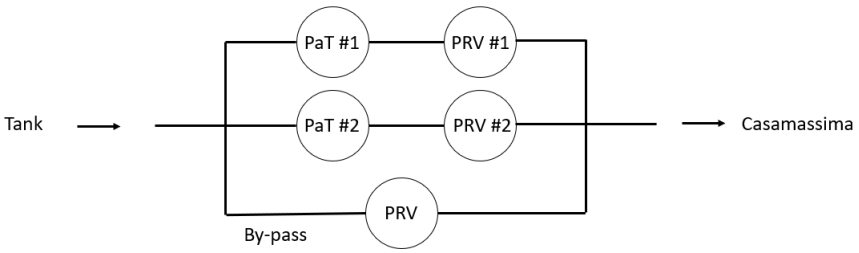

FIGURE 6.8: Installation layout of Case # 1.

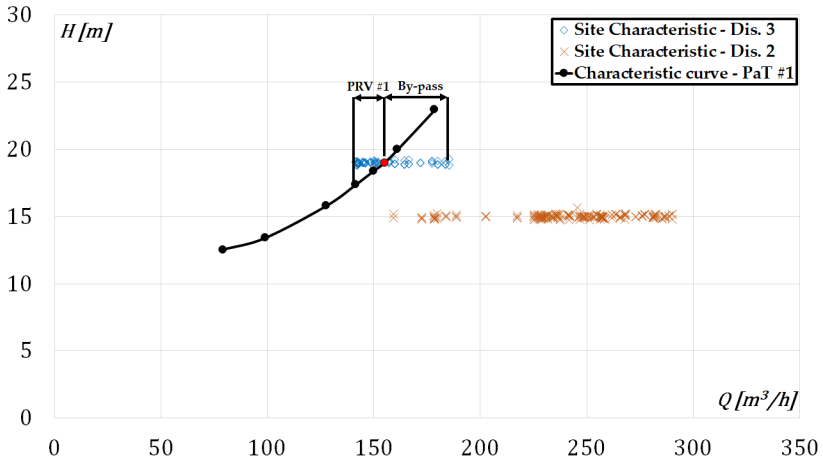

FIGURE 6.9: Site characteristic curves with characteristic curve of PaT # 1 during the night with regulation methods.

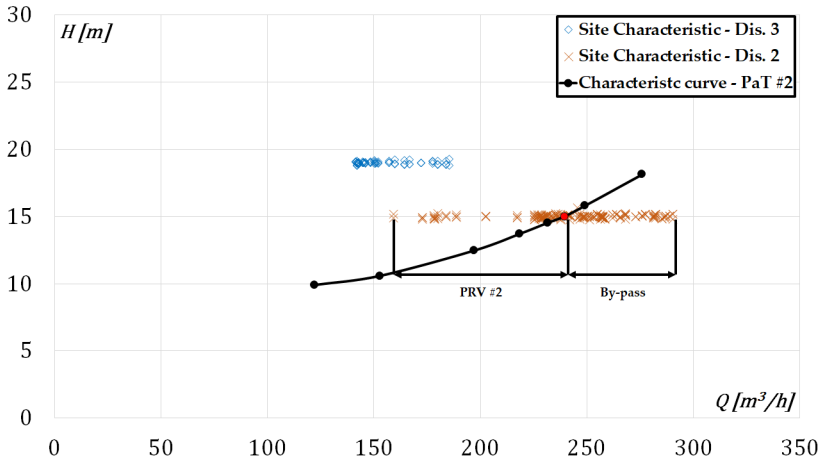

FIGURE 6.10: Site characteristic curves with characteristic curve of PaT # 2 during the day with regulation methods.

6.2.2 Case 2

Fig. 6.11 shows the layout with two identical PaTs # 1 installed in parallel. In order to allow the hydraulic regulation, two identical PRVs are installed (one for each PaT) and a by-pass line is installed in parallel to the entire PaT system. In this case, it is supposed that only one machine works during the night, whereas both of them work in parallel during the day.

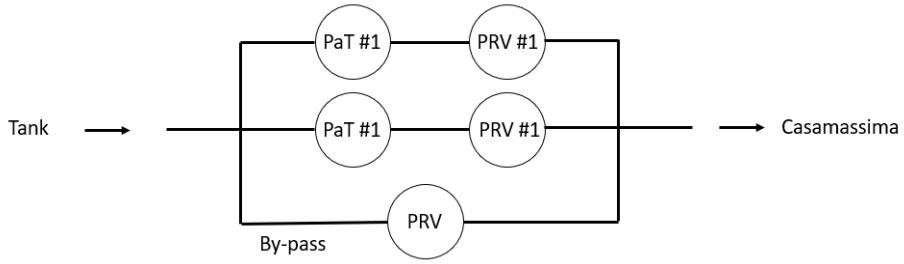

FIGURE 6.11: Installation layout of Case # 2.

Fig. 6.12 shows the characteristic curve of two PaT # 1 in parallel and the site characteristic. During the day, three types of regulation are considered: the by-pass line is used for flow rates greater than the operating point; both the PRVs operate for flow rates lower than the operating point; when operation points are close to the runway condition, the system is controlled by means of a speed regulation. The rotational speed is decreased in order to move the runway point towards lower flow rates. At this point, it is possible to use PRVs in order to regulate the head by dissipating the exceeding pressure (Fig. 6.13).

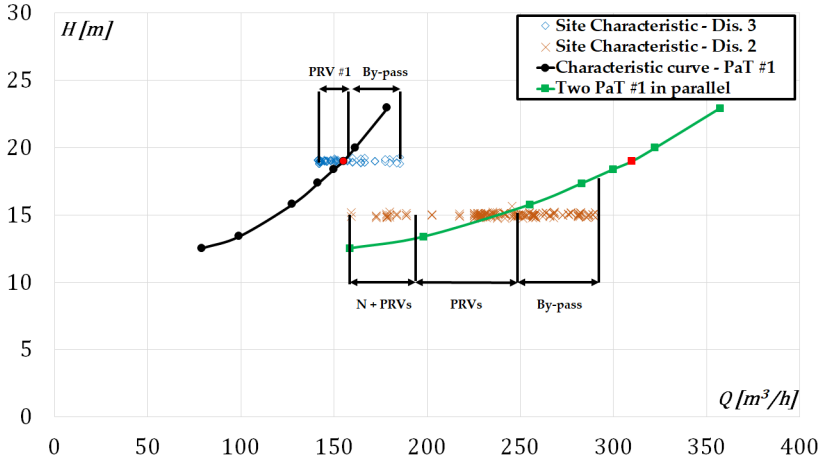

FIGURE 6.12: Characteristic curve of PaT # 1 during the night (in black) and characteristic curve of two PaT # 1 in parallel during the day (in green) with their regulation methods.

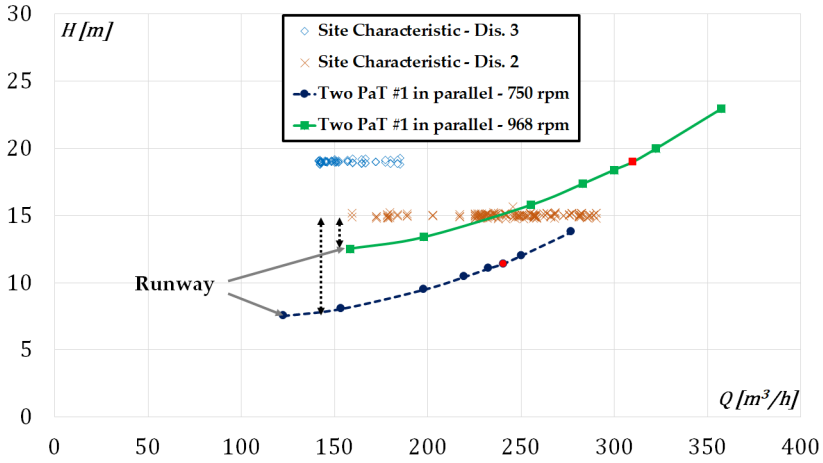

FIGURE 6.13: Particular of the speed regulation method during the day.

6.2.3 Case 3

A third case has been considered in order to simplify the system with only one machine, PaT # 3, one PRV and a by-pass line, as shown in Fig. 6.14.

The KSB PaT has been scaled in order to guarantee the mean flow rate required daily and nightly ($\overline{Q} = 219.55\ m^3/h$ and $\overline{H} = 15\ m$). As results, the machine requires $D_2 = 414.4\ mm$ and $N = 680.8\ rpm$. In this way, the by-pass line is used for all the

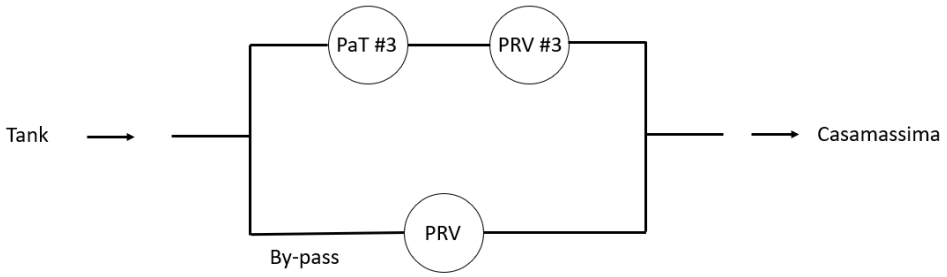

FIGURE 6.14: Installation layout of Case # 3.

flow rates greater than the BEP condition (highlighted in red), whereas a PRV can be used for flow rates lower than the BEP condition (Fig. 6.15). In order to guarantee a lower pressure drop during the hydraulic regulation in the night, it is possible to increase the rotational speed of the turbine (from 680.1 rpm to 750 rpm), as depicted in Fig. 6.16.

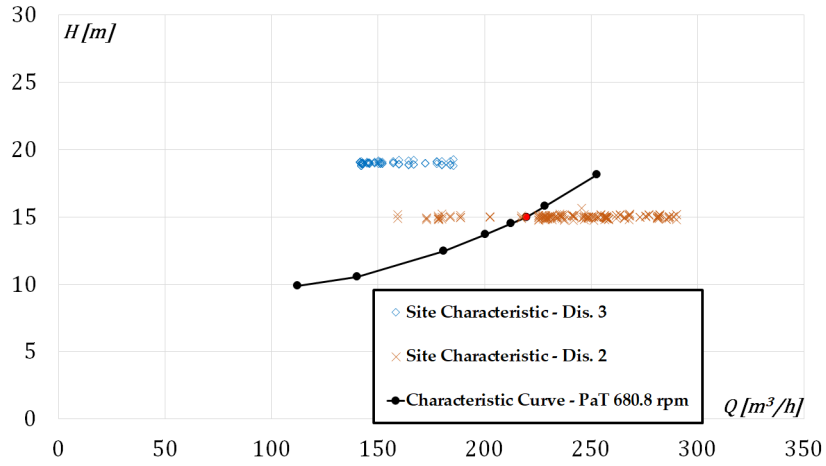

FIGURE 6.15: Characteristic curve of a single PaT during the day.

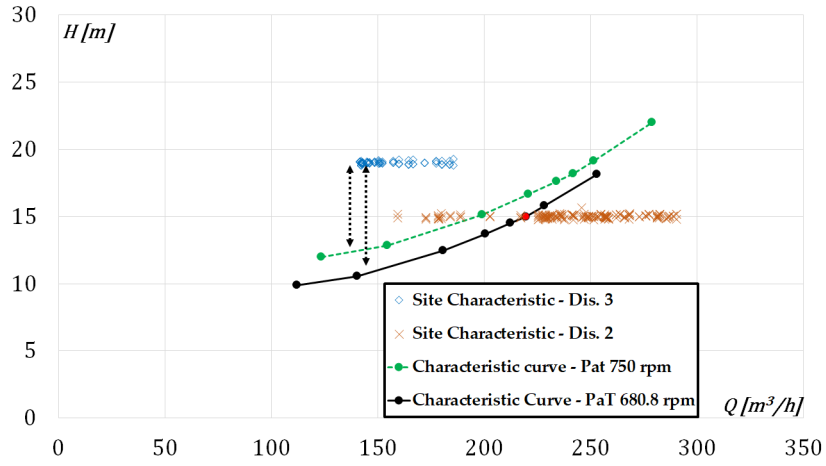

FIGURE 6.16: Characteristic curve of a single PaT during the night with its regulation methods.

6.3 Results and Discussion

In order to evaluate which solution can be more suitable for the case study, a Hydraulic Source Harvesting Coefficient has been introduced, C_P, as the ratio between the total hydraulic power obtained by the PaT and the total hydraulic power available from the site (equation 6.4).

$$C_P = \frac{\sum P_{Hydr}^{obt.}}{\sum P_{Hydr}^{available}} \tag{6.4}$$

Tab. 6.1 compares all the three solutions in terms of C_P. Case # 1 represents the best solution in terms of hydraulic energy harvesting because the two specific PaTs have been chosen in order to guarantee BEPs in different operating conditions, during the nightly and daily patterns. However, this solution can involve high costs in terms of the purchase of two different machines, three different PRVs and civil works. Case # 2 shows a decrease of 3 % of C_P in daily working condition. This is understandable because the intersection between the daily site characteristic and the characteristic in parallel is not at the BEP, as illustrated in the Case # 1. Although this decrease of C_P, this solution is more suitable with respect the first case in terms of costs because it requires the purchase of two identical machines and PRVs. Finally, Case # 3 shows a decrease of C_P in the night whereas a lower decrease in the day. Indeed, considering only one PaT, all the available energy in the night is no more exploitable because of the hydraulic regulation by means of the PRV. Despite of this reduction of C_P, this solution minimizes costs because it shows the simplest layout with one PaT, one PRV and the by-pass line.

TABLE 6.1: Comparison of the three proposed cases in terms of C_P.

ID Case	$C_P(Night)$	$C_P(Day)$
Case # 1	0.7621	0.8987
Case # 2	0.7621	0.8743
Case # 3	06842	0.8644

Fig. 6.17 and 6.18 show respectively the effective produced power during the day and the night for each proposed case ($P_{eff} = \eta_{PaT}\ P_{Hydr}^{obt.}$). The power required by the recharging point is a design constrain and it is equal to 3.7 kW. Case # 1 shows the highest power output during the day with the by-pass regulation because of the highest flowrate with a pressure drop as equal as to the other cases, whereas Case # 3 shows the highest power output with the pressure regulation by PRV. Moreover, during the night, Case # 1 and Case # 2 show the same power output because in both cases the same PaT works (PaT # 1). During all the night these two solutions presents power output greater than 3.7 kW. Case # 3, due to the head reduction with the PRV, shows a lower power output level than the Case # 1 and # 2 during the night. Moreover, some operating points are below the constrain of 3.7 kW and electric batteries could be used to store the surplus power obtained during all the other moments of the day. Although Case # 3 does not show the maximum power output, it represents a good compromise in terms of power generation and cost installation.

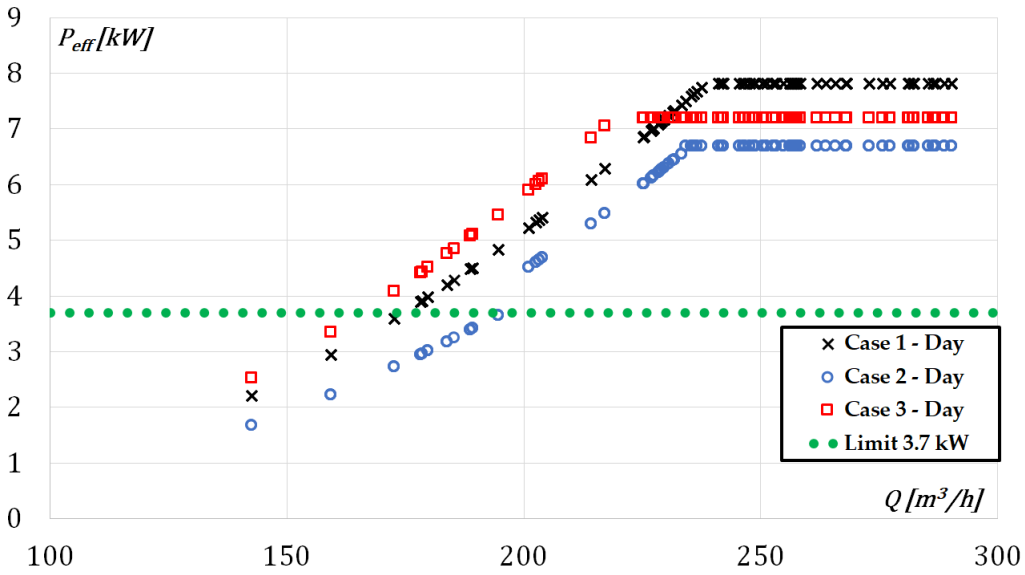

FIGURE 6.17: Comparison of the three proposed cases in terms of effective power output, P_{eff}, during the day. In green the power required by the electrical charging system.

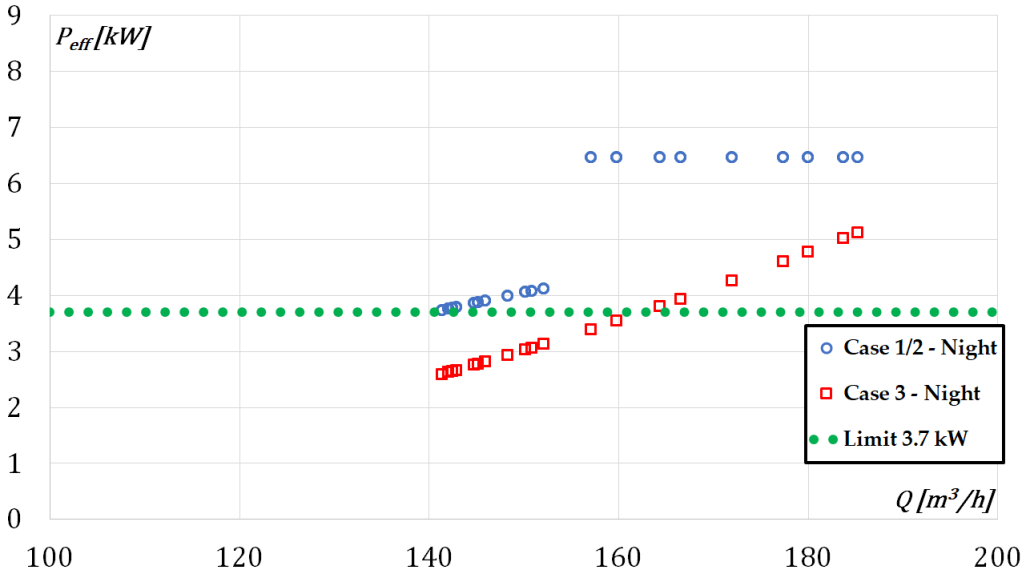

FIGURE 6.18: Comparison of the three proposed cases in terms of effective power output, P_{eff}, during the night. In green the power required by the electrical charging system.

Chapter 7

Multistage PaTs with Two-Phase Flow

PaTs can be used not only in hydraulics but also in chemical processes (gas washing plants, ammonia synthesis, reverse osmosis, mines cooling, oil supply systems). In these various chemical engineering processes, fluids containing dissolved or undissolved gases are expanded from a higher to a lower pressure level. If the energy released by this process is sufficiently large, it may be worthwhile to expand the fluid in a pump operating as a turbine. A two-phase flow is established in the turbine if the liquid fluid contains free gas and dissolved gases are released from the solution or part of the liquid evaporates during the expansion. As the gas contained in the fluid is expanded, additional energy is delivered with respect to the case of incompressible flow. This increase of power output is very interesting in terms of energy management improvement in process industries. Interest in pumps as turbines with two-phase flow dates back to the early 80's when the first technical reports on theoretical and experimental studies appear in literature. However, these models with simple assumptions show a limited applicability. In this chapter, a 6-stages centrifugal pump operating as turbine has been used as case study in order to develop a theoretical model, which could help in the prediction of the performance of a pump as turbine operating with two-phase flow, whose properties are known. Moreover, the fluid is considered with no vapour phase at the inlet section of the machine, whereas during the expansion both the mass vapor fraction, x, and the volume vapor fraction, α, can increase. Part of this chapter is already published in [93].

FIGURE 7.1: 3D drawing of a multistage centrifugal pump tipically used in the process engineering [94].

7.1 Multi-phase flows in turbomachinery

In many processing engineering fields, both pumps and turbines can deal with multiphase flows. Two general kind of multiphase flow can be identified, namely disperse flows and separated flows. Disperse flows consist of finite particles, drops or bubbles (the disperse phase) distributed in a connected volume of the continuous phase. On the other hand, separated flows consist of two or more continuous streams of different fluids separated by interfaces [95]. A persistent theme throughout the study of multiphase flows is the need to model and predict the detailed behavior of those flows and the phenomena that they manifest in turbomachines. The capability of a centrifugal pump to convey a two-phase mixture depends basically on whether gas and liquid form a homogeneous mixture or to what extent the two phases separate. Fine gas bubbles dispersed in a liquid can be considered as a quasi-homogeneous mixture. Moreover, there is some slip between the phases, which causes additional losses. Slip and losses due to exchange of momentum are much higher than in bubbly flow. With larger gas volume fractions, bubbly flow is no longer possible, since small bubbles tend to coalesce to form larger gas accumulations. Body forces in rotating runners are effective in determining the flow patterns, which have an impact on the energy transfer. Indeed, the fluid in the runner channel is subject to a strong Coriolis acceleration $\overline{a}_c = 2 \times \overline{\omega} \times \overline{w}$. The Coriolis force acts perpendicularly to the direction of the relative velocity of the liquid phase and a stratified flow develops if a sufficient amount of a gas is present. Flow pattern prediction and interpretation in an impeller with two-phase flow is more difficult than with single-phase flow and it is difficult to establish general rules. Indeed, pumps and turbines show different behaviors when two-phase flows occur. In pumps, Coriolis forces transport liquid to the pressure side, while buoyancy effects move the gas to the suction side of the blades of centrifugal impellers. Phase separating effects grow with increasing flow rate because the pressure gradient from the pressure to the suction side as well as the Coriolis acceleration become stronger with increasing of flow rate. With larger gas volume fractions bubbly flow is no longer possible, since small bubble tend to coalesce to form larger gas accumulations, which can cause the "gas-locked" condition, as depicted in Fig. 7.2. In addition, in radial pumps gas bubbles travel against a strong centrifugal pressure gradient towards the outlet. All of these aspects cause a deterioration of pump performance and the appearance of operating instabilities [96].

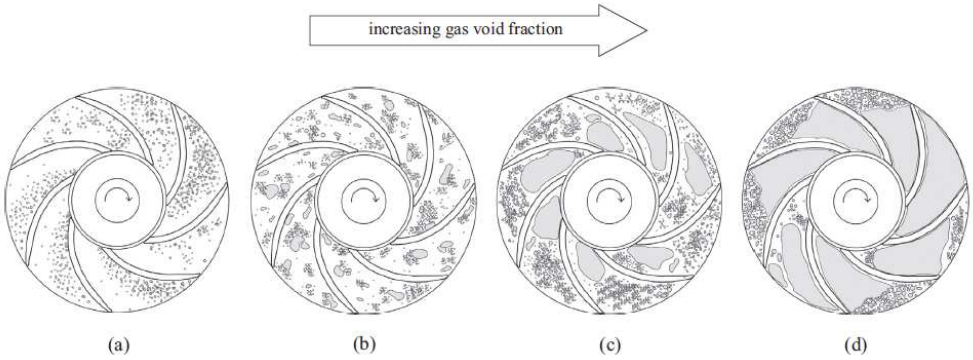

FIGURE 7.2: Two-phase flow patterns within centrifugal pumps impellers. (a) Bubble Flow, (b) Agglomerated Bubble Flow, (c) Gas Pocket Flow, (d) Segregated Flow [96].

Differently, in a turbine a pressure difference in the flow direction is established between the inlet and the exhaust nozzle. Consequently, the buoyancy effect tends to accelerate the gas in the direction of the flow, avoiding the gas-locking, even with high gas content. In most applications area, the fluid is subjected to high pressure drop and, for this reason, manufacturer propose to install multistage centrifugal pumps working as turbine in order to expand gradually the fluid and recovery energy. Fig. 7.3 shows three stages of a hypothetical PaT where the void fraction increases, hence also the flow rate, stage by stage. Apart from a possible Mach number limit, phase separation problems do not restrict the stable operation of a turbine: the gas is always blown through the machine, albeit with high losses and possibly little useful work.

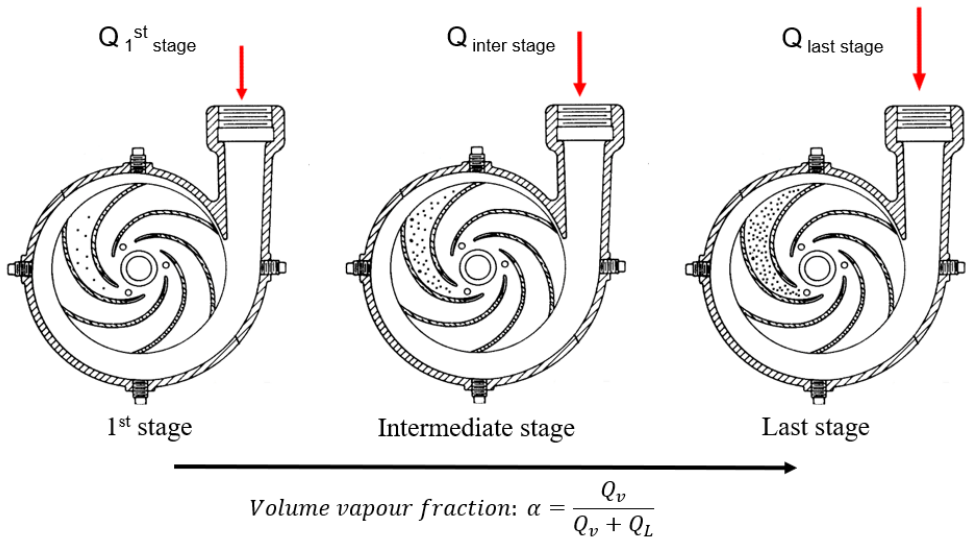

FIGURE 7.3: Example of increasing of the volume vapor fraction, α, during the expansion in a multi-stage PaT.

7.2 Proposed model

In order to design a two-phase flow multistage PaT, the manufacturer needs to know the available mass and volumetric flow rates, the power required, the flow properties ($x, \alpha, \rho_v^* = \rho_V/\rho_L$) at a reference temperature $T = T_{ref}$, the maximum and the minimum pressure of the process. Usually, manufacturing companies test their machines in single phase (generally water). Hence, in order to evaluate the behavior under two-phase flow, they need a global performance correction tool.

In this work, a multistage centrifugal pump with 6 equal stages was considered as case study. In Fig. 7.4 the characteristics of all the single stages are reported in terms of non-dimensional parameters, with the following assumption:

- $\eta_y^{(st)} = \eta_{y,T,1P}$
- $\varphi_{1P}^{(st)} = \varphi_{T,1P}$
- $\psi_{1P}^{(st)} = \psi_{T,1P}/N_{st}$

Moreover, Fig. 7.5 and Fig. 7.6 show flow properties (volume vapour fraction, α, non-dimensional vapor density, ρ_v^*, vapour mass fraction , x) as function of the

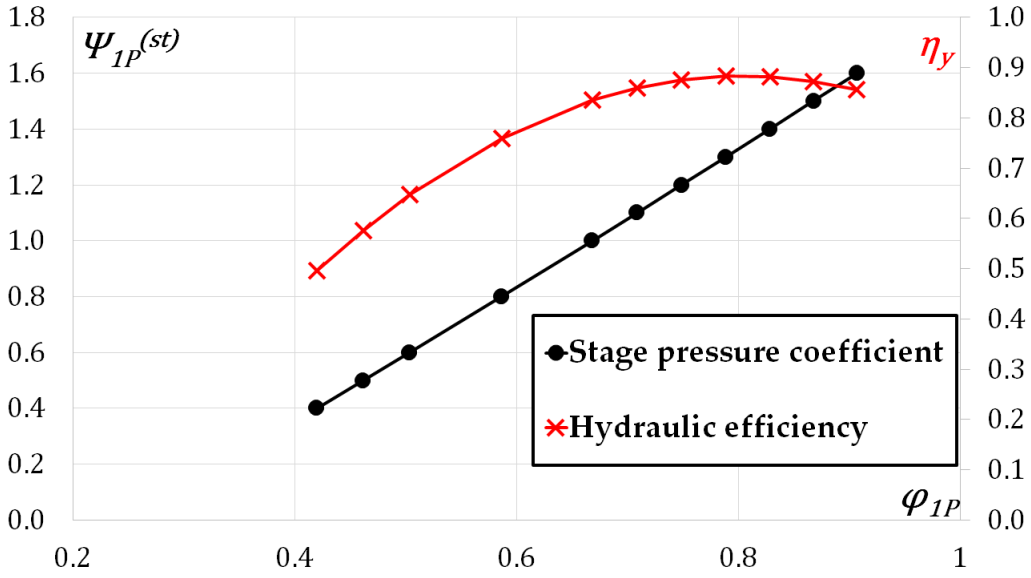

FIGURE 7.4: Experimental stage pressure coefficient, $\psi_{1P}^{(st)}$, and hydraulic efficiency, η_y vs. one-phase flow coefficient, φ_{1P} in turbine operation mode.

pressure during the expansion ($p_{ref} = 190\ bar$). Once the mass fraction, x, the liquid density, ρ_L, and the vapour density, ρ_V, are known it is possible to compute the vapour volume fraction, using equation 7.1.

$$\alpha = \frac{x\,\rho_L}{x\,\rho_L + (1-x)\,\rho_V} \tag{7.1}$$

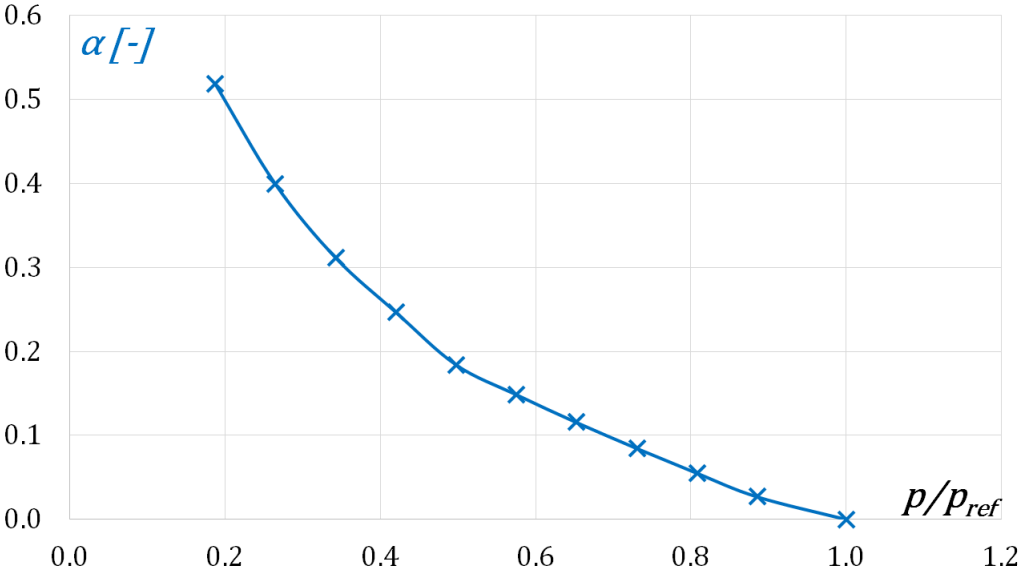

FIGURE 7.5: Values of the considered two-phase properties: volume vapor fraction, α, and vapor density vs. pressure.

The proposed model is based on the main hypothesis that the flow is homogeneous with a mean density of the mixture constant for each stage. Fig. 7.7 shows the algorithm of the proposed model. This calculation is performed simultaneously

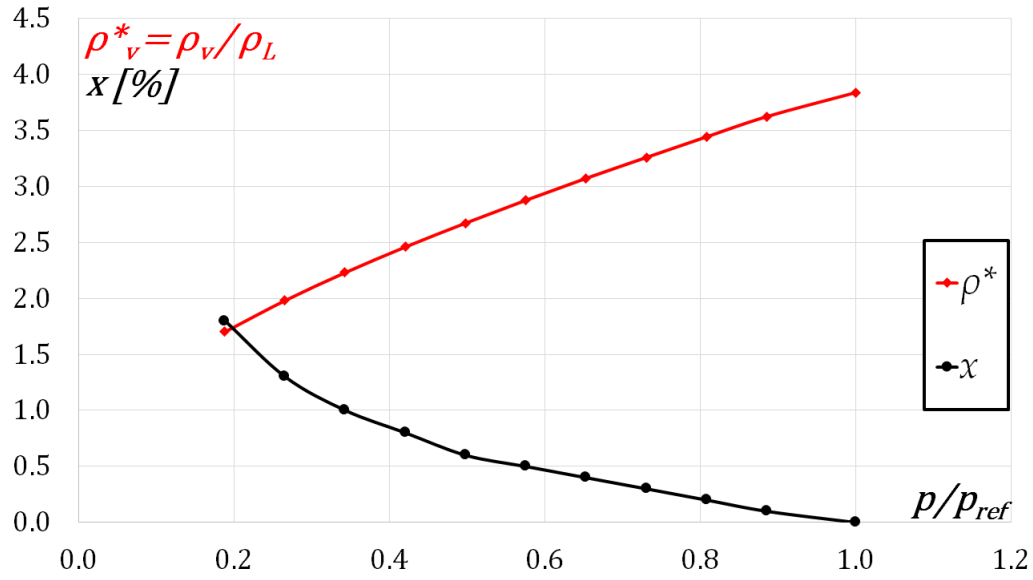

FIGURE 7.6: Values of the considered two-phase properties: mass vapor fraction, x, and non-dimensional vapor density, ρ_v^*, vs. pressure.

on each stage. The subscript 2 and 1 are respectively the inlet and the outlet sections of each stage. For initialization, the mass flow rate, G, is imposed and the turbine pressure drop, $\Delta p_T = (p_{in} - p_{out})$, is equally divided among each stage, $\Delta p^{(st)} = \Delta p_T / N_{st}$. The value of p_{out} is critical in order to avoid too high velocities. Although PaTs can handle significant vapour volume fractions, the proposed model can handle α lower than 50 %, otherwise bulk velocities become too high and comparable to sound speed. In such case, the hypothesis of incompressible flow across each stage is no more valid. This problem is particularly important in the last stage.

Once all the stage pressure drops $\Delta p^{(st)}$ are determined, $p_2^{(st)}$ and $p_1^{(st)}$ of each stage are known and it is possible to obtain from the correlation in Fig. 7.6 the vapour mass fraction, x, the vapour density, ρ_V, and the vapour volume fraction, α, at the inlet and outlet section of the stage ($x_2^{(st)}$, $x_1^{(st)}$, $\rho_{V,2}^{(st)}$, $\rho_{V,1}^{(st)}$, $\alpha_2^{(st)}$, $\alpha_1^{(st)}$). In order to compute the pressure levels across each turbine stage, the following conditions are imposed:

$$\begin{cases} p_2^{(1st)} = p_{in} \\ p_2^{(st)} = p_1^{(st-1)} \\ p_1^{(st)} = p_2^{(st)} - \Delta p^{(st)} \\ p_1^{(N_{st})} = p_{out} \end{cases} \tag{7.2}$$

Considering a homogeneous mixture, it is possible to calculate the mixture density at both inlet, $\rho_{mix,2}^{(st)}$, and outlet, $\rho_{mix,1}^{(st)}$, of each stage by means of equation 7.4

$$\rho_{mix,i}^{(st)} = (1 - \alpha_i^{(st)})\rho_L + \alpha_i^{(st)} \rho_{V,i}^{(st)} \quad \forall i = 1,2 \tag{7.3}$$

Under the hypothesis of relative low vapour volume fraction, α, the mean mixture density of the stage, $\rho_{mix}^{(st)}$, can be computed as the average of the two mixture densities.

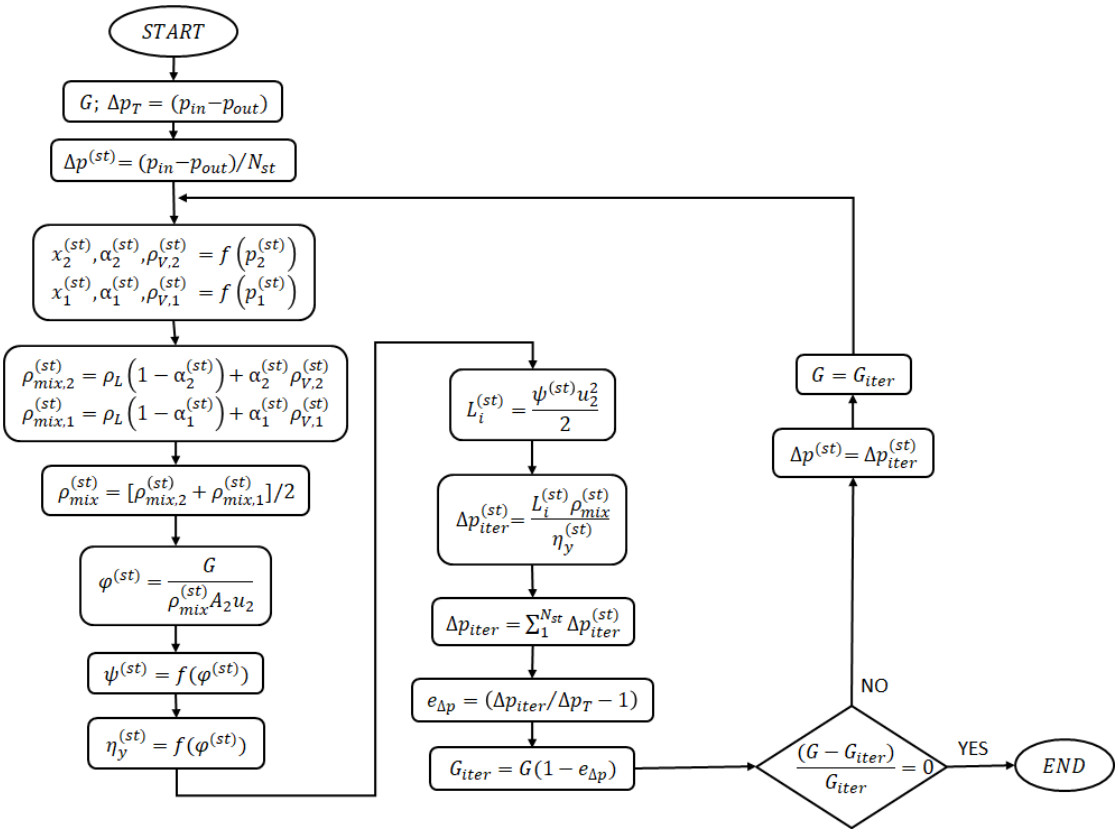

FIGURE 7.7: Flow chart of the proposed model.

$$\rho_{mix}^{(st)} = \frac{\rho_{mix,1}^{(st)} + \rho_{mix,2}^{(st)}}{2} \tag{7.4}$$

Knowing the mass flow rate, G, it is possible to calculate the flow coefficient, $\varphi^{(st)}$, as follows:

$$\varphi^{(st)} = \frac{G}{\rho_{mix}^{(st)}\ A_2\ u_2} \tag{7.5}$$

where A_2 and u_2 are respectively the cross section and the tangential velocity at the inlet of the runner.

Entering with $\varphi_{1P}^{(st)} = \varphi^{(st)}$ on the characteristic curves of Fig. 7.4, $\psi^{(st)} = f(\varphi^{(st)})$ and $\eta_y^{(st)} = f(\varphi^{(st)})$ are obtained.

At this point, it is possible to compute the new pressure drop for each stage:

$$\Delta p_{new}^{(st)} = \frac{L_i^{(st)}\ \rho_{mix}^{(st)}}{\eta_y^{(st)}} = \frac{\psi^{(st)}\ u_2^2\ \rho_{mix}^{(st)}}{2\ \eta_y^{(st)}} \tag{7.6}$$

Obviously, the new pressure distribution differs from the starting one and the mass flow rate need to be changed in order to satisfy the mass conservation across the entire PaT.

In the iterative process, in order to estimate the new mass flow rate, G_{new}, it has been supposed that the relative error on the pressure drop $e_{\Delta p} = (\Delta p_{new}/\Delta p_{old} - 1)$ is the opposite to the relative error on the mass flow rate G_{new} with respect to the starting mass flow rate G. This calculation is iterated until convergence of G.

7.3 Results and discussion

Fig. 7.8 and Fig. 7.9 show the comparison between the characteristic curve of the investigated 6-stages PaT under one phase operation and the predicted performance curves under two-phase flow for different pressure drops and different outlet pressure, in terms of turbine pressure coefficient, ψ_T, and the turbine power coefficient, $\lambda_T = 2P/(\rho_L\ A_2\ u_2^3)$. Each curve was obtained at constant rotational speed, N, constant outlet pressure, p_{out}, and by increasing the pressure upstream the turbine. These curves provide performance by varying the rotational speed and for similar PaTs in order to allow the manufacturer to scale its PaT according to different requirements. Pressure values were selected in order to guarantee that the flow coefficient in each stage remained within its operating range ($0.4 \leq \varphi \leq 0.9$, as depicted in Fig. 7.4). Indeed, the increase of the volumetric flow rate, when two-phase flows are considered, involves an increase of ψ_T and λ_T respectively of 40 % and 20 % on average. The minimum value of p_{out} is 35 *bar* (when p_{in} is 130 *bar*), otherwise the vapour volume fraction, α, becomes too high (greater than 50 %) and the flow coefficient of the last stage becomes higher that the upper allowable limit ($\varphi = 0.9$).

Fig. 7.8 and Fig. 7.9 point out that the reduction of the outlet pressure, p_{out}, causes two opposite effects: on one side, it involves a higher work output but, on the other side, a reduction of the operating range. In the case with $p_{out} = 60\ bar$, the maximum inlet pressure is $p_{in} = 190\ bar$. This means that the increase of the outlet pressure allows on an increase of the inlet pressure.

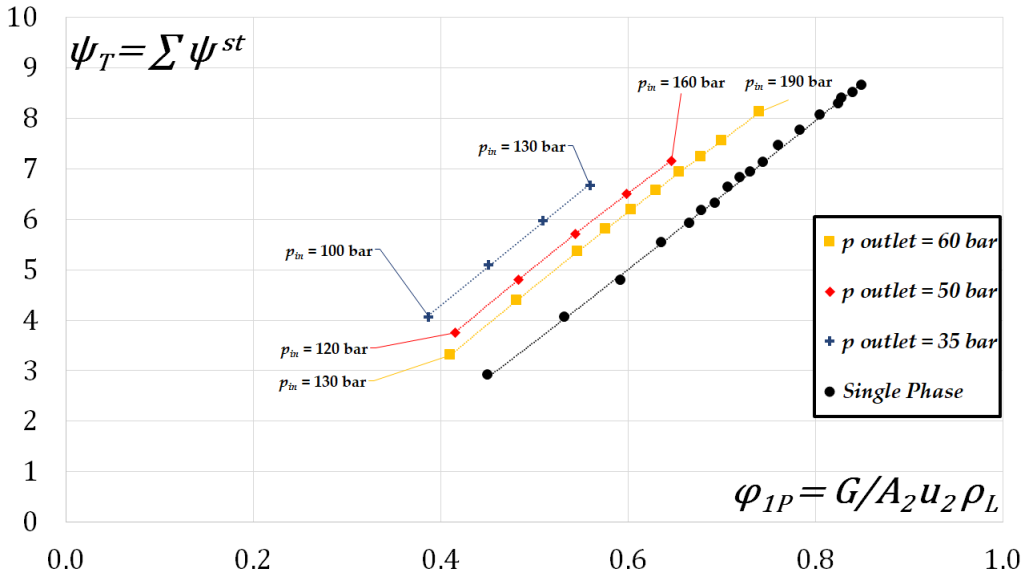

FIGURE 7.8: Comparison of the predicted performance curve with two-phase flow and the experimental curve with water in terms of pressure coefficient, ψ_T, vs. flow coefficient, φ_{1P}.

Fig. 7.10, Fig. 7.11 and Fig. 7.12 show how the operating points of each stage change during expansion. Three cases were compared at constant turbine pressure drop equal to 100 *bar*:

- $p_{in} = 160\ bar$ / $p_{out} = 60\ bar$ ($\alpha_{outlet} = 0.29$);
- $p_{in} = 150\ bar$ / $p_{out} = 50\ bar$ ($\alpha_{outlet} = 0.35$);
- $p_{in} = 100\ bar$ / $p_{out} = 30\ bar$ ($\alpha_{outlet} = 0.45$).

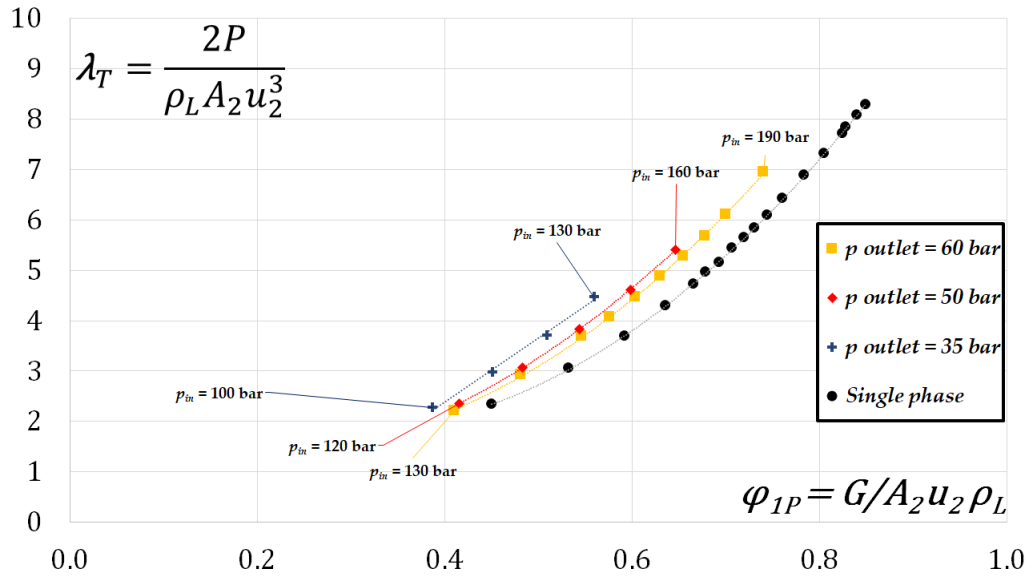

FIGURE 7.9: Comparison of the predicted performance curve with two-phase flow and the experimental curve with water in terms of power coefficient, λ, vs. flow coefficient, φ_{1P}.

During the expansion, the operating points of each stage, identified with $\psi^{(st)}$ and φ, remain on the non-dimensional characteristic of the machine and move towards higher flow coefficient and pressure coefficient, due to the decrease of the mean mixture density. Moreover, the effect of the increase of the volume vapor fraction is highlighted by the increase of the steps between two consecutive operating points from the first to the last stage. This aspect is strongly accentuated in the last case with the lowest pressure outlet, $p_{out} = 30\ bar$.

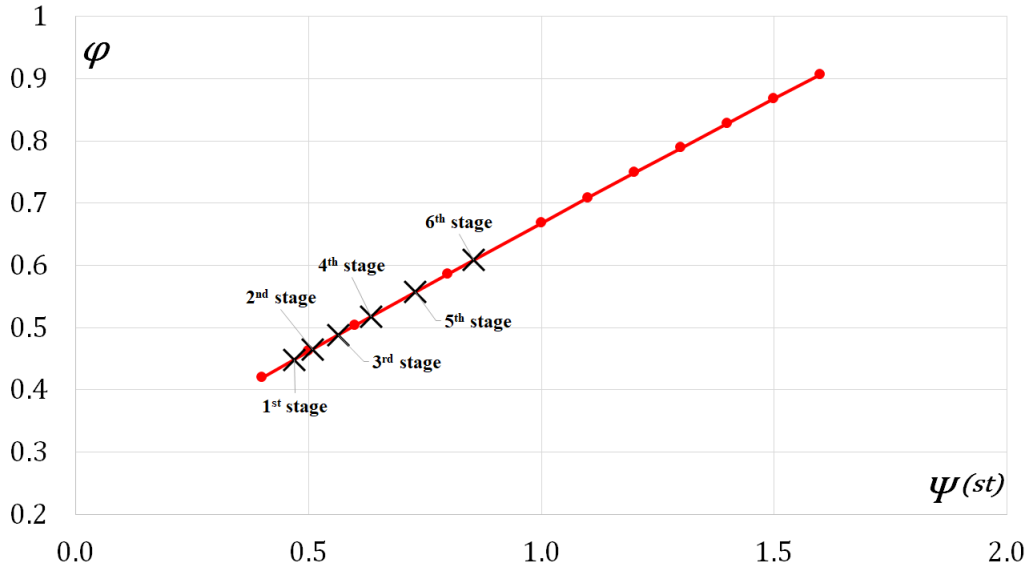

FIGURE 7.10: Change of operating points stage by stage ($p_{in} = 160\ bar$ and $p_{out} = 60\ bar$).

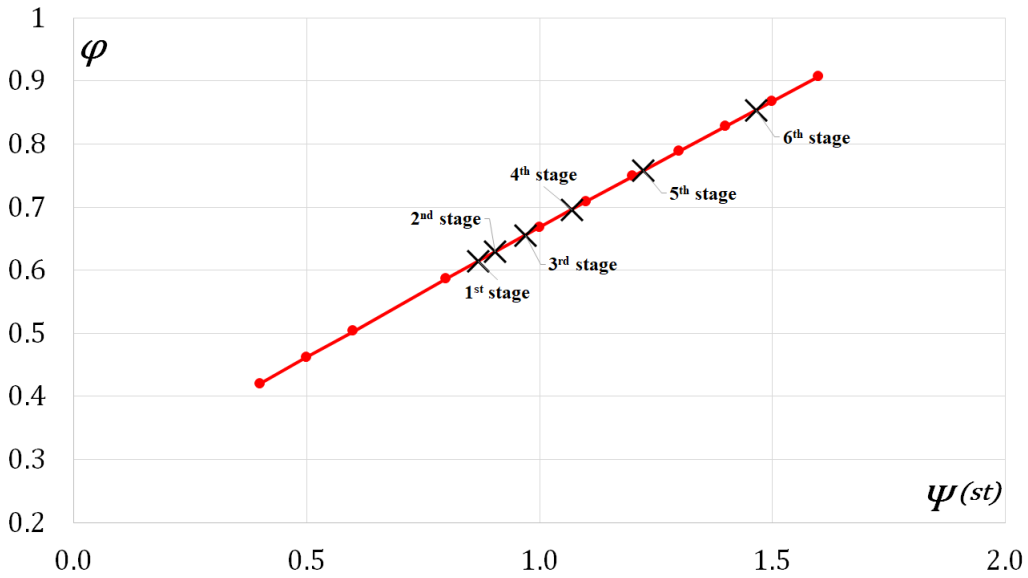

FIGURE 7.11: Change of operating points stage by stage (p_{in} = 150 *bar* and p_{out} = 50 *bar*).

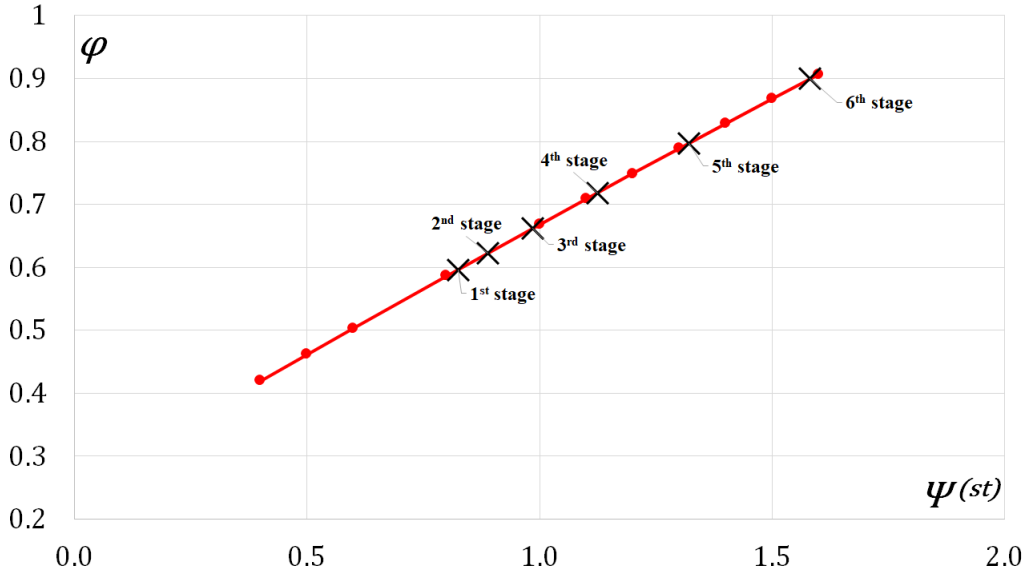

FIGURE 7.12: Change of operating points stage by stage (p_{in} = 130 *bar* and p_{out} = 30 *bar*).

Chapter 8

Conclusions and Future Developments

8.1 Conclusions

The results of this thesis have been reached thanks to a partnership, which has allowed to merge both the academic and the industrial know-hows.

The technical literature survey of Chapter 2 has highlighted how PaTs represent a common issue between many scientific fields, which are focusing on PAT as an efficient way of generating energy from sources that would be wasted through a theoretical and experimental studies.

A consistent effort has been made by the scientific community with the aim to predict the pump performance in reverse mode. This thesis has mainly focused on this issue by improving a manufacturer pre-existent prediction model though experimental and theoretical investigations. As illustrated in Chapter 3, a closed-loop test rig for experimental studies on hydraulic pumps and turbines has been set up at the Department of Mechanics, Mathematics and Management (DMMM) of the Polytechnic University of Bari, in order to experimentally support the theoretical studies on PaTs. At the same time, this test rig could be an important facility for those pump manufacturers that would like to investigate more deeply their machine operations. A hardware and software architecture have been developed to remotely control the test rig and perform experimental tests. A KSB single-stage centrifugal pump has been tested in both direct and reverse modes.

All the test rig results have been shown in Chapter 4, where experimental characteristic curves have been exploited to develop the experimental model for turbine BEP prediction, and to carry out a preliminary assessment of the installation of the same PaT in a real water distribution network. In Chapter 5 two new different prediction models have been proposed: (i) an experimental model for the prediction of the BEP of PaTs, as a selection tool for users; (ii) and another 1-D model for the prediction of the entire characteristic, as a design tool for manufactures.

The first model has been proposed for users who would select the best PaT for a specific application. The model has been based on a greater number of samples constituted by gathering all the PaTs found in the literature, in order to have a better accuracy and a more general applicability in the prediction of PaT's BEP. It was preferred to base the model on the specific speed number rather than on the efficiency at BEP under pump operating mode, because representing families of different pumps that could work in similar operating conditions. The proposed model has been compared with other models in terms of head and discharge prediction errors by using a new set of pumps. Although data showed a significant dispersion and the sample is not yet big enough, it has presented a greater number of pumps with head and discharge BEP in turbine operation prediction errors within ± 10 %.

Obviously, the results given by models in this field depend both on the proposed method and on the set of machines used for calibration. As the calibration set gets richer, the model can gain in generality but may lose accuracy. Indeed, the new 11 pumps, used to validate the model, have been added to the starting data set. As result, the new interpolating curves have showed R squared value lower than the previous ones. At this point, the machine data set has been divided in three groups by a specific property (in our case by the pump specific speed), in order to obtain "specialized" models to be applied only to the pumps with that property. It has been possible to divide the data set in radial-vane types, Francis-vane types and mixed-flow types. As result, only the radial type has showed an improvement with respect to the proposed model in terms of R squared values of the experimental correlations, whereas there is a significant decrease for Francis-vane and Mixed-flow types. This could depend on the significant data dispersion. Actually, further experiments are thus required in order to add a bigger number of pumps for each specific sample.

The second model is a new 1-D prediction model, which has been developed in partnership with Nuovo Pignone, in order to predict the entire characteristic of a PaT, by taking into account detailed geometrical information of the machine, hydraulic losses, and the influence of the slip phenomenon at the outlet section of the runner during turbine operation. This last aspect has been often neglected in PaTs. Three machines by Nuovo Pignone have been used as case studies (i.e., two single-stage centrifugal pumps, and a two-stages centrifugal pump). As a result, the use of detailed geometrical information, the introduction of the slip factor, and a new modeling of hydraulic losses have implied a more accurate prediction of the off-design operating points with prediction errors within ± 4 % .

Furthermore, a preliminary assessment about the installation of a PaT in a real water distribution network has been conducted in Chapter 6. The case study analyzed in this work is Casamassima (BA), located in Puglia (Southern Italy). The experimental characteristic curves of the KSB PaT (showed in in Chapter 4) have been used for this work. Then, starting from the analysis of the pressure and flow rate patterns during the day and the night, three installation cases have been evaluated and compared in terms of hydraulic energy harvesting and power output useful to supply an electrical charging station: Case # 1) the installation of two different PaTs, each of them works alone during the day and the night; Case # 2) the installation of two identical PaTs: the first works alone during the night and the second works in parallel to the first during the day; Case # 3) the installation of only one PaT, which works during the day and the night. Although Case # 1 and Case # 2 are better than Case # 3 in terms of hydraulic energy harvesting, Case # 3 can be considered a practical solution to be implemented because it shows the simplest layout with one PaT, one PRV and the by-pass line. Moreover, Case # 3 represents a good compromise in terms of power generation and cost installation. Obviously, further economic analysis has to be performed in order to have a more detailed assessment of the installation of a PaT in the real water distribution network of Casamassima.

This thesis aims at studying PaTs not only in hydraulic power generation but also in processes engineering, where fluids containing dissolved or undissolved gases or volatiles can be expanded from a higher to a lower pressure level for energy recovery. A literature survey has been conducted in order to investigate the behavior of centrifugal pumps operating in reverse mode with two-phase flows. The first technical reports in the literature can be dated back to the early '80. These models are essentially based on the assumption of a homogeneous flow, which is in two-phase condition from the inlet to outlet section of the machine. In this work a fluid with the vapour phase, which is not present at the inlet section of the machine and increases

during the expansion is considered.

In Chapter 7, a 6-stages centrifugal pump operating as turbine has been used as a case study in order to develop a theoretical model, which predicts the performance operating with two-phase flow. Companies usually test their machines in single phase (generally water). By starting from the characteristic curves provided by the company, non-dimensional curves have been obtained $\psi = f(\varphi)$ and $\eta_y = f(\varphi)$. Thanks to these curves, is possible to model the behavior of the same machine operating with a two-phase mixture, whose properties are known. The advantage of the proposed model is that it does not rely on experimental correlations based on a limited number of samples, which could limit its range of applicability. Although experimental data are not available yet, the model has been proposed as an engineering tool which can help in the initial prediction of the performance of a PaT operating with a two-phase flow.

8.2 Future Developments

At the end of these investigations, some research lines have been identified as future developments:

- Initially, an upgrade of the test rig could support CFD investigations about cavitation and multi-phase flow in PaTs;
- The theoretical proposed model could be improved for multistage PaTs with a greater number of stages than two. Moreover, further CFD investigations should be carried out on different PaT impellers in order to study more deeply the effect of the slip phenomenon;
- By a practical point of view, the preliminary assessment on the real case study investigated needs of a next step, where the 1-D theoretical model could be applied to other pumps in order to estimate off-design operating condition and finally choose the best machine for the site;
- Experimental activities on PaTs operating with two-phase flows should be carried out in order to improve the prediction model for PaT in processing engineering.

Bibliography

[1] *Pumps as turbines in the water industry*. URL: http://www.worldpumps.com.

[2] United Nations Industrial Development Organization and International Center on Small Hydro Power. *World Small Hydropower Development Report 2016*. 2016.

[3] C. Alatorre-Frenk. "Cost minimisation in micro-hydro systems using pumps-as-turbines". PhD thesis. University of Warwick, 1994.

[4] D. Thoma and C.P. Kittredge. "Centrifugal pumps operated under abnormal conditions". In: *Journal of Power Sources* 73.1 (1931), pp. 881–884.

[5] S.V. Jain and R.N. Patel. "Investigations on pump running in turbine mode: A review of the state-of-the-art". In: *Renewable and Sustainable Energy Reviews* 30 (2014), pp. 841–868.

[6] R.T. Knapp. "Centrifugal-Pump Performance as Affected by Design Features". In: *Transactions of the ASME* (1941), pp. 251–260.

[7] A.J. Stepanoff. *Centrifugal and axial flow pumps: theory, design, and application*. Wiley New York, 1957.

[8] U. Ruggiero. "Studio teorico delle pompe-turbine assiali a funzionamento reversibile". In: *Annuali della Facoltà di Ingegneria di Bari* 7 (1967).

[9] C.H. Laux. "Rückwärtslaufende mehrstufige Pumpen als Energierückgewinnungs-Turbinens in Ölversorgunssystemen". In: *Technische rundschau Sulzer* 2 (1980), pp. 61–80.

[10] C.H. Laux. "Rückwärtslaufende Standardpumpen als Rekuperationsturbinen". In: *Technische rundschau Sulzer* 2 (1982), pp. 23–27.

[11] R. Apfelbacher and F. Etzold. "Energy-Saving, Shock-Free Throttling with the Aid of a Reverse Running Centrifugal Pump". In: *KSB Technische Berichte* 24e (1988), pp. 33–41.

[12] S.S. Yang, S. Derakhshan, and F.Y. Kong. "Theoretical, numerical and experimental prediction of pump as turbine performance". In: *Renewable Energy* 48 (2012), pp. 507 –513.

[13] O. Fecarotta, H.M. Ramos, S. Derakhshan, G. Del Giudice, and A. Carravetta. "Fine Tuning a PAT Hydropower Plant in a Water Supply Network to Improve System Effectiveness". In: *Journal of Water Resources Planning and Management* 144.8 (2018).

[14] S. Barbarelli, M. Amelio, and G. Florio. "Experimental activity at test rig validating correlations to select pumps running as turbines in microhydro plants". In: *Energy conversion and Management* 149 (2017), pp. 781 –797.

[15] F. Pugliese, F. De Paola, N. Fontana, G. Marini, and M. Giugni. "Optimal Selection of Pumps As Turbines in Water Distribution Networks". In: *Multidisciplinary Digital Publishing Institute Proceedings*. Vol. 2. 11. 2018, p. 685.

[16] G. Balacco, A. Carbonara, A. Gioia, V. Iacobellis, and A.F. Piccinni. "Evaluation of peak water demand factors in Puglia (Southern Italy)". In: *Water* 9.2 (2017), p. 96.

[17] A. Carravetta, O. Fecarotta, R. Martino, and L. Antipodi. "PAT efficiency variation with design parameters". In: *Procedia Engineering* 70 (2014), pp. 285–291.

[18] *Creating a Smart Water Grid*. URL: `http://www.rentricity.com`.

[19] A. Muhammetoglu, E. Karadirek, O. Ozen, and H. Muhammetoglu. "Full-scale PAT application for energy production and pressure reduction in a water distribution network". In: *Journal of Water Resources Planning and Management* 143.8 (2017).

[20] M. Rossi, M. Righetti, and M. Renzi. "Pump-as-turbine for energy recovery applications: the case study of an aqueduct". In: *Energy Procedia* (2016), pp. 1207–1214.

[21] G. Balacco, M. Binetti, V. Caporaletti, A. Gioia, L. Leandro, V. Iacobellis, C. Sanvito, and A.F. Piccinni. "Innovative mini-hydro device for the recharge of electric vehicles in urban areas". In: *International Journal of Energy and Environmental Engineering* (2018).

[22] J. Alberizzi, M. Renzi, A. Nigro, and M. Rossi. "Study of a Pump-as-Turbine (PaT) speed control for a Water Distribution Network (WDN) in South-Tyrol subjected to high variable water flow rates". In: *Proceedings of the 73rd Conference of the Italian Thermal Machines Engineering Association, ATI2018, 12-14 September 2018, Pisa, Italy* (2018).

[23] J. Du, H. Yang, Z. Shen, and J. Chen. "Micro hydro power generation from water supply system in high rise buildings using pump as turbines". In: *Energy* 137 (2017), pp. 431–440.

[24] G.D. Ciocan, O. Teller, and F. Czerwinski. "Variable speed pump-turbines technology". In: *University" Politehnica" of Bucharest Scientific Bulletin, Series D: Mechanical Engineering* 74.1 (2012), pp. 33–42.

[25] *Pumped hydroelectric Storage*. URL: `http://www.ourworldofenergy.com`.

[26] M. Arriaga. "Pump as turbine–a pico-hydro alternative in Lao People's Democratic Republic". In: *Renewable Energy* 35.5 (2010), pp. 1109–1115.

[27] A. Carravetta, S. Derakhshan, and H.M. Ramos. *Pumps as turbines: Fundamentals and applications*. Springer, 2017.

[28] A.J. Semple and W. Wong. "The application of hydraulic power recovery turbines in process plant". In: *I.Mech.E.* C35/84 (1984), pp. 227–234.

[29] S. Gopalakrishnan. "Power recovery turbines for the process industry". In: *Proceedings of the 3rd International Pump Symposium*. Turbomachinery Laboratories, Department of Mechanical Engineering, Texas A&M University. 1986.

[30] W. Raja and R. Piazza. "Reverse running centrifugal pumps as hydraulic power recevery turbines for seawater reverse osmosis systems". In: *Desalination* 38 (1981), pp. 123–134.

[31] W. Bolliger. "Pumpen und Turbinen in Anlagen für umgekehrte Osmose". In: *Technische rundschau Sulzer* 3 (1984), pp. 29–32.

[32] W. Bolliger. "Pumpen als Turbinen erfolgreich". In: *Technische rundschau Sulzer* 2 (1997), pp. 27–29.

[33] H.J. Van Antwerpen and G.P. Greyvenstein. "Use of turbines for simultaneous pressure regulation and recovery in secondary cooling water systems in deep mines". In: *Energy Conversion and Management* 46.4 (2005), pp. 563–575.

[34] M. Amelio, S. Bova, G. Florio, and N.M. Scornaienchi. "Primi risultati del Banco per la Prova di Pompe-Turbine dell' Università della Calabria". In: *Proceedings of the 52nd Conference of the Italian Thermal Machines Engineering Association, ATI1997, Como, Italy* 2 (1997), pp. 879–889.

[35] S. Derakhshan and A. Nourbakhsh. "Experimental study of characteristic curves of centrifugal pumps working as turbines in different specific speeds". In: *Experimental Thermal and Fluid Science* 32.3 (2008), pp. 800 –807.

[36] H. Nautiyal, V. Varun, Varun, A. Kumar, and S. Yadav. "Experimental investigation of centrifugal pump working as turbine for small hydropower systems". In: *Energy Science and technology* 1.1 (2011), pp. 79–86.

[37] F. Pugliese, F. De Paola, N. Fontana, M. Giugni, and G. Marini. "Experimental characterization of two pumps as turbines for hydropower generation". In: *Renewable energy* 99 (2016), pp. 180–187.

[38] P. Singh and F. Nestmann. "An optimization routine on a prediction and selection model for the turbine operation of centrifugal pumps". In: *Experimental Thermal and Fluid Science* 34.2 (2010), pp. 152–164.

[39] G. Shi, X. Liu, Z. Wang, and Y. Liu. "Conversion relation of centrifugal pumps as hydraulic turbines based on the amplification coefficient". In: *Advances in Mechanical Engineering* 9.3 (2017).

[40] X. Tan and A. Engeda. "Performance of centrifugal pumps running in reverse as turbine: Part II - systematic specific speed and specific diameter based performance prediction". In: *Renewable energy* 99 (2016), pp. 188 –197.

[41] A. Carravetta, O. Fecarotta, and H.M. Ramos. "A new low-cost installation scheme of PATs for pico-hydropower to recover energy in residential areas". In: *Renewable Energy* 125 (2018), pp. 1003–1014.

[42] A.A. Williams. "The turbine performance of centrifugal pumps: a comparison of prediction methods". In: *Proceedings of the Institution of Mechanical Engineers, Part A: Journal of Power and Energy* 208.1 (1994), pp. 59–66.

[43] K. Sharma. "Small hydroelectric project-use of centrifugal pumps as turbines". In: *Kirloskan Electric Co., Bangalore* (1985).

[44] J.F. Gülich. *Centrifugal pumps*. Vol. 2. Springer, 2008.

[45] S. Barbarelli, M. Amelio, and G. Florio. "Predictive model estimating the performances of centrifugal pumps used as turbines". In: *Energy* 107 (2016), pp. 103–121.

[46] G. Ventrone. "Deviazione Della Corrente Relativa Nelle Giranti Delle Turbine Francis". In: *L'energia elettrica* 9 (1972), pp. 569 –574.

[47] G. Shi, X. Liu, J. Yang, S. Miao, and J. Li. "Theoretical research of hydraulic turbine performance based on slip factor within centripetal impeller". In: *Advances in Mechanical Engineering* 7 (2015).

[48] M. Binama, W.T. Su, X.B. Li, F.C. Li, X.Z. Wei, and S. An. "Investigation on pump as turbine (PAT) technical aspects for micro hydropower schemes: A state-of-the-art review". In: *Renewable and Sustainable Energy Reviews* 79 (2017), pp. 148–179.

[49] T. Capurso, M. Stefanizzi, M. Torresi, G. Pascazio, G. Caramia, S.M. Camporeale, B. Fortunato, and L. Bergamini. "How to Improve the Performance Prediction of a Pump as Turbine by Considering the Slip Phenomenon". In: *Multidisciplinary Digital Publishing Institute Proceedings*. Vol. 2. 11. 2018, p. 683.

[50] P. Singh. "Optimization of internal hydraulics and of system design for pumps as turbines with field implementation". PhD thesis. Institut für Wasserwirtschaft und Kulturtechnik, Universität Karlsruhe (TH), 2005.

[51] P. Singh and F. Nestmann. "Internal hydraulic analysis of impeller rounding in centrifugal pumps as turbines". In: *Experimental Thermal and Fluid Science* 35.1 (2011), pp. 121–134.

[52] T. Wang, C. Wang, F. Kong, Q. Gou, and S. Yang. "Theoretical, experimental, and numerical study of special impeller used in turbine mode of centrifugal pump as turbine". In: *Energy* 130 (2017), pp. 473–485.

[53] X. Su, S. Huang, Y. Li, Z. Zhu, and Z. Li. "Numerical and experimental research on multi-stage pump as turbine system". In: *International Journal of Green Energy* 14.12 (2017), pp. 996–1004.

[54] W.G. Li. "Optimising prediction model of centrifugal pump as turbine with viscosity effects". In: *Applied Mathematical Modelling* 41 (2017), pp. 375–398.

[55] M. Rossi, G. Comodi, N. Piacente, and M. Renzi. "Effects of viscosity on the performance of Hydraulic Power Recovery Turbines (HPRTs) by the means of Computational Fluid Dynamics (CFD) simulations". In: *Proceedings of the 73rd Conference of the Italian Thermal Machines Engineering Association, ATI2018, 12-14 September 2018, Pisa, Italy* (2018).

[56] G. Olimstad, T. Nielsen, and B. Børresen. "Dependency on runner geometry for reversible-pump turbine characteristics in turbine mode of operation". In: *Journal of Fluids Engineering* 134.12 (2012).

[57] G. Olimstad, T. Nielsen, and B. Børresen. "Stability limits of reversible-pump turbines in turbine mode of operation and measurements of unstable characteristics". In: *Journal of fluids engineering* 134.11 (2012).

[58] T.K. Nielsen and G. Olimstad. "Dynamic Behaviour of Reversible Pump-Turbines in Turbine Mode of Operation". In: *13th International Symposium on Transport Phenomena and Dynamics of Rotating Machine* (2010).

[59] C. Hamkins, H.O. Jeske, R. Apfelbacher, and O. Schuster. "Pumps as energy recovery turbines with two phase flow". In: *ASME Pumping Machinery Symp, San Diego* (1989), pp. 73–81.

[60] F.C. Visser. "Basic Considerations for Evaluating Hydraulic Power Recovery of Fluid Streams Expanding With or Without Gas or Vapor Evolution". In: *ASME 2005 Fluids Engineering Division Summer Meeting*. American Society of Mechanical Engineers. 2005, pp. 1137–1146.

[61] P. Payvar. "Mass transfer-controlled bubble growth during rapid decompression of a liquid". In: *International journal of heat and mass transfer* 30.4 (1987), pp. 699–706.

[62] P. Maher, N.P. Smith, and A.A. Williams. "Assessment of pico hydro as an option for off-grid electrification in Kenya". In: *Renewable Energy* 28.9 (2003), pp. 1357–1369.

[63] K.H. Motwani, S.V. Jain, and R.N. Patel. "Cost analysis of pump as turbine for pico hydropower plants–a case study". In: *Procedia Engineering* 51 (2013), pp. 721–726.

[64] M. Kramer, K. Terheiden, and S. Wieprecht. "Pumps as turbines for efficient energy recovery in water supply networks". In: *Renewable Energy* 122 (2018), pp. 17–25.

[65] *Application-oriented Planning Documents for Pumps as Turbines*. URL: http://www.ksb.com.

[66] *ANDRITZ centrifugal pump as turbine*. URL: http://www.andritz.com.

[67] *Pump Hydro Turbine*. URL: http://www.ge.com.

[68] *Awa Prozone*. URL: http://www.thermocold.it.

[69] *Lika SMRI5*. URL: http://www.lika.it.

[70] *T40B Universal Digital Torque Transducer*. URL: http://www.hbm.com.

[71] *PCB 113B21*. URL: http://www.pcb.com.

[72] *NI PXIe-8135*. URL: http://www.ni.com/pdf/manuals/373716b.pdf.

[73] *NI PXIe-4499*. URL: http://www.ni.com/pdf/manuals/372125f.pdf.

[74] *NI PXIe-8431/8*. URL: http://www.ni.com/pdf/manuals/373170f.pdf.

[75] *Chassis CompactRIO NI 9144*. URL: http://www.ni.com/pdf/manuals/372498a_02.pdf.

[76] *C Series Relay Output Module NI 9481*. URL: http://www.ni.com/pdf/manuals/373507d.pdf.

[77] *C Series Analog Output Module NI 9263*. URL: http://www.ni.com/pdf/manuals/373781b_02.pdf.

[78] *C Series Analog Input Module NI 9201*. URL: http://www.ni.com/pdf/manuals/373783a_02.pdf.

[79] *C Series Analog Input Module NI 9203*. URL: http://www.ni.com/pdf/manuals/374070a_02.pdf.

[80] *C Series RTD Module NI 9217*. URL: http://www.ni.com/pdf/manuals/374187a_02.pdf.

[81] R.L. Mott, F.M. Noor, and A.A. Aziz. "Applied fluid mechanics". In: (2006).

[82] *Rotodynamic pumps – Hydraulic performance acceptance tests – Grades 1, 2 and 3*. URL: https://www.iso.org/standard/41202.html.

[83] M. Stefanizzi, M. Torresi, B. Fortunato, and S.M. Camporeale. "Experimental investigation and performance prediction modeling of a single stage centrifugal pump operating as turbine". In: *Energy Procedia* 126 (2017), pp. 589–596.

[84] M. Stefanizzi, T. Capurso, M. Torresi, G. Pascazio, S. Ranaldo, S.M. Camporeale, B. Fortunato, and R. Monteriso. "Development of a 1-D Performance Prediction Model for Pumps as Turbines". In: *Multidisciplinary Digital Publishing Institute Proceedings*. Vol. 2. 11. 2018, p. 682.

[85] S.S. Yang, F.Y. Kong, W.M. Jiang, and X.Y. Qu. "Effects of impeller trimming influencing pump as turbine". In: *Computers & Fluids* 67 (2012), pp. 72–78.

[86] S. Huang, G. Qiu, X. Su, J. Chen, and W. Zou. "Performance prediction of a centrifugal pump as turbine using rotor-volute matching principle". In: *Renewable Energy* 108 (2017), pp. 64–71.

[87] *Pipeline pump*. URL: http://www.ksb.com.

[88] A. Busemann. "Stability limits of reversible-pump turbines in turbine mode of operation and measurements of unstable characteristics". In: *ZAMM - Journal of Applied Mathematics and Mechanics / Zeitschrift für Angewandte Mathematik und Mechanik* 8.5 (1928), pp. 372–384.

[89] A. Stodola. *Dampf-und Gasturbinen: mit einem Anhang über die Aussichten der Wärmekraftmaschinen; mit einem Nachtrag nebst Entropie-Tafel für hohe Drücke u. B1-T-Tafel zur Ermittlung des Rauminhaltes*. Springer, 1924.

[90] *Worthington*. URL: http://www.abset.com.

[91] M. Stefanizzi, T. Capurso, G. Balacco, M. Binetti, A.F. Piccinni, B. Fortunato, S.M. Camporeale, and M. Torresi. "Preliminary assessment of the installation of a Pump as Turbine in a Real Water Distribution Network". In: *under review for the12th European Conference on Turbomachinery Fluid dynamics and Thermodynamics, ETC13, April 8-12, 2018, Lausanne, Switzerland* (2018).

[92] *How to Select Turbomachinery For Your Application*. URL: https://www.barber-nichols.com/sites/default/files/wysiwyg/images/how_to_select_turbomachinery_for_your_application.pdf.

[93] M. Stefanizzi, M. Torresi, F. Fornarelli, B. Fortunato, and S.M. Camporeale. "Performance prediction model of multistage centrifugal Pumps used as Turbines with Two-Phase Flow". In: *Proceedings of the 73rd Conference of the Italian Thermal Machines Engineering Association, ATI2018, 12-14 September 2018, Pisa, Italy* (2018).

[94] *Multistages Pumps*. URL: http://www.flexachem.com.

[95] C.E. Brennen. *Fundamentals of multiphase flow*. Cambridge university press, 2005.

[96] W.M. Verde, J.L. Biazussi, N. A. Sassim, and A.C. Bannwart. "Experimental study of gas-liquid two-phase flow patterns within centrifugal pumps impellers". In: *Experimental Thermal and Fluid Science* 85 (2017), pp. 37–51.